TÉCNICO LISBOA

Frequency domain response of a propfan using finite element method and experimental study on a rotor

Luís Guilherme Figueira Franco

Thesis to obtain the Master of Science Degree in

Aerospace Engineering

Supervisor: Prof. Miguel António Lopes de Matos Neves

Examination Committee

Chairperson: Prof. Fernando José Parracho Lau
Supervisor: Prof. Miguel António Lopes de Matos Neves
Member of the Committee: Prof. Tiago Alexandre Narciso da Silva

November 2017

Acknowledgments

I would like to express my sincere gratitude to Professor Miguel Matos Neves from DEM, IST, for the opportunity of working with him and for the patience, support and guidance throughout the development of this work.

I must also leave a word of gratitude to Professor Hugo Policarpo for his constant availability and suggestions concerning the experimental tests performed in the laboratory.

I must thank my colleagues and friends, whose friendship I treasure.

Finally, I would like to thank my family for their support throughout my studies and throughout my whole life.

Resumo

Actualmente, o estudo da Dinâmica de Rotores é fundamental para compreender o comportamento de grande parte das máquinas rotativas, tais como: turbinas, compressores, bombas e geradores. Na indústria aeronáutica, a Dinâmica de Rotores é bastante importante e, maioritariamente, usado no contexto dos motores das aeronaves. Uma vez que é inevitável evitar falhas em estruturas reais, devido ao fabrico imperfeito ou a acidentes operacionais, é essencial prevenir e corrigir o comportamento indesejado de máquinas rotativas.

Por conseguinte, esta tese é focada na validação de um método numérico (Método de Elementos Finitos) usado para simular a resposta dinâmica de máquinas rotativas. O processo de validação é realizado através de uma comparação directa dos resultados obtidos pelo método dos elementos finitos, com valores experimentais.

O teste experimental foi dirigido para o estudo da resposta em frequência de um sistema de rotores, o "SpectraQuest's Machinery Fault Simulator" (MFS). A metodologia experimental é, completamente, descrita e as Funções de Resposta em Frequência (FRFs) usadas para prever condições de ressonância, são cuidadosamente interpretadas. Os testes são divididos em duas etapas: na primeira etapa, obtém-se as FRFs do rotor em repouso (usando o teste do martelo de impacto); na segunda etapa, adquire-se a resposta do sistema em operação para diferentes velocidades de rotação (usando a função "autospectrum").

Após a conclusão do processo de validação, o método numérico desenvolvido é aplicado a um caso de estudo da aeronáutica, o motor Propfan criado no âmbito do projecto Europeu DUPRIN (DUcted PRopfan INvestigation).

Palavras-chave: Dinâmica de Rotores, Domínio em Frequência, Método de Elementos Finitos, Análise Modal Experimental, MFS, Propfan

Abstract

Nowadays, the study of Rotordynamics is fundamental to comprehend the behaviour of most rotating machinery, such as turbines, compressors, pumps and generators. In the aeronautical industry, the Rotordynamics field is very important and mostly used in the subject of aircraft engines. Since it is inevitable to avoid faults in real structures, due to imperfect manufacturing or unwanted operation accidents, it is essential to design, predict and correct the unwanted behaviour of rotating machinery.

As such, this thesis is focused on the validation of a numerical method (Finite Element Method) used to measure the dynamic response of rotor machinery. The validation process is performed by a direct comparison of the results obtained, resorting to the finite element model, with experimental values.

The experimental test is focused on the frequency response study of a rotor system, the Spectra Quest's Machinery Fault Simulator (MFS). The experimental methodology is thoroughly described and the Frequency Response Functions (FRFs), used to predict resonance conditions, are carefully interpreted. The tests are divided into two stages: in the first stage, one obtains the rotor's FRF while at rest (using the impact hammer test); in the second stage, one acquires the system's response while operating at different spin speeds (using the autospectrum function).

After concluding the validation process, the developed numerical method is applied to a case-study of aeronautics, the Propfan engine created under the European project DUPRIN (DUcted PRopfan INvestigation).

Keywords: Rotordynamics, Frequency Domain, Finite Element Method, Experimental Modal Analysis, MFS, Propfan

Contents

List of Tables

List of Figures

Nomenclature

Greek symbols

α	Modal damping
β	Force phase angle
δ	Nodal displacement vector; virtual displacement
Γ	Boundary
γ	Coherence function
λ, μ	Lamé constants
ν	Poisson's coefficient
Ω	Domain; Rotating speed
ω	Angular frequency
ω_{ap}	Applied excitation frequency
ω_N	Natural frequency
Ψ_r	Eigenvectors; Vibration modes
ρ	Density
σ	Stress; decay factor
θ, ψ, ϕ	Euler angles
ε	Strain

Roman symbols

$\bar{X}$	Displacement amplitude
$\hat{Q}$	Load amplitude vector
A	Area; Accelerance matrix
a	Gyroscopic effect

C, c	Damping matrix; Damping coefficient
E	Longitudinal modulus of elasticity or Young's modulus
F	Force
F_0	Force Amplitude
F_t	Exciting Force
G	Shear modulus or modulus of rigidity
H	Receptance matrix
h	Thickness
I	Shaft second moment of area; Identity matrix
I_{Dx}, I_{Dy}, I_{Dz}	Disk inertia moments about its principal axis xyz
j	Imaginary unit
K, k	Stiffness matrix; stiffness coefficient
L, l	Length
M, m	Mass matrix; Mobility matrix; Mass
n	Normal unit vector; number of degrees of freedom
N_α	Shape function
q_i	Generalized coordinate
R	Outer radius
r	Inner radius
$R_0(X, Y, Z)$	Inertial reference frame
$R_i(x, y, z)$	Non-inertial reference frame
S	Surface; Cross-section area of the shaft
s	Eigenvalue of the modal analysis
T	Surface Forces; Kinetic energy
t	Traction vector; Time
U	Strain energy
u, v, w	Displacements along the x, y, and z directions
V	Volume

W Virtual work

X, Y, Z Inertial reference frame coordinates

x, y, z Cartesian Coordinates; Displacement; Non-inertial reference frame coordinates

Acronyms

BW Backward whirl

DOF Degree of Freedom

DUPRIN Ducted Propfan Investigation

FEM Finite Element Method

FFT Fast Fourier Transform

FRF Frequency Response Function

FW Forward whirl

MDOF Multiple Degrees of Freedom

MFS Machinery Fault Simulator

SDOF Single Degree of Freedom

SISO Single Input - Single Output

Chapter 1

Introduction

1.1 Background

Nowadays a considerable number of machinery is used for applications where rotors and bearings are of critical importance. These parts play a significant role in many components such as compressors, turbines, pumps, aircraft engines, ship engines, electrical generators, among others. Aeronautical and aerospace industries often require increase power output using more-flexible, lighter and faster rotors, influencing the need, from the design phase to field-diagnostics, for an understanding of the interaction between the resulting static and dynamic forces acting on the rotating elements and stationary equipment such as the bearings, seals, machinery casing, etc.

As stated in Genta [1], ”a rotor is a body suspended through a set of cylindrical hinges or bearings that allows it to rotate freely about an axis fixed in space ” and it may be characterized in two groups, fixed rotors and free rotors. Fixed rotors are equipped with material bearing used to constrain their spin axis in a fixed position in space in a more or less rigid way, while free rotors are not constrained in any direction by their bearings. The field of engineering that studies the transverse and torsional vibrations of rotating shafts is called rotordynamics. One of its objectives is the prediction of excessive vibrations applied on the rotor ensuring the safe and reliable operation of rotating structures. Some aspects like gyroscopic moments, cross-coupled forces, critical speeds and whirling effects are investigated in rotordynamics and are not studied in structural vibration analysis.

The establishment of more comprehensive standards combined with the demands for improved performance and high power/weight output has accentuated the value of the designer’s prediction of lateral critical speeds along with associated amplification factors and system stability parameters. Also, the further use of rotordynamics modelling techniques along with the practical knowledge of rotating machinery is being accepted as an extremely valuable and powerful field-diagnostic approach.

1.2 Motivation and Objectives

The large increase in rotational speed of many machinery components made it critical to include rotation into the analysis of their dynamic behaviour. Most of rotor dynamics studies were motivated by turbomachines being incapable of producing their estimated performance or even functioning at all, due to the lack of some rotordynamics requirements. Thus, it is mandatory to understand the principals of this field to develop and design rotor-bearing systems for various applications. As stated by Vance et al. [2], a fundamental approach to a rotordynamic analysis generally involves the following process:

1. Predict critical speeds;
2. Determine design modifications to change critical speeds;
3. Predict natural frequencies of torsional vibration;
4. Calculate balance correction masses and locations from measured vibration data;
5. Predict amplitudes of synchronous vibration caused by rotor unbalance;
6. Predict threshold speeds and vibration frequencies for dynamic instability;
7. Determine design modifications to avoid dynamic instabilities.

During the development of this thesis, these guide lines are carefully examined aside from the third topic, since torsional vibration is considered from the beginning as out of scope of this work.

Before analysing the previous topics, a proper revision on the theory and fundamentals of rotordynamics is presented. Understanding of basic rotordynamics phenomena and the various types of problems is absolutely mandatory when designing and developing rotor-bearing systems for various applications. To accomplish this objective an application of a mathematical model created by Lalanne and Ferraris [3] is used to describe the rotor behaviour, which derives from the energy and work expressions of the rotor components in order to acquire the system's lateral dynamic equations of motion.

It is important to emphasize that all methods and analysis established in this work are developed on the frequency domain, allowing the use of techniques to determine the stability of the system and also give more insight to the steady state response of the rotor's behaviour under different working conditions. Consequently, it is possible to elaborate studies on new rotor configurations to enhance its design and create a sturdier system.

In order to prevent rotor critcal operational conditions, this work focused on the validation of a finite element method (FEM) following the numerical developments made by Rafael Carvalho [4] and Miguel Matos [5] to study the vibrational response of a rotor system, based on the Campbell diagram. Testing the FEM with other numerical, analytical and experimental studies enables the verification and validation of this process to determine its efficiency and computational cost. Then, the proposed numerical methodology is applied on the investigation of the frequency domain response of a Propfan engine.

The contribution of this discussion is expected to allow fundamental statements on vibrational behaviour of machines and their elements, discovering excitations, their causes and defining critical or dangerous rotational speeds creating the required precautions to avoid possible risks.

1.3 Brief Literature Review

According to Nelson in [6], a German civil engineer called August Föppl proposed (in 1895) what is considered the first successful rotor model designed to analyse the dynamic behaviour and vibration of rotational structures. The model was composed by a single disk centrally located on a circular elastic shaft with undamped rigid bearings placed at each end of the shaft. The author used this model to demonstrate that supercritical operation was still possible, i.e. Föppl showed that rotor activity was still viable even if the shaft's rotational speed surpassed the established critical speed.

Using a similar model to August Föppl, but this time with damping, Henry Jeffcott [7] confirmed Föppl prediction that a stable supercritical solution existed. Since Jeffcott's publication was the first most recognized work on this subject, a rotor model with viscous damping supports at each shaft end, consisting of one disk on a constant circular cross-section shaft, is called a Jeffcott rotor. Although, his model is still a simplification of a real-world rotor, thus it is mostly used to acquire basic knowledge on realistic rotor system behaviour.

A tool known as the Campbell diagram was created by Wilfred Campbell [8] in 1924, where the system natural frequencies are plotted as a function of the shaft spin speed. Considering the evolution of new and more complex rotor systems, new solving methods were developed and applied to this subject, such as the FEM. The first rotordynamics finite element model was introduced by Ruhl and Booker [9], which included elastic bending energy and translational kinetic energy. Subsequently, Nelson and McVaugh [10] developed a finite element model for both stationary and rotating reference, which included the gyroscopic moment and axial loading. Later, Nelson [11] and Genta [12] applied the Timoshenko beam theory to rotor systems.

Since the rotor dynamics subject can be rather confusing for new learners, an excellent and easy understanding of the physical concepts related to this theme was first available by Nelson [6], where the author focuses more on the physics of the problem than the math of it. This publication includes the description of whirl frequencies and modes, critical speeds, instability, the equation of motion and other phenomena related to rotordynamics. Nelson's article is a great introduction to clarify various complex concepts on this subjects, but in order to have a more consistent model, numerical method are used.

Essential numerical methods for rotordynamics are presented by Lalanne and Ferraris [3] in their book "Rotordynamics Prediction in Engineering". Their work includes the description of the basic rotor components, the derivation of the basic equations of motion and the application of the FEM to some industrial results, such as the Propfan engine. Genta [1] and Rao [13] also introduce an accurate explanation on rotordynamics field, including nonlinear and nonstationary phenomena, asymmetric rotor geometries, various fault models (misalignment, unbalanced, bent shafts) and 3D modelling.

The recent MSc thesis of Rafael Carvalho [4] and Miguel Matos [5], who in their respective works created models for a finite element analysis in order to study the lateral dynamic behaviour of rotors and used forced identifications methods applied to rotordynamics, should also be mentioned since one of this project's main objective is the complementation of their initial work.

Relatively to experimental modal analysis, one may highlight the work developed by Silva [14], which

refers to the concentrated mass method used to analyse continuous structures characterized into spacial mass elements, stiffness and damping. This method is part of the base development of the experimental modal analysis, which allows to determine the dynamic properties of a structure through its frequency response functions (FRFs). In [15] Maia and Silva also present an extensive work in this subject, based on the modal and response model. The document presented by Schwarz and Richardson [16] also contains some concepts related to experimental modal analysis, mainly focused on the verification and validation of models. Most of the modal identification methods are already implemented in almost all commercial programms of modal analysis, such as the Pulse of Brüel & Kjaer (see tutorial in [17]).

1.4 Thesis Outline

This Thesis is divided in 5 chapters. Chapter one presents the framework of this thesis, its importance and the respective motivation. Also, it includes the main objective established for this work as well as some revision of the literature regarding elastodynamics, the FEM, the rotor system, modal testing and finally the Propfan case-study.

Chapter two introduces some theoretical and experimental fundamentals used in this work. It starts with the elastic characterization of a solid body followed by an introduction of the FEM. Then, the fundamentals and theory of rotordynamics are presented, including a mathematical model used to represent the rotor system elements based on their energy equations and the deduction of the rotor's equation of motion. Also, the Rayleigh-Ritz analytical method is presented in this chapter. Lastly, one introduces the principles related to experimental modal analysis.

Chapter three describes the different numerical and experimental methodologies adopted and developed in this work. It starts with a detailed description of two numerical models (steel beam and a mono-rotor) created in a commercial finite element ($ANSYS$) environment. Then, in the experimental methodology, one indicates the different aspects related to the experiment, which include the setup used, the experimental models and the procedure applied to each test.

The fourth chapter is dedicated to the presentation and discussion of the results obtained. Thus, it starts with a convergence study with a mention to the FEM computational effort in rotordynamic analysis. After the convergence study, one performs a direct comparison between the FEM and the Rayleigh-Ritz solutions through an assessment on rotordynamics dynamic behaviour. Then, a comparison between numerical and experimental data is presented, which include the analyses of the first natural frequencies and critical speeds of the mono-rotor model used in the laboratory. In the last section of this chapter, results from a numerical modelling of the Propfan engine are presented and discussed.

The fifth and final chapter contains a general discussion of the obtained results and some conclusions about the achievement of the objectives that were established in the beginning of this work.

Chapter 2

Fundamentals

2.1 The Elastodynamic Problem

Through experience, it has come to ones knowledge that every material possesses a specific degree of elasticity, i.e., the external forces applied to a structure may deform it to a certain extent, but it will retrieve its original form completely with the removal of the forces. In this work, the materials will be considered homogeneous and each smallest element possesses the same properties as the original body. It will also be assumed that the materials are isotropic, which means that their elastic properties are equal in all directions. All these hypotheses may diverge from reality, but from experience they have the advantage of simplifying the theoretical model, and therefore, approximating the experimental data to the numerical results [18].

Introducing the small displacement theory, one may assume that the displacements of the material particles are much smaller (infinitesimally smaller) when compared to the body's dimension. This assumption allows to simplify the Green tensor functions of extension-displacement [19], obtaining the following expression in tensional notation (index notation):

$$\varepsilon_{ij} = \frac{1}{2}\left(\frac{\partial u_i}{\partial x_j} + \frac{\partial u_j}{\partial x_i}\right) = \frac{1}{2}(u_{i,j} + u_{j,i}) \tag{2.1}$$

where $\boldsymbol{u}$ represents the displacement vector, $i, j = 1, 2, 3$ are the notation indices corresponding to the directions of the chosen referential and $\boldsymbol{\varepsilon}$ represents the matrix of the infinitesimal strain tensor introduced by Cauchy, which disregards the nonlinear terms of the generalized strain tensor and is given by $\boldsymbol{\varepsilon} = \varepsilon_{ij} e_i e_j$.

In the case considered here, after applying an external force (static or dynamic) to the body it will respond with small deformations and internal stresses. Thus, one may define the stress tensor $\boldsymbol{\sigma} = \sigma_{ij} e_i e_j$ in the deformed configuration, which is characterized by the tension vector t_i on a generic surface [19], given by

$$t_i = \sigma_{ij} n_j \tag{2.2}$$

where n_j represents the unit vector normal to the considered surface.

Consider a body in equilibrium within a closed sub-domain Ω with surface S, subjected to surface forces **t** applied to the boundary surface Γ_t and body forces F, as illustrated in Figure 2.1.

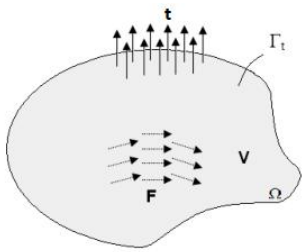

Figure 2.1: Body and surface forces acting on a body in equilibrium (source [20]).

The governing equations of the distribution of the stress tensor within a body may be deduced from the general concept of conservation of linear momentum, resulting in

$$\int_{\Gamma_t} T dA + \int_V F_i dV = \int_V \rho \ddot{u}_i dV \tag{2.3}$$

where ρ is the mass density, V is the volume of Ω, T represents the surface forces, F_i stands for the body forces and $\ddot{u}_i$ is the displacement's second order derivative with respect to time, in index notation. Substituting Equation 2.2 in 2.3 and applying the Divergence theorem of Gauss, results on

$$\int_V \sigma_{ji,j} n_j dV + \int_V F_i dV = \int_V (\sigma_{ji,j} n_j + F_i) dV = \int_V \rho \ddot{u}_i dV \tag{2.4}$$

Since it is valid in any arbitrary infinitesimal volume, Equation 2.4 may be written in differential form (strong form) which corresponds to the Cauchy theorem,

$$\sigma_{ji,j} + F_i = \rho \ddot{u}_i \tag{2.5}$$

In these conditions, the elasticity tensor E_{ijkl} establishes the linear constitutive behaviour between the strain tensor and stress tensor [19],

$$\sigma_{ij} = E_{ijkl} \varepsilon_{kl} \tag{2.6}$$

The elasticity tensor is independent of strain and stress and, for isotropic materials, can be given by the following expression,

$$E_{ijkl} = \lambda \delta_{ij} \delta_{kl} + \mu (\delta_{ik} \delta_{jl} + \delta_{il} \delta_{jk}) \tag{2.7}$$

where λ and μ are the Lamé constants used to characterize the properties of an isotropic material and are related to the Young's modulus E and Poisson's ratio ν by

$$\lambda = \frac{E\nu}{(1+\nu)(1-2\nu)} \tag{2.8}$$

$$\mu = \frac{E}{2(1+\nu)} = G \tag{2.9}$$

Here G is the transversal modulus of elasticity. Substituting Equations 2.8 and 2.9 in 2.6, one obtains

$$\sigma_{ij} = \lambda \varepsilon_{kk} \delta_{ij} + 2\mu \varepsilon_{ij} \tag{2.10}$$

which represents Hook's Law applied to an elastic, isotropic material. The equation of motion defined in 2.5 can be rewritten in terms of displacements as

$$G\nabla^2 u_i + (\lambda + G)\frac{\partial e}{\partial x_i} + f_i = \rho \frac{\partial^2 u_i}{\partial t^2} \tag{2.11}$$

where the Laplace operator is represented by $\nabla^2 = \frac{\partial^2}{\partial x^2} + \frac{\partial^2}{\partial y^2} + \frac{\partial^2}{\partial z^2}$, and $e = \frac{\partial u_j}{\partial x_j}$ is the divergence operator. Equation 2.11 is designated as the Navier's elastodynamics equation . Due to its complexity, one can determine the analytical solution only for particular cases where the body's geometry and boundary conditions are well established [19].

2.2 Finite Element Method

The numerical method used in this work to analyse the rotating structure is the finite element method (FEM). It consists of an analysis in which a continuous domain (Ω) is divided into smaller elements with the same properties of the original system, called sub-domains (Ω_e). Together, the elements give shape to the system's mesh and are connected through specific points (nodes), Figure 2.2. The solution is obtained at these nodes in the form of discrete values denominated generalized coordinates or degrees of freedom (DOF). Since this work focuses on structural problems, the generalized coordinates are likely to be displacements, rotations and related stresses and strains [21].

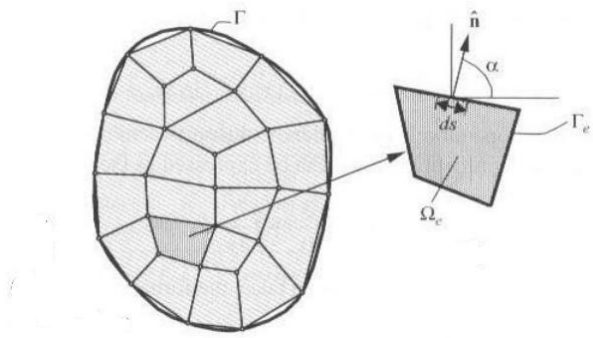

Figure 2.2: Discretization of an irregular domain Ω into several sub-domains Ω_e (with the unit normal $\hat{n}$ on the boundary Γ_e of an element) (source: [21]).

The FEM is usually based on techniques such as the residual method in order to determine the weak form of the problem or on the Galerkin method to acquire an array of equation that describes the system's behaviour. Considering the case of the elastodynamics problem 2.5 with essential boundary conditions $u = u_{given}$ in Γ_d and natural boundary conditions $t = t_{given}$ in Γ_t, and applying the principle

of virtual displacements [22], one has:

$$\delta\varepsilon_{ij} = \frac{1}{2}(\delta u_{i,j} + \delta u_{j,i}) \tag{2.12}$$

To determine the weak formulation of the elasticity problem 2.5 established in the previous section [21]

$$\int_{\Omega} \delta u_i \rho \ddot{u}_i d\Omega + \int_{\Omega} \delta\varepsilon_{ij}\sigma_{ij} d\Omega - \int_{\Omega} \delta u_i F_i d\Omega - \int_{\Gamma_t} \delta u_i t_i d\Gamma = 0 \tag{2.13}$$

The Galerkin method applied for finite elements and virtual displacements can be given by [21],

$$u = \sum_{\alpha} N_\alpha u_\alpha, \tag{2.14}$$

$$\delta u = \upsilon = \sum_{\beta} N_\beta \upsilon_\beta, \tag{2.15}$$

where N_α stands for the shape function specific for each finite element and the indices $\alpha, \beta = 1, 2, ..., NDOF$ are related to the N degrees of freedom of the element, where $NDOF$ is the total number of $DOFs$. Substituting Equations 2.14 and 2.15 in expression 2.13, one obtains the equation of motion in matrix form [21],

$$\{\upsilon\}^T([M]^e\{\ddot{u}^e\} + [K]^e\{u^e\}) = \{\nu\}^T\{F^e\} \tag{2.16}$$

with the system's mass matrix $[M]^e$, the stiffness matrix $[K]^e$ and the force vector $\{F^e\}$ applied to each element. Combining the individual elements of the domain, it is possible to assemble each of the global matrices.

Considering the case of an harmonic excitation, one has the following expressions for the force and displacement vector,

$$F = \bar{F}e^{i\omega_{ap}t}, \tag{2.17}$$

$$u = \bar{U}e^{i\omega_{ap}t}, \tag{2.18}$$

where ω_{ap} represents the applied excitation frequency, $\bar{F}$ is the force amplitude and $\bar{U}$ stands for the displacement amplitude. Thus, it is possible to conduct an analysis in free vibration (2.19) with the modal amplitude $\{u\} = \{\psi\}e^{i\omega_n t}$, where ω_n is the natural frequency of the system, as well as an harmonic vibration (2.20), by [23]

$$[K\{\psi\} - \omega_n^2 M\{\psi\}] = \{0\}, \tag{2.19}$$

$$[K\{\bar{U}\} - \omega_{ap}^2 M\{\bar{U}\}] = \{\bar{F}\}. \tag{2.20}$$

2.3 Dynamic Analysis of Systems with MDOF

In most cases, structures are continuous systems defined by elastic and non-homogeneous elements, thus their representation at every moment requires an infinite number of $DOFs$, becoming a discreet system of multiple degrees of freedom ($MDOF$) [14].

Considering the example of a damped system with N degrees of freedom, one realises that the $MDOF$ system needs N coordinates to characterize the position of the N masses relatively to its equilibrium position, as shown Figure 2.3.

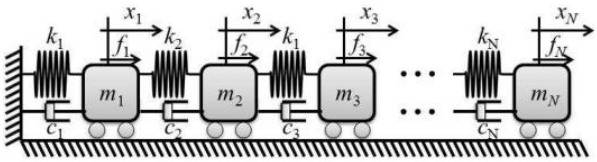

Figure 2.3: System with multiple degrees of freedom, $MDOF$ [14].

The m_i represents the system's mass, c_i is the damping coefficient, k_i is the stiffness, f_i stands for the force applied and x_i is the generalized coordinate. The structure's response is defined by N second order differential equations coupled for N movement coordinates. The system can be represented by the following equation of motion,

$$[M]\{\ddot{x}\} + [C]\{\dot{x}\} + [K]\{x\} = \{F\} \tag{2.21}$$

where $\boldsymbol{M}$ represents the mass matrix, $\boldsymbol{C}$ is the damping Matrix, $\boldsymbol{K}$ stands for the stiffness matrix and $\boldsymbol{F}$ symbolizes the force vector. The acceleration, velocity and displacement vectors are characterized by $\ddot{x}$, $\dot{x}$ and x respectively.

2.3.1 Modal Analysis

Modal Analysis is an essential tool used to study the dynamic properties of a structure, which is independent of external forces applied to the system as well as its dynamic response. This type of analysis consists in the determination of natural frequencies, vibration modes and modal dampening in free vibration conditions [15].

The natural frequency, as the name implies, is the frequency at which the system resonates. Resonances conditions are determined by the material properties (mass, stiffness and damping properties) and the structure's boundary conditions, where each mode is defined by its own natural frequency, modal dampening and mode shape [16]. For example, if the structure's mass is increased, its natural frequencies and modes should change. While a system composed by a single degree of freedom ($SDOF$) has an unique natural frequency, a $MDOF$ system composed by N degrees of freedom will demonstrate N

natural frequencies. One may consider the following equation of motion of an undamped system with no applied forces,

$$[M]\{\ddot{x}\} + [K]\{x\} = 0 \tag{2.22}$$

with the system's mass $\boldsymbol{M}$ and stiffness $\boldsymbol{K}$. The solution for Equation 2.22 can be given by,

$$\{x(t)\} = \{\bar{X}\}e^{i\omega t} \tag{2.23}$$

where $\{\bar{X}\}$ represents the response's amplitude. Replacing Equation 2.23 in 2.22, results in:

$$\left[[K] - \omega^2[M]\right]\{\bar{X}\} = 0 \tag{2.24}$$

Equation 2.24 represents a generalized problem of eigenvalues and eigenvectors. Aside from the trivial solution, which corresponds to the stationary response, the non-trivial solution is given by,

$$det\left[[K] - \omega^2[M]\right] = 0 \tag{2.25}$$

where det represents the determinant of the given matrix. Solving Equation 2.25, one can obtain N eigenvalues that represent the system's N natural frequencies $\omega_1, \omega_2, ...\omega_N$. Substituting each natural frequency in 2.24 and solving each system of equations, one acquires the eigenvectors $\{\Psi_r\} = \{\psi_1, \psi_2, ...\psi_N\}$ of the dynamic system, which represent its N vibration modes associated with the respective N natural frequencies ω_r, (r labels the mode). Thus, the solution of a system in free vibration may be represented in the following matrix form,

$$[\omega_r^2] = \begin{bmatrix} \omega_1^2 & 0 & \cdots & 0 \\ 0 & \omega_2^2 & \cdots & 0 \\ \vdots & \vdots & \ddots & \vdots \\ 0 & 0 & \cdots & \omega_N^2 \end{bmatrix} \tag{2.26}$$

$$[\Psi] = [\{\psi_1\}, \{\psi_2\}, ..., \{\psi_N\}] \tag{2.27}$$

Since both matrices $\boldsymbol{M}$ and $\boldsymbol{K}$ are symmetric and the eigenvectors are orthogonal, one may deduce the following relations:

$$[\Psi]^T[M][\Psi] = [M_r], \tag{2.28}$$

$$[\Psi]^T[K][\Psi] = [K_r]. \tag{2.29}$$

The vibration modes are usually normalized by the following equation:

$$\{\gamma_r\Psi_r\}^T[M]\{\gamma_r\Psi_r\} = 1, \tag{2.30}$$

with

$$\gamma_r = \frac{1}{\sqrt{\{\Psi_r\}^T[M]\{\Psi_r\}}} = \frac{1}{\sqrt{M_r}}. \tag{2.31}$$

The normalized modal matrix may be defined by,

$$[\varphi_r]^T[M][\varphi_r] = [I], \tag{2.32}$$

$$[\varphi_r]^T[K][\varphi_r] = [\omega_r^2], \tag{2.33}$$

where $[I]$ represents the identity matrix. For the case of a system with viscous damping, Equation 2.22 changes to:

$$[M]\{\ddot{x}\} + [C]\{\dot{x}\} + [K]\{x\} = 0 \tag{2.34}$$

Substituting Equation 2.23 in 2.34, results in:

$$\left[[K] - \omega^2[M] + i\omega[C]\right]\{X_0\} = 0 \tag{2.35}$$

A particular case is to consider that the viscous damping matrix is proportional to the stiffness and mass matrices (Rayleigh damping) through a linear combination between both [24],

$$[C] = a[K] + b[M] \tag{2.36}$$

where a and b are constants. In these conditions, the damping factor (ξ_r) may be characterized for each mode r, using the following expression:

$$\xi_r = \frac{b}{2\omega_r} + \frac{a\omega_r}{2} \tag{2.37}$$

As for the modal matrix, it can be defined as:

$$[\varphi_r]^T[C][\varphi_r] = [\varphi_r]^T[a[K] + b[M]][\varphi_r] = [2\xi_r\omega_r] \tag{2.38}$$

These properties can be helpful to solve equation 2.34, as such, the equation of motion may be rewritten in terms of modal coordinates $q(t)$ by using the following transformation:

$$\{x(t)\} = [\varphi_r]\{q(t)\} \tag{2.39}$$

For a more detailed study about modal analysis one may consult [15].

2.3.2 Harmonic Analysis

In harmonic analysis, here is considered that the system is submitted to external dynamic forces which constitute the force vector $\{F(t)\}$. These harmonic excitations may be applied to a single DOF or every $DOFs$ as long as their excitation frequency ω is equal to all of them [15].

$$\{F(t)\} = \{F_0\}e^{i\omega_{ap}t} \tag{2.40}$$

Here, ω is the applied force frequency [rad/s] and F_0 represents the force amplitude [N]. Substituting Equations 2.40 and 2.23 in Equation 2.22 while still considering the case of an undamped system ($C = 0$), it results:

$$\left[[K] - \omega^2[M]\right]\{\bar{X}\} = \{F_0\} \tag{2.41}$$

Furthermore, one can obtain the system's response in coordinate j due to an excitation force applied in coordinate k for a $MDOF$ system, using the following expression:

$$H_{jk}(\omega) = \frac{X_j}{F_k} = \sum_{r=1}^{N} \frac{{}_rA_{jk}}{\omega_r^2 - \omega^2} \tag{2.42}$$

In the previous expression, $H_{jk}(\omega)$ represents the receptance function which gives the ratio between the displacement amplitude at point j and the excitation force amplitude at coordinate k. The modal constant ${}_rA_{jk}$ is given by the following expression, where m_r stands for the modal mass respective to mode r.

$${}_rA_{jk} = \left|\frac{\bar{X}_{jr}\bar{X}_{kr}}{m_r}\right| \tag{2.43}$$

Considering the case of a damped system, the system's receptance is given by

$$H_{jk}(\omega) = \frac{X_j}{F_k} = \sum_{r=1}^{N} \frac{{}_rA_{jk}}{\omega_r^2 - \omega^2 + i2\xi_r\omega\omega_r} \tag{2.44}$$

Here, $i = \sqrt{-1}$ is the complex unity. An important aspect to consider is that the receptance matrix $\boldsymbol{H}$ is symmetric. Thus it is possible to establish the following relation (known as the reciprocity theorem [15])

$$H_{jk}(\omega) = \frac{X_j}{F_k} = H_{kj}(\omega) = \frac{X_k}{F_j}. \tag{2.45}$$

2.3.3 Spatial, Modal and Response Model

According to the topics discussed in the previous sections, one may define three types of models (Spatial, Modal and Response) for a $MDOF$ system, as illustrated in Figure 2.4.

The Spatial Model controls the system's spatial characteristics given by the matrices $[M]$, $[K]$ and $[C]$, in the time domain. It allows to study the response in time including transient analysis, etc.

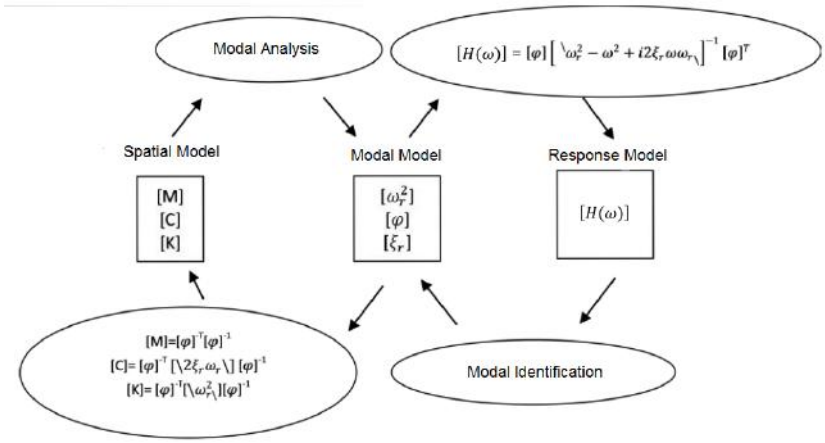

Figure 2.4: Relation between the three dynamic models (source [15]).

The Modal Model is defined by the system's modal properties, such as the natural frequency ω_r, the modal dampening ξ_r and the vibration modes ψ_r. One can determine the Spatial Model through the Modal Model using Equations 2.34, 2.35 and 2.36. This is possible due to the fact that the modal vectors are linearly independent, therefore matrix $[\Phi_r]$ becomes regular and consequently invertible [15].

Regarding the Response Model, it may also be related to the Modal Model as it can be observed in Equation 2.44, which contains modal parameters,

$$[H(\omega)] = [\varphi_r][\omega_r^2 - \omega^2 + i2\xi_r\omega\omega_r]^{-1}[\varphi_r]^T \tag{2.46}$$

One of the Response Model's main advantages is the development of models that are too complex to be solved analytically, resorting to experimental analysis through the receptance matrix $H_{jk}(\omega)$ (2.44). Each one of the matrix elements corresponds to a frequency response function (FRF) which represents the ratio between the measured response at point j and the excitation applied at point k.

2.3.4 Frequency Domain Analysis

Observing the previous section, one realizes that dynamic models may be represented in both time and frequency domain. This work is focused on the frequency domain.

The most common tool used to transform time signals into the frequency domain is called the Fast Fourier Transform (FFT). Figure 2.5 illustrates how a square wave can be constructed by adding up a series of sine waves. Each of the sine waves has a frequency that is a multiple of the square wave's frequency. The frequency of each tone is represented by the location of each peak on the coordinate in the horizontal axis and the amplitude of each sine tone is represented by the height of each peak on the vertical axis [25].

As it was already mentioned, the most common representation used to describe the output response of a structure, due to an applied force in the frequency domain, is the FRF (Frequency Response Function). The most frequently used FRF is the Receptance Matrix (2.44), which is utilized to study the structure's response in terms of displacement [15]. In the case of velocity response it is the Mobility

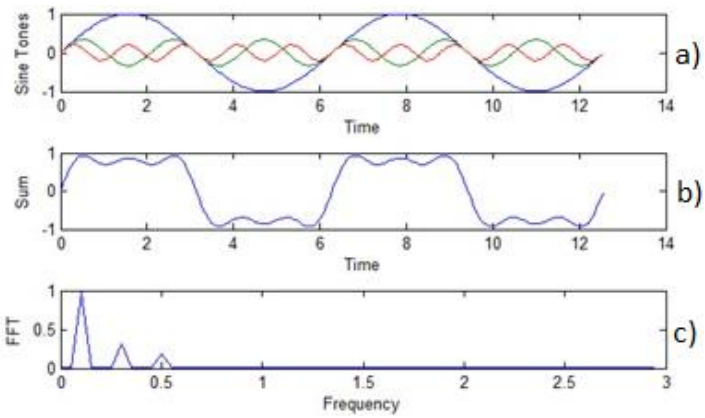

Figure 2.5: Transformation from the time domain to the frequency domain using FFT: a) sine waves; b) square wave; c) amplitude of each of the sine tones (source [25]).

Matrix (2.47) and for the acceleration one has the Accelerance Matrix (2.48),

$$M_{jk}(\omega) = \frac{i\omega X_j}{F_k} = i\omega H_{jk}(\omega), \tag{2.47}$$

$$A_{jk}(\omega) = \frac{-\omega^2 X_j}{F_k} = -\omega^2 H_{jk}(\omega). \tag{2.48}$$

A typical representation of a FRF is illustrated in Figure 2.6. While plotting the amplitude of response of a system in frequency domain, important information is obtainable about the dynamic characteristics of the structure. A peak point in this diagram demonstrates the resonant frequencies of the structure, while an inverted peak point represents an anti-resonance frequency. Around these points, structural damping is dominant. The magnitude values are normally displayed in logarithmic scale (dB), since the linear scale may not properly show the structure's behaviour at lower levels of magnitude.

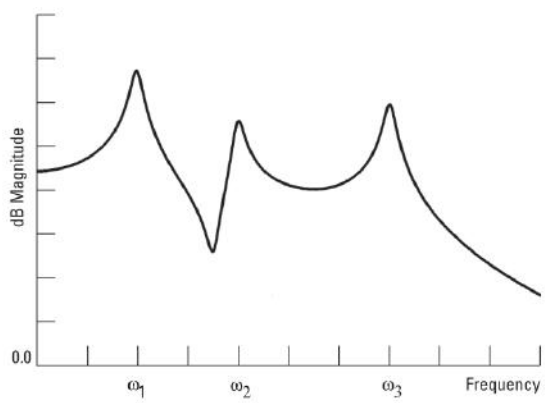

Figure 2.6: Example of a FRF plot (source [26]).

2.4 Rotordynamics Concepts

In this section, the main concepts and terminology of rotordynamic are introduced in order to provide a better insight of the rotor system behaviour. Before providing a general description of the rotating machinery physical properties, a study model is deduced. This model is simplified into several elementary parts that will be studied in this section, which include the rigid disk, flexible shaft, bearings and the mass unbalanced. Based on this model, several rotordynamic analysis are examined providing results that are important to describe the lateral dynamic behaviour of rotors, providing the reader a good introduction to the rotordynamic subject.

2.4.1 Elements of the Rotor System

As mentioned earlier rotor systems can be simplified into four basic components, the disk, the shaft, the bearings and the mass unbalanced. This model is based on the one used by Lalanne and Ferraris [3] and some simplifications and assumptions were used to characterize each part of the model. It implements the kinetic and strain energies of the components, as well as the external forces virtual work to compute the system's energy equation and external force's work. Some simplifications and assumptions were used to characterize each part of the model. Thus, applying the Lagrange Equation 2.49 it is possible to obtain the system's equation of motion.

$$\frac{d}{dt}\left(\frac{\delta T}{\delta \dot{q}_i}\right) - \frac{\delta T}{\delta q_i} + \frac{\delta U}{\delta q_i} = \frac{\delta W}{\delta q_i} = F_{q_i} \tag{2.49}$$

Here the index i represents the number of degrees of freedom, q_i indicates the system corresponding generalized coordinates, δW symbolizes the virtual work produced by non-conservative forces acting on the system along a virtual displacement δq_i and F_{q_i} are the generalized loads. From Equation 2.49 one can recognize the importance of computing the disk, shaft and mass unbalance kinetic energy T and the shaft's strain energy U, since this model only considers the shaft component as flexible. The next sections present the calculation of the energies associated with each part of the system.

The Rigid Disk

During this work, the disk is considered as a rigid body, implying that the kinetic energy is the only energy that characterizes this component. According to Genta [1], this approximation is very reasonable in most cases since the resulting error is extremely small when compared with the real solution.

To analyse the disk's behaviour, one used a non-inertial reference frame that rotates synchronously with the disk's spin and its use is associated with the appearance of gyroscopic effects. This type of rotating frame is mostly used by dynamic systems involving rotating components since its main advantage is the possibility to avoid periodic terms conditioned by time.

Figure 2.7 represents the disk's geometry, where $R[m]$ stands for the external disk radius, $r[m]$ is the inner radius, $h[m]$ corresponds to the disk thickness and lastly $\rho_D[\frac{Kg}{m^3}]$ is the disk material density.

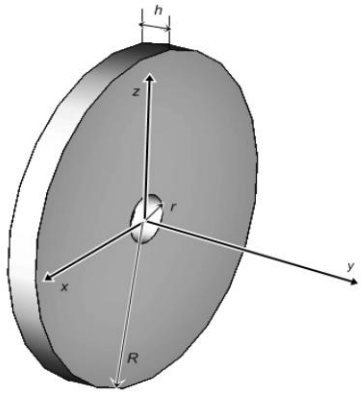

Figure 2.7: Disk model (source [4]).

Taking into account the disk geometry and the material properties, the mass M_D [kg] and inertia tensor I_D [$kg.m^2$] are given by

$$M_D = \rho_D \pi (R^2 - r^2) h, \tag{2.50}$$

$$I_D = \begin{bmatrix} I_{Dx} & 0 & 0 \\ 0 & I_{Dy} & 0 \\ 0 & 0 & I_{Dz} \end{bmatrix} \tag{2.51}$$

where:

$$I_{Dx} = I_{Dz} = \frac{M_D}{12}(3R^2 + 3r^2 + h^2) \tag{2.52}$$

$$I_{Dy} = \frac{M_D}{2}(R^2 + r^2) \tag{2.53}$$

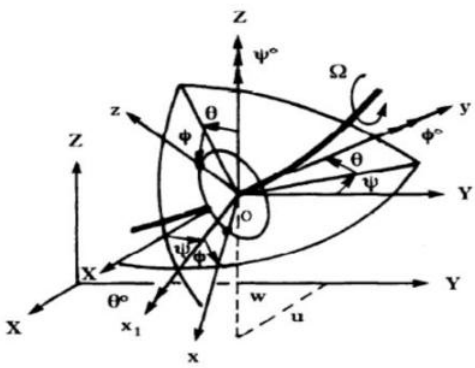

Figure 2.8: The Disk and its reference frame (source [3]).

Figure 2.8 displays two distinct reference frames located at the disk's center, a fixed rotating frame $R(x, y, z)$ to represent the referential that rotates with the rotor's angular speed Ω and a inertial reference frame $R_0(X.Y, Z)$ where the system's equation of motion is defined. The instantaneous angular velocity

vector of the xyz frame is given by

$$\vec{\omega}_{R/R_0} = \dot{\psi}Z + \dot{\theta}x_1 + \dot{\phi}y \tag{2.54}$$

Considering the relation between both reference frames, it is possible to obtain the angular speed vector about the disk center of mass as

$$\vec{\omega}^R_{R/R_0} = \begin{bmatrix} \omega_x \\ \omega_y \\ \omega_z \end{bmatrix} = \begin{bmatrix} -\dot{\psi}\cos\theta\sin\phi + \dot{\theta}\cos\phi \\ \dot{\phi} + \dot{\psi}\sin\theta \\ \dot{\psi}\cos\theta\cos\phi + \dot{\theta}\sin\phi \end{bmatrix} \tag{2.55}$$

where the rate of nutation θ, rate of spin ψ and rate of precession ϕ are referred to as the Euler angles and $\dot{\theta}$, $\dot{\psi}$ and $\dot{\phi}$ represent the time derivatives respectively. Considering the displacements u and w of the disk's center of mass along X and Z directions on the inertial reference frame, the disk kinetic energy is given by

$$T_D = \frac{1}{2}M_D(\dot{u}^2 + \dot{w}^2) + \frac{1}{2}(I_{Dx}\omega_x^2 + I_{Dy}\omega_y^2 + I_{Dz}\omega_z^2) \tag{2.56}$$

Expressions 2.55 and 2.56 may be simplified for a symmetric disk ($I_{Dx} = I_{Dz}$). Considering that the angles θ and $\dot{\psi}$ are small ($\cos(\theta) \approx 1, \sin(\theta) \approx \theta, \sin(\theta)^2 \approx 0$) and a constant angular velocity $\dot{\phi} = \Omega$

$$\begin{bmatrix} \omega_x \\ \omega_y \\ \omega_z \end{bmatrix} = \begin{bmatrix} -\dot{\psi}\phi + \dot{\theta} \\ \Omega + \dot{\psi}\theta \\ \dot{\psi} + \dot{\theta}\phi \end{bmatrix} \tag{2.57}$$

Applying expression 2.57 in the kinetic energy results one obtains

$$T_D = \frac{1}{2}M_D(\dot{u}^2 + \dot{w}^2) + \frac{1}{2}I_{Dx}\left(\dot{\theta}^2 \underbrace{-2\dot{\psi}\phi\dot{\theta} + 2\dot{\psi}\phi\dot{\theta}}_{=0} + \underbrace{(\dot{\psi}\phi)^2}_{\approx 0} + \underbrace{(\phi\dot{\theta})^2}_{\approx 0} + \dot{\psi}^2\right) + \frac{1}{2}I_{Dy}\left(\Omega^2 + 2\Omega\dot{\psi}\theta + \underbrace{(\dot{\psi}\theta)^2}_{\approx 0}\right) \tag{2.58}$$

giving the following expression for the kinetic energy of the disk:

$$T_D = \frac{1}{2}M_D(\dot{u}^2 + \dot{w}^2) + \frac{1}{2}I_{Dx}(\dot{\theta}^2 + \dot{\psi}^2) + \frac{1}{2}I_{Dy}(\Omega^2 + 2\Omega\dot{\psi}\theta) \tag{2.59}$$

where the term $I_{Dy}\Omega\dot{\psi}\theta$ represents the gyroscopic effect.

Flexible Shaft

The shaft will be modelled as a flexible beam with circular cross-section composed by an isotropic, homogeneous material with no internal damping and following a linear behaviour. Figure 2.9 represents the shaft's cross-section along with two reference frames, the rotating reference frame coincident with the cross-section center, defined by the displacements u^* and w^* along the x and z axis and the inertial frame with displacements u and w along the X and Z axis.

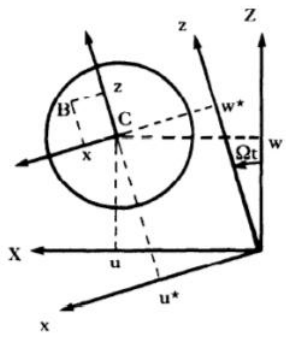

Figure 2.9: Cross section of the shaft (source [3]).

The shaft's kinetic energy can be defined in a similar way as the disk's with a slight variation, since it will be applied to an element with length L [m]:

$$T_S = \frac{\rho S}{2}\int_0^L (\dot{u}^2 + \dot{w}^2)dy + \frac{\rho I}{2}\int_0^L (\dot{\theta}^2 + \dot{\psi}^2)dy + \rho I L \Omega^2 + 2\rho I \Omega \int_0^L \dot{\psi}\theta dy \tag{2.60}$$

where ρ represents the shaft's material density, S [m^2] is the shaft's cross-section area and I [m^4] denotes the second moment of area of the shaft's cross-section. Analysing equation 2.60, one recognizes that the first term is the kinetic energy of a bending beam (associated with transversal deformation), the second term is the secondary effect of rotary inertia (associated with rotation of shaft rotation), consistent with Timoshenko beam theory, and the last term symbolizes the gyroscopic effect.

Considering the shaft as an elastic body (coherent with Hook's Law) and including the strain caused by both the rotation of the shaft and a constant axial force F_0 applied at both ends of the shaft (in O_y directions), it is possible to compute the strain energy U_S for a shaft of constant cross-section as follows

$$U_S = \frac{EI}{2}\int_0^L \left[\left(\frac{\partial^2 u}{\partial y^2}\right)^2 + \left(\frac{\partial^2 w}{\partial y^2}\right)^2\right] dy + \frac{F_0}{2}\int_0^L \left[\left(\frac{\partial u}{\partial y}\right)^2 + \left(\frac{\partial w}{\partial y}\right)^2\right] dy \tag{2.61}$$

The strain energy caused by the transversal (bending) deformation of the shaft is present in the first term of equation 2.61. This longitude strain, due to the rotation of the points located at the shaft's cross-section, is considered to be approximately linear, since the displacements are small and the cross-section is symmetric relatively to the rotating reference frame.

The second term of the strain energy equation is associated with the longitudinal (traction/compression) strain resultant from an axial force. This longitudinal strain includes only non-linear terms and the associated energy. Although, important for stability considerations, these are out of scope of this work.

Bearings

Almost all rotor machinery is supported by some type of bearings as they are responsible for maintaining the axis of rotation in a defined position in space and providing non-rotating damping to the system's vibration and stability. These components can be classified as being symmetric or asymmetric, rigid or elastic and damped or undamped. During this work, the bearing's stiffness and viscous damping

are assumed already known.

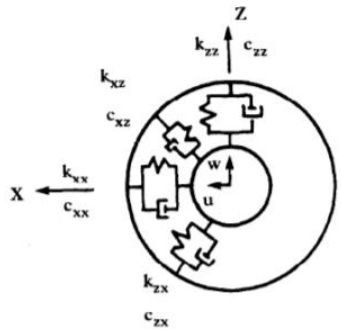

Figure 2.10: The bearing model (source [3]).

Figure 2.10 shows the bearing model used, where c_{xx}, c_{zz} and c_{xz} stands for the dampers in the respective directions and k_{xx}, k_{zz} and k_{xz} represent the stiffness in the respective direction. Since this model is composed by springs and dampeners, the virtual work of the forces acting on the bearings should be used to compute the displacements.

$$\delta W = F_u \delta_u + F_w \delta_w \tag{2.62}$$

$$\delta W = -k_{xx} u \delta u - k_{xz} w \delta u - k_{zz} w \delta w - k_{zx} u \delta w - c_{xx} \dot{u} \delta u - c_{xz} \dot{w} \delta u - c_{zz} \dot{w} \delta w - c_{zx} \dot{u} \delta w \tag{2.63}$$

Combining equation 2.62 with 2.63, and eliminating the virtual displacements, results in the following expression in matrix form

$$\begin{bmatrix} F_u \\ F_w \end{bmatrix} = - \begin{bmatrix} k_{xx} & k_{xz} \\ k_{zx} & k_{zz} \end{bmatrix} \begin{bmatrix} u \\ w \end{bmatrix} - \begin{bmatrix} c_{xx} & c_{xz} \\ c_{zx} & c_{zz} \end{bmatrix} \begin{bmatrix} \dot{u} \\ \dot{w} \end{bmatrix} \tag{2.64}$$

Mass Unbalance

The mass unbalance may be modelled as a punctual mass m_u located at a distance d from the shaft center in a plane perpendicular to the YY axis.

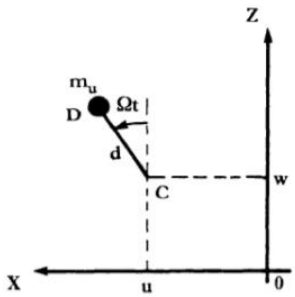

Figure 2.11: Rotating mass with offset length (source [3]).

From Figure 2.11, it is possible to deduce the coordinates of the mass in the inertial reference frame:

$$\bar{OD} = \begin{pmatrix} u + d\sin\Omega t \\ const \\ w + d\cos\Omega t \end{pmatrix} \tag{2.65}$$

Vector of speed V of the punctual mass can be computed, giving:

$$V = \frac{d(\bar{OD})}{dt} = \begin{pmatrix} \dot{u} + \Omega d\cos\Omega t \\ 0 \\ \dot{w} - \Omega d\sin\Omega t \end{pmatrix} \tag{2.66}$$

Finally, the kinetic energy expression for the mass unbalance becomes

$$T_u = \frac{m_u}{2}(\dot{u}^2 + \dot{w}^2 + \Omega^2 d^2 + 2\Omega\dot{u}d\cos\Omega t - 2\Omega\dot{w}d\sin\Omega t) \tag{2.67}$$

Using expression 2.67 and considering that the punctual mass m_u is much smaller than the rotor's mass, the kinetic energy of a punctual mass is as follows:

$$T_u \cong m_u\Omega d(\dot{u}\cos\Omega t - \dot{w}\sin\Omega t) \tag{2.68}$$

2.4.2 Whirling motion

Since rotor systems are dynamic by nature, it is important to contemplate the vibration effects to characterize the rotor's performance. Considering the case of horizontal rotors, these are assumed to vibrate in two directions, vertical and horizontal, generating whirl orbits. The most frequent reason for rotor whirling is rotor unbalance, since rotating machinery can never be perfectly balanced in practice, although, different causes may be responsible for rotor whirling such as: gyroscopic forces and moments, bearings, damping, among other factors.

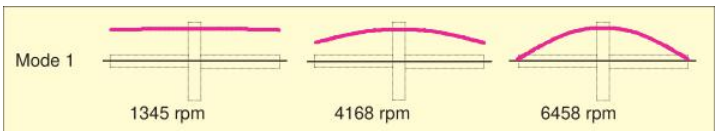

Figure 2.12: First mode shape and respective natural frequencies (in rpm) versus bearing stiffness, shaft not rotating in a lateral view (source [27]).

To have a more comprehensive insight on the whirling experience, lets consider the first mode shape of three different versions of a rotor (Figure 2.12), each with soft, intermediate and stiff bearings. At each frequency, the motion is planar just as a pinned-pinned beam which is expected from a static structure. Additionally, the ratio between bearing stiffness and shaft stiffness influences the mode-shapes, as the bearing stiffness increases (or the shaft stiffness decreases), the amount of shaft bending increases.

Considering now a rotating shaft, it is noticeable that the shape of motion has changed. However, the frequencies are similar to the non-rotating first mode. This new mode involves circular motion rather than

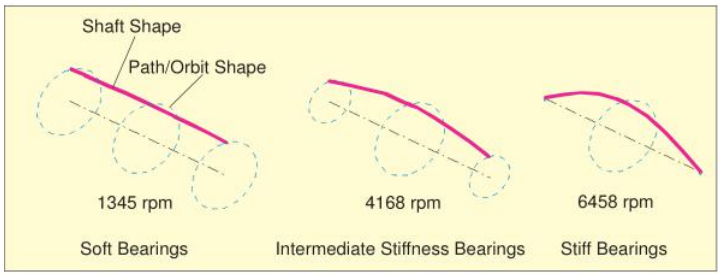

Figure 2.13: Shaft rotating, 1st mode shapes in perspective and respective natural frequencies (in rpm) (source [27]).

planar motion creating whirling orbits as it is seen in Figure 2.13. This rotation can be called ”Forward Whirl” (FW) if the rotor moves in the same direction as the shaft’s whirl, or ”Backward Whirl” (BW) if the rotor rotates in the opposite direction.

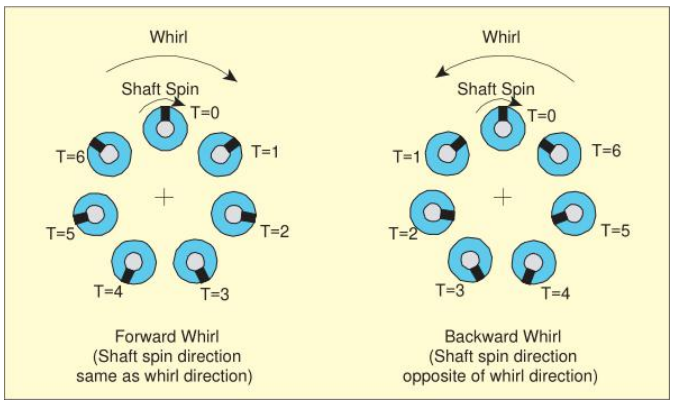

Figure 2.14: Whirl sense (source [27]).

Examining Figure 2.14, one can observe rotor cross section over time for FW and BW. In case of forward whirl, a point on the surface of the rotor represented as a black marked area remains outside of the whirl orbit during the whole motion, while on the opposite case with backward whirl, the black marked area alternates from inside to outside of the whirl orbit. This change in direction of the surface point creates alternate tensile stresses (tensile loading and compression) leading to the fatigue of the rotor machinery, highlighting therefore the importance of whirling motion analysis in rotordynamics.

2.4.3 Campbell Diagram

Knowing that the equation of motion clearly depends on the spin speed of the rotor, the natural frequencies will also depend on Ω. Figure 2.15 presents a plot of the rotor natural frequencies in Hz over a wide shaft spin speed in rpm, where the blue line, starting at (0,0), represents the linear function $\omega = f(\Omega)$, red line represents Forward Whirl and the purple line symbolizes Backward Whirl.

Analysing the Campbell diagram, one can observe two angular velocities corresponding to the intersection between the blue line and the purple/red lines. These spin speeds represent the eigenfrequencies of the shaft in function of the rotor velocity, which create increase vibration on the system conceiving considerable damage on the rotor leading possibly to its failure.

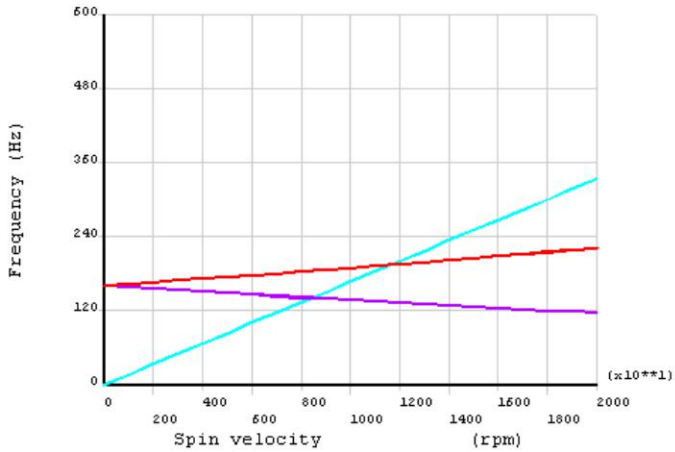

Figure 2.15: Example of a Campbell diagram.

2.4.4 Critical Speeds

There are many definitions for critical speeds, in particular the American Petroleum Institute (API), in API publication 684 (First Edition, 1996) [27], states that a critical speed is achieved "*when the synchronous rotor frequency equals the frequency of a rotor natural frequency, the system operates in a state of resonance, and the rotor's response is amplified if the resonance is not critically damped*", this resonance state translates to a rotor vibration when the frequency of the harmonic forcing function coincides with the natural frequency of the rotor system. In practice, when a rotor reaches a certain spin speed where the forcing function frequency matches with the system natural frequency, a properly placed sensor displays a distinct peak in response versus speed confirming that the machine has passed through a critical speed, Figure 2.16.

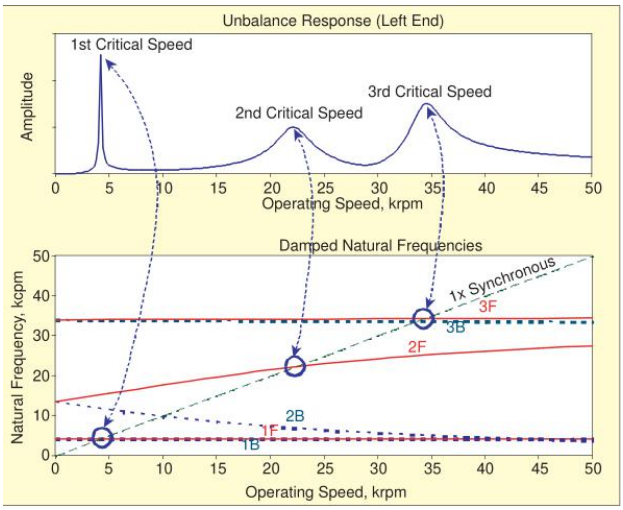

Figure 2.16: Natural frequencies and critical speeds (source [27]).

For increasing levels of damping on the system (through the use of different bearing), these critical speeds become noticeably different from how they are described by API, since these large amplitude peaks cease to exist as it is demonstrated in Figure 2.17.

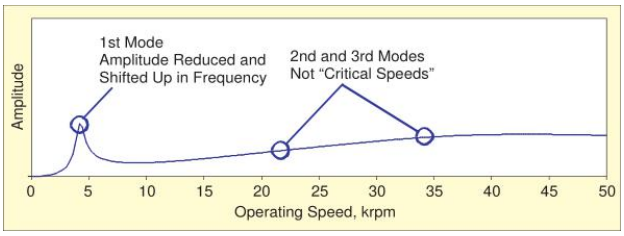

Figure 2.17: Critical speeds with additional bearing damping (source [27]).

Critical speeds are present in the Campbell's diagram (Figure 2.15) by identifying the points of intersection between the natural frequencies curves with a linear equation $\omega = \Omega$, representing the force frequencies during unbalance excitation. Therefore, the rotor speed range can be separated in two groups: the sub-critical range, which represents the spin speeds form zero to the first critical speed and the super-critical range occurs after the first critical speed. Most rotor machinery critical speeds are desired to be 0.1 to 0.2 above or below the operating speed range. However, there are many rotors that operate on top of the second critical speed due to sufficient bearing damping. Often attempts to elevate the 2nd critical speed by increased bearing stiffness may lead to serious 1st mode stability problems.

2.5 Numerical Aspects of Rotordynamics Finite Elements

This section introduces how the finite element method is applied to each rotor part, providing a numerical analysis of rotor models such as the mono-rotor. The method used follows the same line of thought made by Lalanne and Ferraris [3], starting by estimating the energy equations of each rotor element using the equations presented in section 2.4.1. Then, one proceeds to characterize the system's modal analysis and harmonic response.

2.5.1 Displacement vector

The first step is to define the displacement vector in order to implement the Lagrange equation 2.49 to each rotor part energy equation. The displacement vector is composed by 4 degrees of freedom per rotor node, two translation displacements u and w along the X and Z axis and two rotations, θ and ψ, about the same two axis. Considering an Euler-Bernoulli assumption on the beam deformation, the rotation can be related with the displacements through the following equations

$$\theta = \frac{\partial w}{\partial y}, \tag{2.69}$$

$$\psi = -\frac{\partial u}{\partial y}. \tag{2.70}$$

An important aspect to consider is that the axial and torsional DOFs are not contemplated, thus the displacement vector is given by:

$$\boldsymbol{\delta} = [u, w, \theta, \psi]^T. \tag{2.71}$$

2.5.2 The disk

As already mentioned, the disk is represented as a rigid body, thus it will be modelled as having only one node. The element matrices of the symmetric disk are derived by applying the Lagrange equation 2.49 to the kinetic energy expression 2.59. Additionally, if one introduces the displacement vector 2.71 in 2.49, it results in the following expression:

$$\frac{d}{dt}\left(\frac{\partial T}{\partial \dot{\delta}}\right) - \frac{\partial T}{\partial \delta} = \begin{bmatrix} M_D & 0 & 0 & 0 \\ 0 & M_D & 0 & 0 \\ 0 & 0 & I_{Dx} & 0 \\ 0 & 0 & 0 & I_{Dx} \end{bmatrix} \begin{bmatrix} \ddot{u} \\ \ddot{w} \\ \ddot{\theta} \\ \ddot{\psi} \end{bmatrix} + \Omega \begin{bmatrix} 0 & 0 & 0 & 0 \\ 0 & 0 & 0 & 0 \\ 0 & 0 & 0 & -I_{Dy} \\ 0 & 0 & I_{Dy} & 0 \end{bmatrix} \begin{bmatrix} \dot{u} \\ \dot{w} \\ \dot{\theta} \\ \dot{\psi} \end{bmatrix} \tag{2.72}$$

The first matrix represents the mass matrix of the disk and the second corresponds to the gyroscopic matrix which is dependent on the rotating speed Ω.

To describe the disk in the finite element software $ANSYS$, one used the MASS21 finite element [28], as a structural mass element, allowing the same behaviour as the one described above.

2.5.3 The shaft

The flexible shaft is modelled as a two node beam of length L with constant circular cross-section, see Figure 2.18. Since the modelled shaft is long and slender, the Euler-Bernoulli theory is used to study its behaviour, as already mentioned in 2.5.1. Another option to consider is the Timoshenko beam theory which is better used for shorter beams with larger cross-sections and considers the influence of the shear loads on the shaft and rotational inertia effects. Here a shear correction to the total stiffness is contemplated in the analysis.

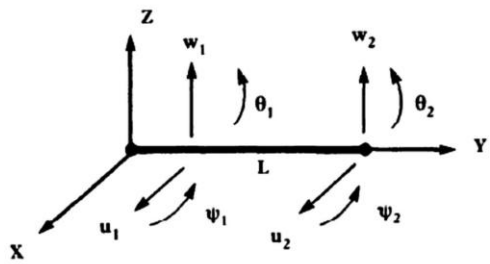

Figure 2.18: Shaft finite element (source [3]).

The nodal displacement vector for the shaft finite element is written as:

$$\delta = [u_1, w_1, \theta_1, \psi_1, u_2, w_2, \theta_2, \psi_2]^T \tag{2.73}$$

Relating the shape functions $N_i(y)$ with the displacements according to a Galerkin approximation, one can build the shaft finite element resorting to the following expressions:

$$u = N_1(y)\delta u \tag{2.74}$$

$$w = N_2(y)\delta w \tag{2.75}$$

where δu and δw represent the displacements contained in 2.73 in the X and Z directions respectively, as stated in the following equation:

$$\delta u = [u_1, \psi_1, u_2, \psi_2]^T \tag{2.76}$$

$$\delta w = [w_1, \theta_1, w_2, \theta_2]^T \tag{2.77}$$

In Equation 2.74 and 2.75, $N_1(y)$ and $N_2(y)$ are shape functions commonly used in a bending beam (Hermite interpolation) and are written as:

$$N_1(y) = \left[1 - \frac{3y^2}{L^2} + \frac{2y^3}{L^3}; -y + \frac{2y^2}{L} - \frac{y^3}{L^2}; \frac{3y^2}{L^2} - \frac{2y^3}{L^3}; \frac{y^2}{L} - \frac{y^3}{L^2}\right] \tag{2.78}$$

$$N_2(y) = \left[1 - \frac{3y^2}{L^2} + \frac{2y^3}{L^3}; y - \frac{2y^2}{L} + \frac{y^3}{L^2}; \frac{3y^2}{L^2} - \frac{2y^3}{L^3}; -\frac{y^2}{L} + \frac{y^3}{L^2}\right] \tag{2.79}$$

Combining expressions 2.74 and 2.75 and their derivatives with the shaft's kinetic energy equation 2.60, solving the integration and introducing the result expression in the Lagrange equation, one gets the final result for the two first terms of 2.49

$$\frac{d}{dt}\left(\frac{\partial T_S}{\partial \dot{\delta}}\right) - \frac{\partial T_S}{\partial \delta} = (M + M_S)\ddot{\delta} + C\dot{\delta} \tag{2.80}$$

where M, M_S and C are presented in Appendix A.

Following a similar procedure, substituting Equations 2.74 and 2.75 in the shaft's strain energy expression 2.61, expanding the integral operations and applying the Lagrange equation, it results:

$$\frac{\partial U}{\partial \delta} = (K_C + K_F)\delta \tag{2.81}$$

The matrix K_C stands for the classic stiffness matrix of the shaft and K_F represents the geometric stiffness matrix associated with the axial force acting of the shaft. Both matrices are listed in Appendix A.

To describe the shaft in the commercial finite element software ($ANSYS$), one used the Timoshenko beam theory (BEAM188 finite element [28]) with cubic interpolation.

2.5.4 The bearings

The bearing model used in the finite element analysis is governed by the same equations referred in section 2.4.1. By applying the displacement vector 2.71 in equation 2.64, the forces acting on bearings are computed, resulting in:

$$\begin{bmatrix} F_u \\ F_\theta \\ F_w \\ F_\psi \end{bmatrix} = - \begin{bmatrix} k_{xx} & 0 & k_{xz} & 0 \\ 0 & 0 & 0 & 0 \\ k_{zx} & 0 & k_{zz} & 0 \\ 0 & 0 & 0 & 0 \end{bmatrix} \begin{bmatrix} u \\ \theta \\ w \\ \psi \end{bmatrix} - \begin{bmatrix} c_{xx} & 0 & c_{xz} & 0 \\ 0 & 0 & 0 & 0 \\ c_{zx} & 0 & c_{zz} & 0 \\ 0 & 0 & 0 & 0 \end{bmatrix} \begin{bmatrix} \dot{u} \\ \dot{\theta} \\ \dot{w} \\ \dot{\psi} \end{bmatrix} \tag{2.82}$$

To describe the bearings in the commercial finite element software ($ANSYS$), one used a two dimensional longitudinal spring-damper element in the $X - Z$ plane (COMBIN14 finite element [28]), allowing the same behaviour as the one described above.

2.5.5 Mass Unbalanced

For this element, one applied the Lagrange equation 2.49 to the kinetic energy expression 2.68, resulting in the following mass finite element model:

$$\frac{d}{dt}\left(\frac{\partial T}{\partial \dot{\delta}}\right) - \frac{\partial T}{\partial \delta} = -m_u \Omega^2 d \begin{bmatrix} \sin(\Omega t) \\ \cos(\Omega t) \end{bmatrix}, \delta = [u, w]^T \tag{2.83}$$

From equation 2.83, it is clear that the mass unbalance effect acts along the two translations in the XZ plane.

2.5.6 Modal Analysis and Campbell Diagram

Having introduced the required elements, one proceeds to analyse a rotating system regarding its modal properties by computing the Campbell Diagram, which presents the evolution of the eigenfrequencies along the rotation frequency. In order to do so one starts with applying a null force vector on equation 2.34, with the coordinated transformation shown in 2.39 with a solution of the form described in the following equation:

$$\{q(t)\} = \{\hat{Q}\}e^{st} = \{\hat{Q}\}e^{(i\omega+\sigma_d)t} \tag{2.84}$$

where $q(t)$ is a vector containing the generalized coordinates, $\{\hat{Q}\}$ is the amplitude vector and $s = i\omega+\sigma_d$ represents the complex eigenvalues, with σ_d as the decay rate and ω the natural frequency, the resulting expression is obtained:

$$(s^2[M(\Omega)] + s[C(\Omega)] + [K(\Omega)])\{\hat{Q}\} = 0 \tag{2.85}$$

In order to obtain the eigenfrequencies ω and the decay rate σ_d, one uses a polynomial eigenvalue solver named $polyeig$ in $Matlab$ [29]. If the decay rate σ_d is positive, one has an unstable mode since the

amplitude will only increase in time, but if the only contribution to the damping matrix $[C]$ comes from the gyroscopic or Coriolis effect, then the decay becomes null considering that such forces are conservative and do not dissipate energy.

Finally, to compute the Campbell Diagram the eigenfrequencies ω are plotted in order to the rotation speed Ω. A critical speed is determined when the eigenfrequencies match with a spin speed, as introduced at section 2.4.4 and illustrated by Figure 2.16.

2.5.7 Harmonic Response

For an harmonic analysis, which is done in the frequency domain, the force vector $\{f(t)\}$ represents an harmonic excitation considering a fixed frequency ω common to all its components. In the time domain, this force excitation may be expressed using the following equation:

$$f_i = \hat{f}_i \cos(\omega t + \beta_i) \tag{2.86}$$

where β is the force's phase angle (in rad), which is considered to be null in this thesis. The previous equation is equivalent to a cosine $\{F_{rc}\}$ and sine $\{F_{rs}\}$ components, since one component is in phase with the rotation speed and the other with a $-\pi/2$ phase difference, respectively. Thus, the equation of motion may be written as follows:

$$[M(\Omega)]\{\ddot{q}(t)\} + [C(\Omega)]\{\dot{q}(t)\} + [K(\Omega)]\{q(t)\} = \{\{F_{rc}\}\cos\omega t + \{F_{rc}\}\sin\omega t\} \tag{2.87}$$

Subsequently, the system forced response adopts the same form, separated in cosine $\{Q_c\}$ and sine components $\{Q_s\}$, resulting in:

$$\{q(t)\} = \{Q_c\}\cos\omega t + \{Q_s\}\sin\omega t \tag{2.88}$$

To assess the system's response, the previous equation is written in the complex form, resulting:

$$q_i(t) = \hat{q}_i e^{i(\omega t + \phi_i)} = (\hat{q}_i \cos\phi_i + i\hat{q}_i \sin\phi_i)e^{i\omega t} = \hat{Q}_i e^{i\omega t} \tag{2.89}$$

Using the same procedure for the forcing functions, one obtains the following expression:

$$f_i = (\hat{f}_i \cos\beta_i + i\hat{f}_i \sin\beta_i)e^{i\omega t} = \hat{F}_i e^{i\omega t} \tag{2.90}$$

Substituting Equations 2.89 and 2.90 in the equation of motion 2.87, the system takes the simple form:

$$(-\omega^2[M(\Omega)] + [K(\Omega)] + i\omega[C(\Omega)])\{\hat{Q}_i\}e^{i\omega t} = \{\hat{F}_i\}e^{i\omega t} \tag{2.91}$$

Finally, to solve the previous equation the complex amplitudes of the response are computed as follows:

$$\hat{Q}_i = (-\omega^2[M(\Omega)] + [K(\Omega)] + i\omega[C(\Omega)])^{-1}\{\hat{F}_i\} \tag{2.92}$$

An important aspect to consider is that for a synchronous loading, such as the mass unbalanced case, the frequency of the applied load ω is the same as the rotational speed Ω.

The next step is to compute the deformation caused by the presence of unbalance. For this, a mass unbalanced may be placed in a rigid disk, resulting in a synchronous harmonic force with two components applied at the shaft's node to where the disk is located. This unbalanced is quantified by its mass m_u, distance d_u from the shaft geometric center and angular position α_u. Departing from the kinetic energy of the mass 2.68 and using the Euler-Lagrange equation, the forcing function can be obtained along two transversal coordinates:

$$\begin{Bmatrix} f_u \\ f_w \end{Bmatrix} = \Omega^2 \times m_u d_u \begin{Bmatrix} \sin(\Omega t + \alpha_u) \\ \cos(\Omega t + \alpha_u) \end{Bmatrix} = \Omega^2 \times m_u d_u \left(\begin{Bmatrix} \sin \Omega t \\ \cos \Omega t \end{Bmatrix} \cos \alpha_u + \begin{Bmatrix} \cos \Omega t \\ -\sin \Omega t \end{Bmatrix} \sin \alpha_u \right) \tag{2.93}$$

where f_u and f_w represent the resulting force along two transversal directions X and Z,respectively (also for the displacements u and w).

Extending the forcing functions to the complex plane, as in 2.90:

$$\begin{Bmatrix} f_u \\ f_w \end{Bmatrix} = \Omega^2 \times m_u d_u \begin{Bmatrix} \sin(\Omega t + \alpha_u) \\ \cos(\Omega t + \alpha_u) \end{Bmatrix} = \Omega^2 \times m_u d_u \left(\begin{Bmatrix} \sin \alpha_u \\ \cos \alpha_u \end{Bmatrix} - i \begin{Bmatrix} \cos \alpha_u \\ -\sin \alpha_u \end{Bmatrix} \right) e^{i\omega t} \tag{2.94}$$

In conclusion, a mass unbalance response analysis can be computed through a dynamic harmonic analysis to the structure as:

$$\begin{Bmatrix} F_u \\ F_w \end{Bmatrix} = \Omega^2 \times m_u d_u \left(\begin{Bmatrix} \sin \alpha_u \\ \cos \alpha_u \end{Bmatrix} + i \begin{Bmatrix} -\cos \alpha_u \\ \sin \alpha_u \end{Bmatrix} \right) \tag{2.95}$$

where F_u and F_w represent the frequency domain amplitude of f_u and f_w. Subsequently, the force harmonic response is computed through equation 2.92.

2.6 Rayleigh-Ritz Analytical Solution for a Mono-Rotor

In this section, the Rayleigh-Ritz method is employed to obtain the rotor dynamics phenomena such as the Campbell diagram, the natural frequencies of the system, the critical speeds on BW and FW and the effects of mass unbalance and harmonic force excitation. To do so the following mono-rotor model is introduced.

The rotor is composed by a flexible shaft of length L with a disk located at l_1 and a bearing at l_2 as illustrated by Figure 2.19. The model is assumed to be simply supported at both ends, thus, the displacement expressions in the X and Z directions (i.e. u and w, respectively) are given by:

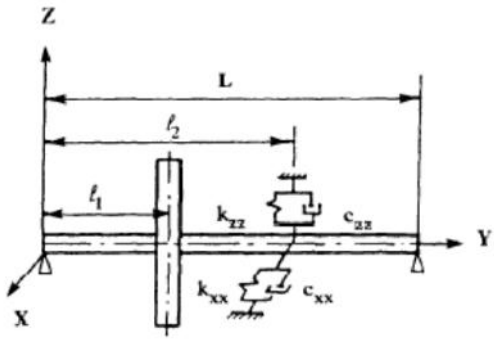

Figure 2.19: Lalanne and Ferraris theoretical model of the mono-rotor (source [3]).

$$u(y,t) = f(y)q_1(t) = f(y)q_1 \tag{2.96}$$

$$w(y,t) = f(y)q_2(t) = f(y)q_2 \tag{2.97}$$

where q_1 and q_2 represent the generalized independent coordinates, used to define the system's configuration relatively to the reference configuration, and the shape function $f(y)$, which is important to describe the rotor's lateral vibration behaviour. The implemented shape function, which is assumed to represent the first vibration mode of the simple supported rotor system, is given by:

$$f(y) = sin\left(\frac{\pi y}{L}\right) \tag{2.98}$$

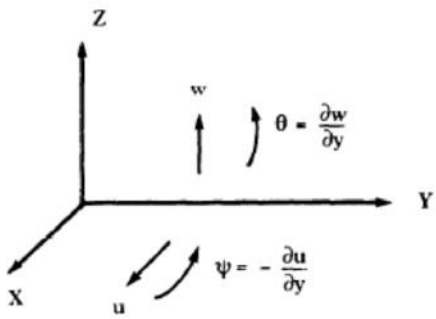

Figure 2.20: Inertial reference frame coordinates - source: [3]

Considering that the beam cross-section angular rotations θ and ψ are of small value (Figure 2.20), the following approximations are valid:

$$\theta = \frac{\partial w}{\partial y} = \frac{df(y)}{dy}q_2 = g(y)q_2 \tag{2.99}$$

$$\psi = \frac{\partial w}{\partial y} = \frac{df(y)}{dy}q_2 = g(y)q_2 \tag{2.100}$$

with: $g(y) = \frac{\pi}{L}\cos\frac{\pi y}{L}$.

The second-order derivatives of u and w used to compute the strain energy are given by:

$$\frac{\partial^2 u}{\partial y^2} = \frac{d^2 f(y)}{dy^2} q_1 = h(y) q_1 \tag{2.101}$$

$$\frac{\partial^2 w}{\partial y^2} = \frac{d^2 f(y)}{dy^2} q_2 = h(y) q_2 \tag{2.102}$$

with: $h(y) = -\left(\frac{\pi}{L}\right)^2 \sin \frac{\pi y}{L}$.

Applying the above Equations (2.96 to 2.102) in combination with the corresponding kinetic energy for both the disk and the shaft (2.59 and 2.60), it results:

$$T = \frac{1}{2} m(\dot{q}_1^2 + \dot{q}_2^2) - \Omega a \dot{q}_1 q_2 \tag{2.103}$$

where m stands for the system's mass and a represents the gyroscopic effect. Computing these two parameters, one has:

$$m = M_D f^2(l_1) + l_{Dx} g^2(l_1) + \rho S \int_0^L f^2(y) dy + \rho I \int_0^L g^2(y) dy \tag{2.104}$$

$$a = I_{Dy} g^2(l_1) + 2\rho I \int_0^L g^2(y) dy \tag{2.105}$$

Combining Equations 2.96 through 2.102 with 2.61, one obtains the shaft's strain energy. It is important to highlight that for this thesis only the lateral dynamics resulting form bending moments will be considered, thus the strain energy may be estimated as

$$U_S = \frac{1}{2} k(q_1^2 + q_2^2) \tag{2.106}$$

with the system stiffness k computed as:

$$k = EI \int_0^L h^2(y) dy \tag{2.107}$$

The expression to represent the virtual work done by the bearing on the shaft is given by Equations 2.62 and 2.63. Considering a bearing located at $Y = l_2$, the virtual work δW becomes:

$$\begin{aligned} \delta W = &-k_{xx} u(l_2)\delta u(l_2) - k_{xz} w(l_2)\delta u(l_2) - k_{zz} w(l_2)\delta w(l_2) - k_{zx} u(l_2)\delta w(l_2) \\ &- c_{xx}\dot{u}(l_2)\delta u(l_2) - c_{xz}\dot{w}(l_2)\delta u(l_2) - c_{zz}\dot{w}(l_2)\delta w(l_2) - c_{zx}\dot{u}(l_2)\delta w(l_2) \end{aligned} \tag{2.108}$$

Substituting 2.96 and 2.97 in Equation 2.108, it results:

$$\begin{aligned} \delta W = &-k_{xx}(f(l_2)^2 q_1 \delta q_1) - k_{xz}(f(l_2)^2 q_2 \delta q_1) - k_{zz}(f(l_2)^2 q_2 \delta q_2) - k_{zx}(f(l_2)^2 q_1 \delta q_2) \\ &- c_{xx}(f(l_2)^2 \dot{q}_1 \delta q_1) - c_{xz}(f(l_2)^2 \dot{q}_2 \delta q_1) - c_{zz}(f(l_2)^2 \dot{q}_2 \delta q_2) - c_{zx}(f(l_2)^2 \dot{q}_1 \delta q_2) \end{aligned} \tag{2.109}$$

simplifying,

$$\delta W = Fq_1\delta q_1 + Fq_2\delta q_2 \tag{2.110}$$

The components of the generalized force acting on the bearing located at $Y = l_2$ come from Equations 2.109 and 2.110, which were first introduced in 2.64.

$$\begin{bmatrix} F^B_{q_1} \\ F^B_{q_2} \end{bmatrix} = -f(l_2)^2 \begin{bmatrix} k_{xx} & k_{xz} \\ k_{zx} & k_{zz} \end{bmatrix} \begin{bmatrix} q_1 \\ q_2 \end{bmatrix} - f(l_2)^2 \begin{bmatrix} c_{xx} & c_{xz} \\ c_{zx} & c_{zz} \end{bmatrix} \begin{bmatrix} \dot{q}_1 \\ \dot{q}_2 \end{bmatrix} \tag{2.111}$$

Lastly, the kinetic energy due to the presence of an unbalanced mass in the disk located at a distance d from the axis of rotation according to 2.68 is given by

$$T_u \cong m_u \Omega d f(l_1)(\dot{q}_1 \cos\Omega t - \dot{q}_2 \sin\Omega t) \tag{2.112}$$

Using the two first terms of the Lagrange equation 2.49 with 2.112, it results:

$$\frac{d}{dt}\left(\frac{\partial T}{\partial \dot{q}}\right) - \frac{\partial T}{\partial q} = -m_u d f(l_1)\Omega^2 \begin{bmatrix} \sin(\Omega t) \\ \cos(\Omega t) \end{bmatrix}, \delta = [u, w]^T \tag{2.113}$$

With a mass unbalanced at an angular position α_u with respect to the Z axis, the forces become:

$$\begin{bmatrix} F^{m_u}_{q_1} \\ F^{m_u}_{q_2} \end{bmatrix} = m_u d f(l_1)\Omega^2 \begin{bmatrix} \sin(\Omega t + \alpha_u) \\ \cos(\Omega t + \alpha_u) \end{bmatrix} \tag{2.114}$$

In order to solve the rotor equation, one applies the kinetic energy, strain energy and virtual work equations of the rotor components in Lagrange Equation 2.49, obtaining the following equation of motion.

$$\begin{bmatrix} m & 0 \\ 0 & m \end{bmatrix} \begin{bmatrix} \ddot{q}_1 \\ \ddot{q}_2 \end{bmatrix} + \Omega \begin{bmatrix} 0 & -a \\ a & 0 \end{bmatrix} \begin{bmatrix} \dot{q}_1 \\ \dot{q}_2 \end{bmatrix} + \begin{bmatrix} k & 0 \\ 0 & k \end{bmatrix} \begin{bmatrix} q_1 \\ q_2 \end{bmatrix} = \begin{bmatrix} F_{q_1} \\ F_{q_2} \end{bmatrix} \tag{2.115}$$

where m is given by 2.104, a by 2.105 and k by 2.107. Considering a general rotor with viscously damped bearings, adding the bearing effect in Equation 2.115, results:

$$\underbrace{\begin{bmatrix} m & 0 \\ 0 & m \end{bmatrix}}_{M} \begin{bmatrix} \ddot{q}_1 \\ \ddot{q}_2 \end{bmatrix} + \underbrace{\left(f(l_2)^2 \begin{bmatrix} c_{xx} & c_{xz} \\ c_{zx} & c_{zz} \end{bmatrix} + \Omega \begin{bmatrix} 0 & -a \\ a & 0 \end{bmatrix} \right)}_{C} \begin{bmatrix} \dot{q}_1 \\ \dot{q}_2 \end{bmatrix} + \underbrace{\left(f(l_2)^2 \begin{bmatrix} k_{xx} & k_{xz} \\ k_{zx} & k_{zz} \end{bmatrix} + \begin{bmatrix} k & 0 \\ 0 & k \end{bmatrix} \right)}_{K} \begin{bmatrix} q_1 \\ q_2 \end{bmatrix} = \begin{bmatrix} F_{q_1} \\ F_{q_2} \end{bmatrix} \tag{2.116}$$

In the above equation, the first matrix represents the mass matrix, the second matrix contains the bearing's damping coefficients and the terms associated with Ω giving the gyroscopic effect matrix and the third matrix is associated with the bearing's stiffness coefficients and bending stiffness. An important aspect of these equations is that the eigenfrequencies are dependent of rotating speeds Ω due to the gyroscopic effects, thus it is necessary to represent the angular frequencies as a function of the speed of rotation and this may be accomplished by plotting the Campbell Diagram of the system.

In order to do so, it is necessary to conduct a free vibration analysis where no external forces are acting on the system. Considering an undamped system ($c_{xx} = c_{xz} = c_{zx} = c_{zz} = 0$) with $k_{xx} \neq 0$, $k_{zz} \neq 0$ and $k_{xz} = k_{zx} = 0$ (since the model only considers bearing stiffness values in the horizontal and vertical directions), the equation of free undamped motion becomes:

$$\begin{bmatrix} m & 0 \\ 0 & m \end{bmatrix} \begin{bmatrix} \ddot{q}_1 \\ \ddot{q}_2 \end{bmatrix} + \Omega \begin{bmatrix} 0 & -a \\ a & 0 \end{bmatrix} \begin{bmatrix} \dot{q}_1 \\ \dot{q}_2 \end{bmatrix} + \begin{bmatrix} k_{11} & 0 \\ 0 & k_{22} \end{bmatrix} \begin{bmatrix} q_1 \\ q_2 \end{bmatrix} = 0 \tag{2.117}$$

where $k_{11} = k + f(l_2)^2 k_{xx}$ and $k_{22} = k + f(l_2)^2 kzz$ represent the sum of the system stiffness with the bearing stiffness. A typical solution of Equation 2.117 can be expressed

$$q_1 = Q_1 e^{rt}, \tag{2.118}$$

$$q_2 = Q_2 e^{rt}, \tag{2.119}$$

with $r = -\frac{\alpha\omega}{\sqrt{1-\alpha^2}} \pm j\omega$.

$Q_{1,2}$ represent the amplitude of the vibrations in the generalized coordinates $q_{1,2}$, ω stands for the angular frequency and α is the modal damping related with each vibration mode. In this case (undamped rotors) α is null.

Substituting the two previous equations in 2.117, it gives the following eigenvalue problem:

$$\begin{bmatrix} k_{11} + mr^2 & -a\Omega r \\ a\Omega r & k_{22} + mr^2 \end{bmatrix} \begin{bmatrix} Q_1 \\ Q_2 \end{bmatrix} = 0 \tag{2.120}$$

Since one is interested in the non-trivial solution of 2.120, the coefficients Q_1 and Q_2 are selected so that the determinant is zero, i.e.

$$m^2 r^4 + ((k_{11} + k_{22})m + a^2\Omega^2)r^2 + k_{11}k_{22} = 0 \tag{2.121}$$

To determine the angular frequencies at rest ($\Omega = 0$), one needs to solve the previous equation in order to r^2, resulting on

$$r_{10}^2 = j^2\omega_{10}^2 = -\frac{k_{11}}{m} \Rightarrow \omega_{10} = \sqrt{\frac{k_{11}}{m}} \tag{2.122}$$

$$r_{20}^2 = j^2\omega_{20}^2 = -\frac{k_{22}}{m} \Rightarrow \omega_{20} = \sqrt{\frac{k_{22}}{m}} \tag{2.123}$$

For a rotating system ($\Omega \neq 0$), the first and second roots (r_1 and r_2) and their respective angular frequencies (ω_1 and ω_2) become [3]

$$r_1^2 = -\left[\frac{\omega_{10}^2}{2} + \frac{\omega_{20}^2}{2} + \frac{a^2\Omega^2}{2m^2} - \sqrt{\left(\frac{\omega_{10}^2}{2} + \frac{\omega_{20}^2}{2} + \frac{a^2\Omega^2}{2m^2}\right)^2 - \omega_{10}^2\omega_{20}^2}\right], r_1 = \mp j\omega_1 \tag{2.124}$$

$$\omega_1 = \sqrt{\frac{\omega_{10}^2}{2} + \frac{\omega_{20}^2}{2} + \frac{a^2\Omega^2}{2m^2} - \sqrt{\left(\frac{\omega_{10}^2}{2} + \frac{\omega_{20}^2}{2} + \frac{a^2\Omega^2}{2m^2}\right)^2 - \omega_{10}^2\omega_{20}^2}} \tag{2.125}$$

$$r_1^2 = -\left[\frac{\omega_{10}^2}{2} + \frac{\omega_{20}^2}{2} + \frac{a^2\Omega^2}{2m^2} + \sqrt{\left(\frac{\omega_{10}^2}{2} + \frac{\omega_{20}^2}{2} + \frac{a^2\Omega^2}{2m^2}\right)^2 - \omega_{10}^2\omega_{20}^2}\right], r_2 = \mp j\omega_2 \tag{2.126}$$

$$\omega_2 = \sqrt{\frac{\omega_{10}^2}{2} + \frac{\omega_{20}^2}{2} + \frac{a^2\Omega^2}{2m^2} + \sqrt{\left(\frac{\omega_{10}^2}{2} + \frac{\omega_{20}^2}{2} + \frac{a^2\Omega^2}{2m^2}\right)^2 - \omega_{10}^2\omega_{20}^2}} \tag{2.127}$$

Observing Equations 2.125 and 2.127, it is certain that the natural frequencies are dependent of the angular velocity, leading to the plot of the Campbell Diagram (Figure 2.15). Also, from Equations 2.124 and 2.126, one notices that r_1 and r_2 are imaginary quantities, thus the rotor is said to be stable if the real part (decay rate) of the imaginary roots is negative. The decay rate becomes null if the only contribution to the global damping matrix $[C]$ comes from the gyroscopic or Coriolis effect, since these forces are conservative and don't dissipate energy.

Having completed the necessary tools to plot the Campbell Diagram, one may now determine the system's mode shapes and sense of whirl during an harmonic movement. The first step consists on solving the system of equations 2.120 in order to Q_1 and Q_2:

$$Q_1 = \frac{(a\Omega)}{(k_{11} + mr^2)} r Q_2 \tag{2.128}$$

$$Q_2 = -\frac{(a\Omega)}{(k_{22} + mr^2)} r Q_1 \tag{2.129}$$

Referring to the mode shapes that correspond to $r = r_1 = \pm j\omega_1$ and using 2.128:

$$\begin{cases} Q_1(j\omega_1) = jQ_2(j\omega_1), \quad if \quad r_1 = +j\omega_1 \\ Q_1(-j\omega_1) = -jQ_2(-j\omega_1), \quad if \quad r_1 = -j\omega_1 \end{cases} \tag{2.130}$$

Performing the same, but for $r = r_2 = \pm j\omega_2$:

$$\begin{cases} Q_1(j\omega_2) = -jQ_2(j\omega_2), \quad if \quad r_2 = +j\omega_2 \\ Q_1(-j\omega_2) = jQ_2(-j\omega_2), \quad if \quad r_2 = -j\omega_2 \end{cases} \tag{2.131}$$

Solving Equations 2.130 and 2.131 in order to Q_2:

$$\begin{cases} Q_2(j\omega_1) = j^{-1}Q_1(j\omega_1), \quad if \quad r_1 = +j\omega_1 \\ Q_2(-j\omega_1) = (-j)^{-1}Q_1(-j\omega_1), \quad if \quad r_1 = -j\omega_1 \\ Q_2(j\omega_2) = (-j)^{-1}Q_1(j\omega_2), \quad if \quad r_2 = +j\omega_2 \\ Q_2(-j\omega_2) = j^{-1}Q_1(-j\omega_2), \quad if \quad r_2 = -j\omega_2 \end{cases} \tag{2.132}$$

One is now capable of characterizing the free motion (vibration) of the system, applying the following

general expressions:

$$q_1 = Q_1 e^{rt} = jA_1 e^{j\omega_1 t} - jB_1 e^{j\omega_1 t} - jA_2 e^{j\omega_2 t} + jB_2 e^{-j\omega_2 t} \tag{2.133}$$

$$q_2 = Q_2 e^{rt} = A_1 e^{j\omega_1 t} + B_1 e^{-j\omega_1 t} + A_2 e^{j\omega_2 t} + B_2 e^{-j\omega_2 t} \tag{2.134}$$

where A_1,A_2,B_1 and B_2 are constants derived from specific initial conditions. In this case, one may consider a set of initial conditions for the first natural frequency ω_1 and $t = 0$:

$$\begin{cases} q_1 = 0 \\ q_2 = q_{20} \\ \dot{q_1} = -\omega_1 q_{20} \\ \dot{q_2} = 0 \end{cases} \tag{2.135}$$

Introducing the previous initial conditions in 2.133 and 2.134, one gets:

$$\begin{cases} A_2 = B_2 = 0 \\ A_1 = B_1 = \frac{q_{20}}{2} \end{cases} \tag{2.136}$$

Applying the above constants in Equations 2.133 and 2.134 one may compute, after some algebraic manipulation, the final expressions for q_1 and q_2:

$$\begin{cases} q_1 = -q_{20} \sin(\omega_1 t) \\ q_2 = q_{20} \cos(\omega_1 t) \end{cases} \tag{2.137}$$

The displacements for some point located at $Y = l$ consist of a beam shape function combined with q_1 and q_2, resulting:

$$\begin{cases} u(l,t) = -q_{20} \sin\left(\frac{\pi l}{L}\right) \sin(\omega_1 t) = -R \sin(\omega_1 t) \\ w(l,t) = q_{20} \sin\left(\frac{\pi l}{L}\right) \cos(\omega_1 t) = R \cos(\omega_1 t) \end{cases} \tag{2.138}$$

where,

$$R = \sqrt{u^2(l,t) + w^2(l,t)} = q_{20} \sin \frac{\pi l}{L} \tag{2.139}$$

With these conditions, one may now plot the rotor's orbit, as illustrated in Figure 2.21.

Examining Figure 2.21, one notices that the orbit is described in the opposite direction of the sense of rotation, implicating that the first natural frequency ω_1 translates a situation of BW.

Following the same procedure, but with a new set of initial conditions, considering the second natural frequency ω_2 and $t = 0$, one gets:

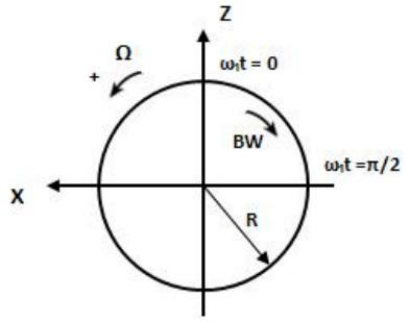

Figure 2.21: Backward Whirl orbit (source [3]).

$$\begin{cases} q_1 = q_{10} \\ q_2 = 0 \\ \dot{q_1} = 0 \\ \dot{q_2} = -\omega_2 q_{10} \end{cases} \tag{2.140}$$

Substituting the previous expressions in Equations 2.133 and 2.134, results:

$$\begin{cases} q_1 = q_{10}\cos(\omega_2 t) \\ q_2 = -q_{10}\sin(\omega_2 t) \end{cases} \tag{2.141}$$

Leading to the displacements u and w related to a point in $Y = l$:

$$\begin{cases} u(l,t) = q_{10}\sin\left(\frac{\pi l}{L}\right)\cos(\omega_2 t) = R\cos(\omega_2 t) \\ w(l,t) = -q_{10}\sin\left(\frac{\pi l}{L}\right)\sin(\omega_2 t) = -R\sin(\omega_2 t) \end{cases} \tag{2.142}$$

This time, the described orbit is in the same sense as that of the rotation Ω, simulating a FW condition as shown in Figure 2.22.

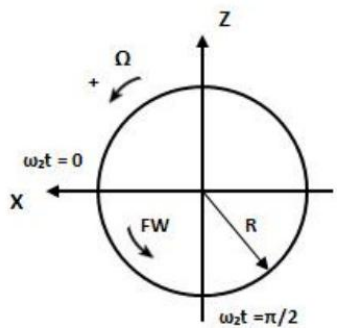

Figure 2.22: Forward Whirl orbit (source [3]).

2.7 Modal Tests

In most cases, it is challenging to model theoretically the real dynamics of rotating machinery in operation. Thus, numerical calculations are often based on the simplified model, which features the various structural components of the system. In order to validate the computed results from the numerical analysis (e.g., natural frequencies, mode shapes, damping factors, critical speeds), resonance tests are carried out on a prototype machinery to assure that resonance conditions are avoided. Throughout this section, one introduces the different types of modal tests and the general equipment used in these procedures.

There are various methods to accomplish resonance tests on machines, parts or individual components. These are classified according to the type of excitation force acting on the system [30]:

- Bump or impact hammer test,
- Shaker test,
- Transient test.

Figure 2.23 represents a schematic of an impact hammer test and a shaker test using a SISO (Single Input - Single Output) configuration, i.e., system composed by one entry and one exit.

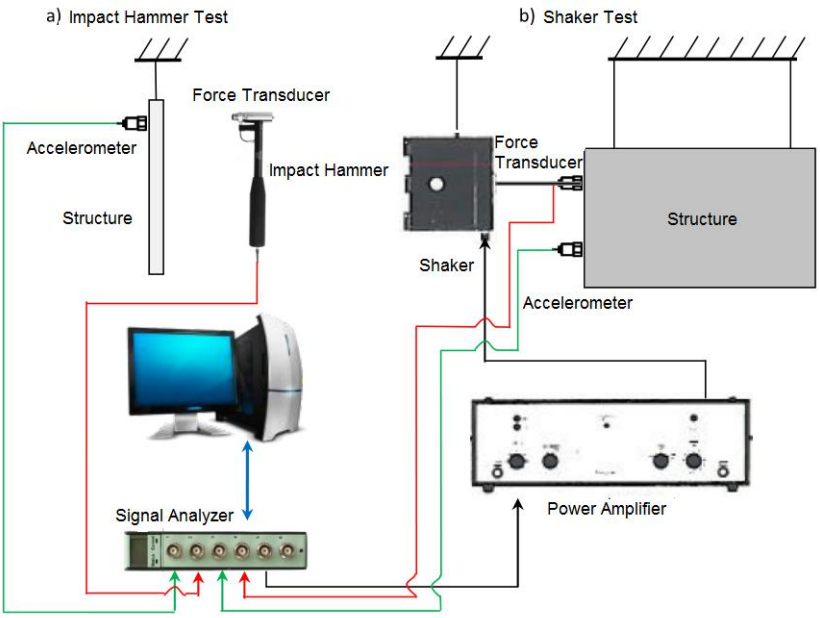

Figure 2.23: Modal test, SISO configuration (source [31]).

One of the main objectives of these tests is to determine the FRFs and identify the natural frequencies of the system. To accomplish this, the experiments are conducted using the following tools:

- Excitation equipment;
- Measurement equipment;
- Data acquisition system.

Next, one introduces some aspects regarding the structure support for the experimental test and the preparations to consider relatively to the three categories of equipment previously mentioned.

2.7.1 Structure Support

The first step to prepare a structure for a modal test is to dictate a boundary condition at which the system is subjected. The fixing mechanism should be well defined to assure the reliability of the acquired data and it should also reflect the dynamic behaviour of the structure without excessive influence the experiment results.

Usually, boundary conditions are specified in a completely free or completely constrained sense, however these conditions are hard to achieve in a lab environment [26]. Free conditions require the body to be floating in space with no attachments to the ground or ceiling, which are circumstances where it also displays a rigid body behaviour at zero frequency - e.g., an airplane in motion. For a sufficiently constrained structure, the rigid body's motion (displacement/rotations) is null.

A common procedure to simulate a completely free boundary condition, is to suspend the structure using very soft elastic strings in order to constrain the body and approximate the rigid body frequencies to zero, as illustrated in Figure 2.24.

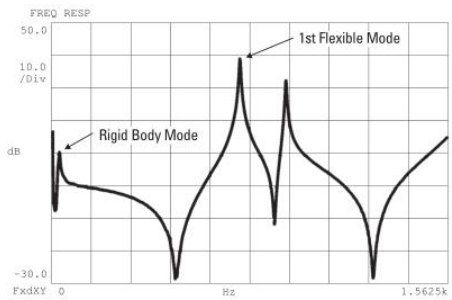

Figure 2.24: Frequency response of a freely suspended system (source [26]).

In the case of a completely constrained system, one possible way to simulate and validate this condition is to measure the frequency response of the base at the attachment points. Then, one compares this frequency with the response of the structure's remaining components, if the frequency response of the attachment points is significantly lower, it will have a negligible effect on the test results.

It is important to choose the right boundary conditions in order to have good correlation between the physical structure and the finite element model. In the end, there is not a best approach for supporting a test structure for modal analysis, it depends on the situation at hand and the goals that one wishes to achieve.

2.7.2 Excitation Equipment

To preform a modal test it is necessary to choose an excitation function and the mechanism in charge off applying the excitation force to the structure.

The force produced may be an impulse in the case of the hammer (impact hammer test), or by coupling to the structure for the electromagnetic shaker (shaker test), producing different types of signals in the required frequency range. Regarding the transient test, the rotating machine excites itself, as the dynamic forces (rotational motion) come into play when the machine starts up and accelerates to a maximum speed and coasts down to rest with constant deceleration [30].

In the bump or hammer test, one uses an impact hammer with a load cell attached to its head, Figure 2.25. This procedure is normally conducted on stationary components in order to reveal their natural frequencies. Since this equipment doesn't require a signal generator nor an amplifier, the energy applied to the structure comes form the linear momentum, thus it depends on the hammer's mass and velocity of impact. For this reason the operator's experience with the equipment is crucial in order to obtain reasonable results.

Figure 2.25: Impact hammer with load cell and different hardness tips (source [25]).

The signal's frequency range depends on the hammer's mass and the stiffness of the hammer tip, thus different hammer tips are used depending on the desired frequency range, Figure 2.26 a). For low frequency measurements, a soft rubber tip concentrates the excitation energy in a narrow frequency range, while a hard metal tip provides a higher amount of energy making it suitable for measurements at high frequencies. The tip must be selected so that all modes of interest are excited by the impact force over the chosen frequency range.

Another important aspect of impact testing is the use of force windows for the impact signal and exponential windows for the response transducer. The force windows are responsible for attenuating noise from the impulse signal, Figure 2.26 b). If the data that follows the impulse signal in the sample window is non-zero, the force window preserves the samples in the proximity of the signal and removes the noise from all other samples in the force signal by making them zero.

On the other hand, if the response signal doesn't decay to zero within the time window, an exponential window is applied to minimize the leakage effect in the response spectrum, i.e. to prevent the distortion of the signal when transformed to the frequency domain. This is accomplished by forcing the impulse response to be fully contained within the sampling window satisfying the periodicity requirements of the Fourier transform process, as shown in Figure 2.27.

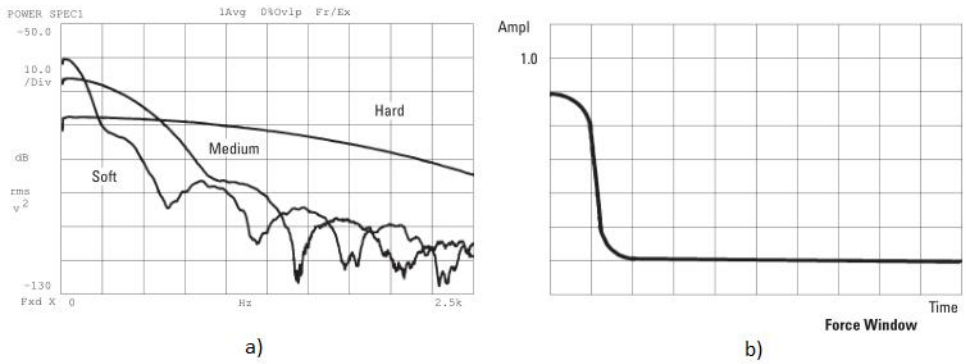

Figure 2.26: Impact force applied by the hammer: a) According to the tip's hardness; b) Force window (source [26]).

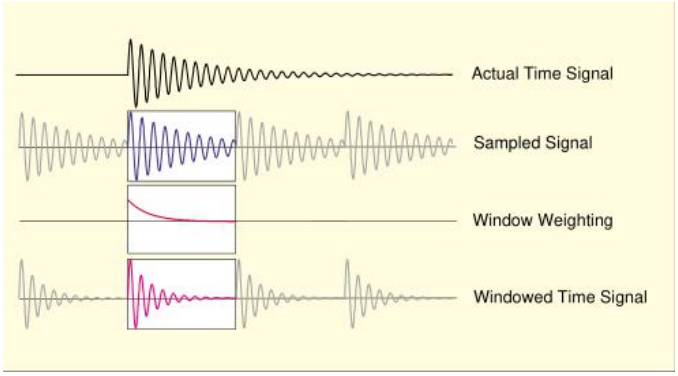

Figure 2.27: Exponential window to minimize leakage effects (source [32]).

In some cases it is not convenient to use the impact hammer test, either because the structure has fragile surfaces or due to the components limited frequency range over the spectrum making it too difficult to excite the modes of interest. Under these circumstances, the FRF measurement is usually conducted with one or multiple shakers. The electromagnetic shaker is usually attached to the structure using a stinger (flexible drive rod) so that the impact force is measured in the direction of the rod's axis. The excitation force is then measured by a force transducer placed between the stinger and the structure, as illustrated in Figure 2.28.

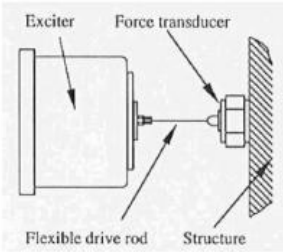

Figure 2.28: Connection of the shaker to the structure (source [15]).

In order to complete the excitation mechanism for the shaker test, it is necessary to use a signal generator to create an excitation function, whose amplitude is usually regulated by the power amplifier, see Figure 2.23. There are many types of excitation signals conceived to generate shaker measurements

with FFT analyzers. Although this wont be a topic of discussion in this thesis, these signals include: *transient*, *true random*, *pseudo random*, *burst random*, *fast sine sweep (chirp)* and *burst chirp* [16].

2.7.3 Measurement Equipment

The measurement equipment is generally formed by transducers used to measure the excitation force and the response of the system. These can be classified according to the requested parameter. The displacements are measured by a potenciometer, the velocity may be obtained using *lasers* (based on the Doppler effect) and the acceleration is usually acquired with piezoelectric accelerometers.

The measurements preformed during this work where made using piezoelectric accelerometers (Figure 2.29), which are known to have a wide frequency range, good linearity and relatively good durability. These sensors convert the acceleration signal to an electronic voltage signal that can be measured, analyzed and recorded. In other words, the accelerometer moves in coordination with the surface of the structure, applying a force in the piezoelectric element causing its deformation. This effect creates a electrical charge proportional to the acceleration of the structure [15].

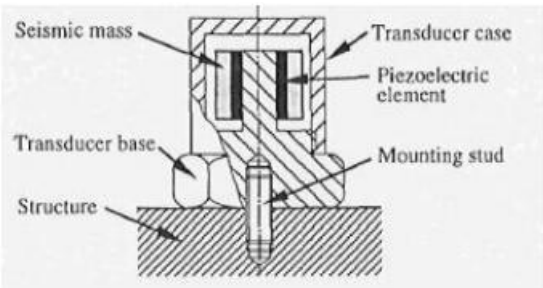

Figure 2.29: Cross-section view of a piezoelectric accelerometer (source [15]).

There are some operating characteristics to consider in order to choose the right measurement equipment for a modal test. These include the transducer's sensitivity, resonant frequency, size and mass.

Since the signal analyser has a predetermined range of voltage, it is important to choose the correct value of sensitivity for the accelerometer, measured in mV/N. A too high value of sensitivity may saturate the input circuitry on the signal analyser, while an extremely small sensitivity value could produce a signal too weak to accurately measure the structure's acceleration. It is also important to assure that the frequency range of the test falls within the frequency response of the transducer, i.e. one should not operate close to the resonance frequency of the transducer since the accelerometer looses its linearity and sensitivity near these conditions, Figure 2.30. Finally the effect of size and mass loading from the accelerometer may bring a significant influence on the dynamic behaviour specially on small structures, since the frequency response measured may not be completely accurate [26].

All things considered, the ideal accelerometer would have high sensitivity, a wide frequency range and small mass in order to have the least influence on the dynamic behaviour of the structure. Trade-offs are usually made since high sensitivity usually requires larger transducers, so a balance between the properties of the accelerometer should be made to meet the requirements of the test.

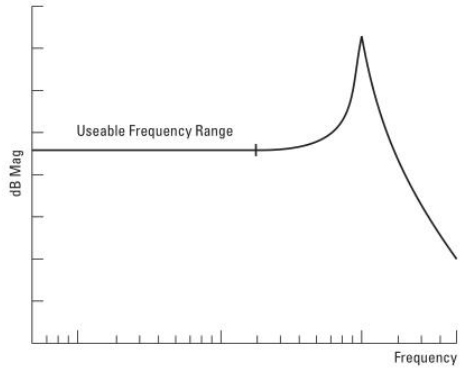

Figure 2.30: Frequency response of the accelerometer (source [26]).

The mounting procedure for contact-type transducers may have a significant influence on the frequency response of a modal test. First off all, the transducer should be mounted on a clean, flat, smooth and unscratched surface over the frequency range of interest to avoid distortion of the results, Figure 2.31 shows three common reasons for coupling mistakes.

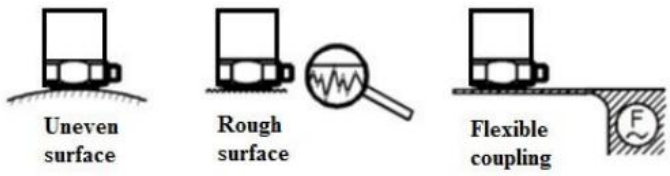

Figure 2.31: Typical reasons of coupling errors (source [33]).

Second, the mounting method (Figure 2.34) should be chosen carefully since the natural frequency of the accelerometer is dependent on the stiffness of the coupling method [33]. The accuracy of the acceleration measurement depends greatly on the mounting which may be modelled by a spring and a damper (Figure 2.32).

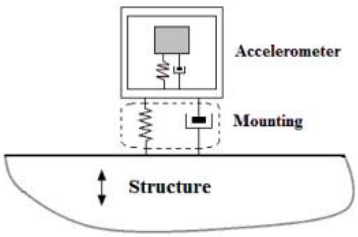

Figure 2.32: Schematic model of an accelerometer and its mounting (source [33]).

The best accuracy of the measurement would be possible if the mounting were rigid. A flexibility of the mounting indicates that the characteristics of the accelerometer may be compromised. Due to that flexibility, the acceleration of the structure may be different from the experienced by the accelerometer. The main mounting methods include:

- Hand held;
- Magnet;

- Cemented stud;
- Bee wax.

The stud mounting provides a very secure attachment for the accelerometer to the structure and assures perpendicularity, but it is not so practical since it promotes the deformation of the structure. The hand held and wax methods are more versatile, but in some cases can be harder to properly apply since the accelerometer needs to be perpendicular to the structure. The magnet is a safe and versatile method and doesn't damage the surface of the component, but it is exclusive to ferromagnetic materials. In the end, it is up to the operator to choose the best mounting method in order to achieve the best results.

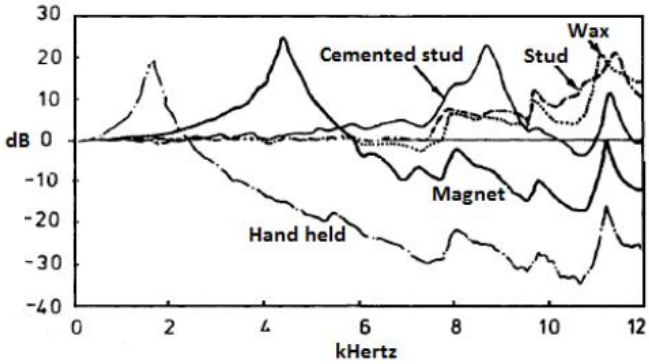

Figure 2.33: Frequency responses obtained with different mounting methods (source [33]).

2.7.4 Data Acquisition System and FRF Estimators

The data acquisition system is composed by the dynamic signal analyser (DSA) working in conjunction with a specific modal analysis software installed on a computer, such as the *Pulse Labshop* [17]. This equipment is in charge of receiving the transducer's analogue signal in the time domain and convert it to the frequency domain resorting to the *Fast Fourier transform* (FFT), the signal is then processed using an appropriate computer software in order to obtain the FFRs of the system.

As it was already mentioned, the signal is measured by a transducer located in the same position as the applied force. However, the excitation force applied to the structure may be different from the force measured by the transducer, normally due to electric noise present in the equipment, creating noise at the signal's entrance and therefore affecting the calculation of antiresonance frequencies. In a similar way, the response signal measured by the accelerometer may be different from the true response due to external factors, originating noise at the exit signal, affecting the calculation of resonance frequencies.

In order to minimize these effects, two FRF estimators (H_1 and H_2) are used to filter the entrance and exit of the signal, Figure 2.34 a) and b). The first estimator $H_1(\omega)$ is used to minimize the signal's exit noise and it is determined dividing the Cross Spectrum between the response and the force ($G_{FX}(\omega)$) by the Autospectrum of the force ($G_{FF}(\omega)$) [34].

$$H_1(\omega) = \frac{\sum F^* X}{\sum F^* F} = \frac{G_{FX}(\omega)}{G_{FF}(\omega)} \tag{2.143}$$

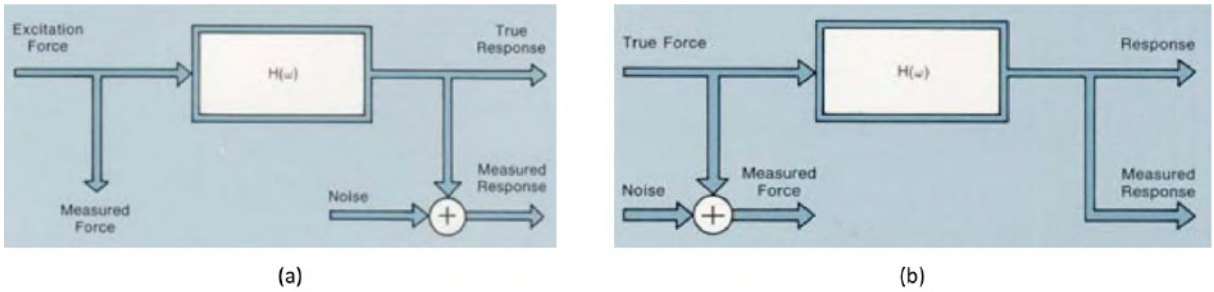

Figure 2.34: Estimators: a) H_1 ; b) H_2 (source [34]).

The second estimator $H_2(\omega)$ is used to reduce the signal's entrance noise and it is a result of the coefficient between the Autospectrum of the response ($G_{XX}(\omega)$) and the Cross Spectrum ($G_{FX}(\omega)$).

$$H_2(\omega) = \frac{\sum X^* X}{\sum X^* F} = \frac{G_{XX}(\omega)}{G_{XF}(\omega)} \tag{2.144}$$

In an ideal scenario, both estimators $H_1(\omega)$ and $H_2(\omega)$ should be equal, thus it is possible to define a function that indicates the quality of the experimental results through the coefficient between both estimators:

$$\frac{H_1(\omega)}{H_2(\omega)} = \frac{|G_{FX}(\omega)|^2}{G_{XX}(\omega)G_{FF}(\omega)} = \gamma^2(\omega) \tag{2.145}$$

where $\gamma^2(\omega)$ represents the Coherence function, which represents the correlation between the measured force and the response signal and can vary between the following values:

$$0 < \gamma^2(\omega) < 1 \tag{2.146}$$

Generally speaking, the presence of noise ($\gamma^2(\omega) < 1$) normally takes place due to damaged equipment, environment factors or other external conditions.

Besides the estimators, the use of a proper range of frequency in the FRFs is very important. The far end of the natural frequencies should be well within the frequency range in order to identify them and to determine the correct dampening.

Chapter 3

Methodology

3.1 Analytical Methodology

In this section, one presents how the analytical solution is implemented resorting to the equations deduced in section 2.4.1 in coherence with the Rayleigh-Ritz analytical method described in section 2.6. This solution will provide a comparison of the implemented solution (FEM) with some results found at the literature, more specifically in Lalanne and Ferraris [3].

In order to do so, one needs to determine the solution of the characteristic Equation 2.121, which leads to two pairs of complex conjugate roots, $r_1 = -\frac{\alpha_1\omega_1}{\sqrt{1-\alpha_1{}^2}} \pm j\omega_1$ and $r_2 = -\frac{\alpha_2\omega_2}{\sqrt{1-\alpha_2{}^2}} \pm j\omega_2$, where ω_1 and ω_2 are the first and the second natural frequencies and are dependent of the rotating speed of the shaft (Ω), and α_1 and α_2 represent the associated viscous damping factors (which are conisdered null in this work). Remind that one is interested in obtaining the rotor equations of motion in the form of 2.116. After obtaining the rotors mass $[M]$, damping $[C]$ and stiffness $[K]$, by computing the variables m (2.104), a (2.105) and k (2.107), the matrices are introduced in a polynomial eigenvalue solver (e.g. polyeig in $Matlab$ [29]), which is used to obtain the roots r_1 and r_2 and the respective eigenfrequencies ω_1 and ω_2.

These results yield to the equations that are used to obtain the Campbell diagram, more specifically 2.125 and 2.127. The Campbell diagram, exemplified in Figure 3.1, is a F versus Ω graphic that represents the variation of the natural frequencies of the rotor with increasing rotating speed, i.e. the frequency curves. Also, several lines may be traced from the graphic origin with different inclinations. These lines are normally defined by $F = nN/60$, where n is the inner-outer spool rotating speed ratio and N is the rotational speed in rotations per minute. There is a specific line traced on the Campbell Diagram called the synchronous line, i.e. the line that includes the point at which the natural frequency equals the rotating speed, and it is defined by $F = N/60$ $(n = 1)$. The intersection points of these lines with the frequency curves indicate the critical operation points, which are to be compared with the critical speeds obtained with the numerical and experimental models as it will be shown later.

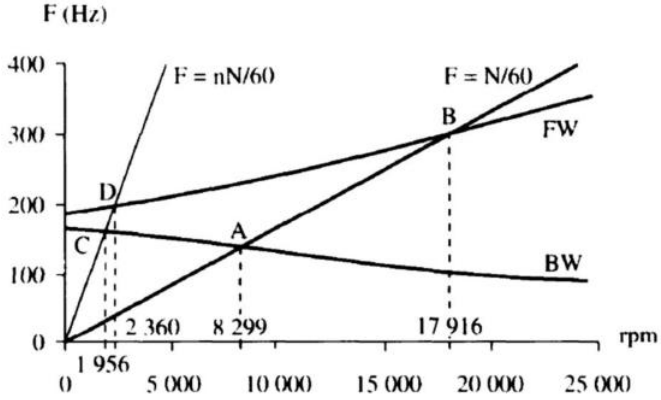

Figure 3.1: Campbell diagram example (source [3]).

To study the response to forces due to mass unbalances, one starts to describe the effect of a punctual mass m_u at a distance d from the center of the disk by rewriting the force vector 2.114 (considering an angular position $\alpha_u = 0$),

$$\begin{Bmatrix} F_{q_1}(t) \\ F_{q_2}(t) \end{Bmatrix} = \begin{Bmatrix} m_u d f(l_1)\Omega^2 \sin(\Omega t) \\ m_u d f(l_1)\Omega^2 \cos(\Omega t) \end{Bmatrix} \tag{3.1}$$

in which $f(l_1)$ is the value of the displacement function in the location l_1 of the disk (Figure 2.19).

Considering that the viscous damping effect is null ($[C] = 0$), the solution of the resultant equation comes in the following form

$$\begin{cases} q_1 = Q_1 \sin \Omega t \\ q_2 = Q_2 \cos \Omega t \end{cases} \tag{3.2}$$

Substituting Equations 3.1 and 3.2 in Equation 2.116, it results

$$\left[-\Omega^2 \begin{bmatrix} m & 0 \\ 0 & m \end{bmatrix} + \Omega \left(\Omega \begin{bmatrix} 0 & a \\ a & 0 \end{bmatrix} \right) + \begin{bmatrix} k_{11} & 0 \\ 0 & k_{22} \end{bmatrix} \right] \begin{Bmatrix} Q_1 \\ Q_2 \end{Bmatrix} = \begin{Bmatrix} m_u f(l_1)\Omega^2 d \\ m_u f(l_1)\Omega^2 d \end{Bmatrix} \tag{3.3}$$

Solving Equation 3.3 in terms of Q_1 and Q_2, it yields

$$\begin{cases} Q_1 = \frac{m_u f(l_1)\Omega^2 d(k_{22}-(m+a)\Omega^2)}{(k_1-m\Omega^2)(k_2-m\Omega^2)-a^2\Omega^4} \\ Q_2 = \frac{m_u f(l_1)\Omega^2 d(k_{11}-(m+a)\Omega^2)}{(k_1-m\Omega^2)(k_2-m\Omega^2)-a^2\Omega^4} \end{cases} \tag{3.4}$$

If viscous damping is added to the model, the solution become in the following form:

$$\begin{cases} q_1 = A_1 \sin \Omega t + B_1 \cos \Omega t \\ q_2 = A_2 \sin \Omega t + B_2 \cos \Omega t \end{cases} \tag{3.5}$$

Once again, using Equations 3.1 and 3.5 in Equation 2.116, the values of A_1, B_1, A_2 and B_2 are obtained by solving the resultant system.

Returning to the results from the system of Equations 3.4, one can now obtain the response diagram of the rotor system with the respective bearing conditions. This type of diagram is a plot of the logarithm of the sum of the transversal vibration amplitude ($Q_1 + Q_2$) against the rotating speed of the rotor's shaft, as exemplified in Figure 3.2. The graphic peaks represent the critical speeds of the rotor, which will be compared with the results obtained with the numerical and experimental models, as shown in the next chapter.

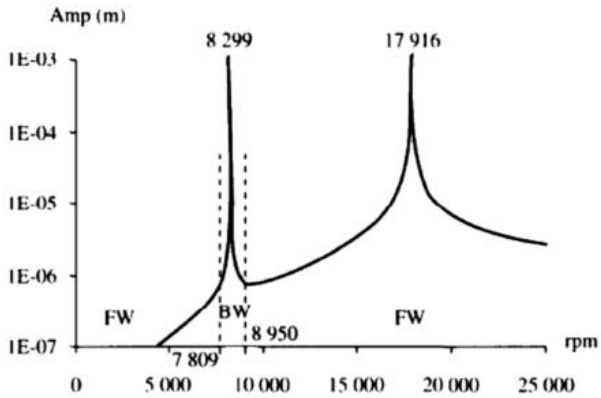

Figure 3.2: Response diagram example of amplitude (m) in function of spin speed Ω (rpm) (source [3]).

3.2 Numerical Methodology

In this section, one presents the procedures used for the numerical analysis. After establishing the finite elements used in the $Matlab$ code described in section 2.5, the $ANSYS$ elements are now introduced.

3.2.1 Main Steps in Finite Element Model Creation

The creation of a finite element model is normally divided in three steps: Pre-processing, Solution and Post-processing. The next subsections provide a description of these phases for the numerical model construction of a steel beam and for the mono-rotor, both in $ANSYS$ environment. For a more detailed description of this process one may consult [23].

Pre-processing

Generally speaking, the Pre-processing phase consists in defining the numerical model and includes the following steps:

1. Define the problem's geometry domain.

2. Appoint the finite element types to be used (beam, shell, solid, etc).

3. Designate the material properties (ρ, E, ν...).

4. Define the element geometric parameters (cross-section properties, length...).

5. Establish the element connectivities (mesh).

6. Specify the physical constrains of the model (boundary conditions: displacement constraints and applied loading).

Solution

The Solution phase corresponds to the choice of the solution type to implement. The commercial finite element code $ANSYS$ library offers a wide variety of solutions (static, modal, harmonic, transient, etc), being the modal and harmonic analysis the ones used in this work.

Each option establishes the differential equations assembled in matrix form and the computed unknown values, such as displacements, are obtained solving the corresponding system of equations. For a modal and an harmonic analysis (from Equation 2.19 and Equation 2.20, respectively), one intends to determine the associated output variables, which are the natural frequencies (ω), the modes (ϕ) and the damping factor ξ (if viscous damping is considered).

Post-processing

The Post-processing phase consists in processing other results than the displacements and graphic representation of the results. The modal analysis (generic postprocessing) shows the structure's natural frequencies and its deformation with respect to each vibration mode, while the harmonic analysis (time-history postprocessing) is able to plot displacement's amplitude $\frac{u_i}{u_0}$ versus ω.

3.2.2 Numerical Models

In this section, one presents the numerical models developed for a steel beam and for the rotor, in order to compare them with their respective experimental models. The purpose of developing a numerical model for a steel beam is to gain some experience in experimental modal analysis and to verify the proper functioning of the lab equipment by comparing its results with the data acquired with the experimental model described in section 3.3.2.

Steel Beam

The development of the steel beam numerical model follows the process described in section 3.2.1, where the Pre-processing parameters such as the material's description, the model's geometry, the mesh and the boundary conditions are presented.

In order to perform an harmonic analysis, one modelled the steel beam using the BEAM188 finite element [28] (Timoshenko beam theory), with cubic interpolation. The material is considered to be isotropic with linear elastic behaviour and the physical properties required to define it are the $Young's$ modulus $E(GPa)$, the $Poisson's$ coefficient ν and the density $\rho(kg/m^3)$, as shown in Figure 3.3.

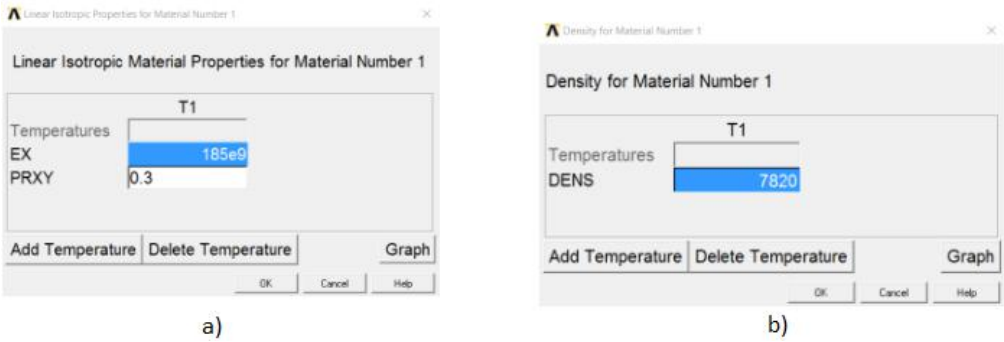

Figure 3.3: Beam model material properties in $ANSYS$: a) Young's Modulus and Poisson's ratio; b) Density.

Having established the material properties, one proceeds to define the geometric characteristics of the element along with the applied mesh.

Figure 3.4 a) illustrates the beam's rectangular cross-section, defined by its height $h(m)$ and width $w(m)$. The model was created using 2 keypoints linked by a line with length $l(m)$ and the respective mesh is applied using 50 finite elements per line. Since the beam experimental model is suspended by two nylon strings (elaborated in section 3.3.2), the model was computed using free-free boundary conditions at both ends and an unitary harmonic force $F = -1(N)$ is applied in the second keypoint in the Y direction, Figure 3.4 b), for the harmonic analysis.

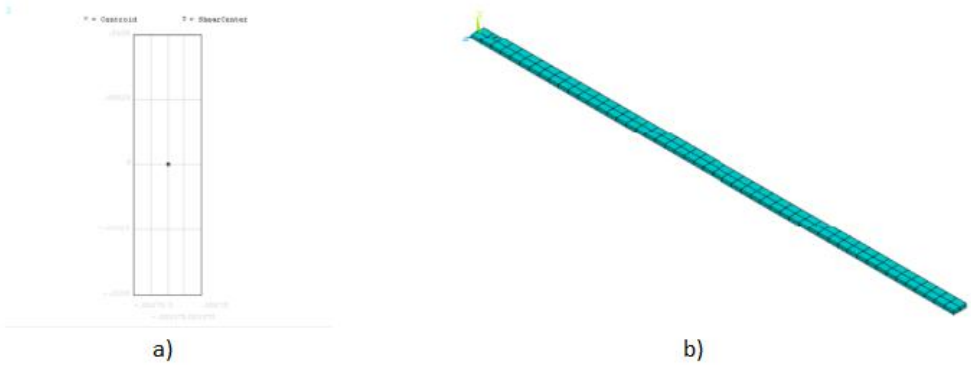

Figure 3.4: Beam model used in $ANSYS$: a) Rectangular cross-section; b) Finite element model.

Analysis: Modal/Harmonic

The structural analysis introduced in the end of section 2.2 are performed using the FEM. After the respective matrices assemblage, the analysis are expressed by the respective equations, which are rewritten.

The modal analysis (Equation 2.19)is used to obtain the eigenfrequencies and eigenmodes

$$K\{\psi\} - \omega_i^2 M\{\psi_i\}] = \{0\}, \tag{3.6}$$

and the harmonic analysis (Equation 2.20) is used to obtain the frequency response

$$[K\{\bar{U}\} - \omega_{ap}^2 M\{\bar{U}\}] = \{\bar{F}_{\omega_{ap}}\}. \tag{3.7}$$

In the previous equations, ω_i is the eigenfrequency, ψ_i is the eigenmode, ω_{ap} is the applied force excitation frequency, $\bar{U}$ is the respective maximum displacement and $\bar{F}_{\omega_{ap}}$ is the magnitude of the applied force. These results are then compared with the experimental analysis. All finite element analysis are programmed in APDL (ANSYS Parametric Design Language), a scripting language used to build models in terms of selected parameters and to automate common tasks.

Rotor

As mentioned in section 2.4 rotor systems are characterized by a set of basic components, the disk, the shaft, the bearings and a mass unbalanced. Just as the beam model, the rotor numerical model follows the procedure described in section 3.2.1, where the Pre-processing parameters are performed for the shaft, disk and bearings. It is important to mention that the cross-section of the rotor was modelled in the XZ plane and the length of the shaft is computed in the Y axis in order to simulate the theoretical model introduced in [3].

The $ANSYS$ element used to model the shaft was the BEAM188 (2 node/6 dofs). This finite element is based on the Timoshenko theory and it is the only beam element that is composed by 2 nodes and takes into consideration the Coriolis and gyroscopic effect in the damping matrix. To apply the gyroscopic effect to the rotating structure, one used the (CORIOLIS) command, which also applies the rotating damping effect. Additionally, the BEAM188 finite element is recommended to represent slender beams, which is the case for the shaft used in this work.

The shaft's material was defined with the generic properties of the aluminium, which include the $Young's$ modulus $E(GPa)$, the $Poisson's$ coefficient ν and the density $\rho(kg/m^3)$, as shown in Figure 3.5.

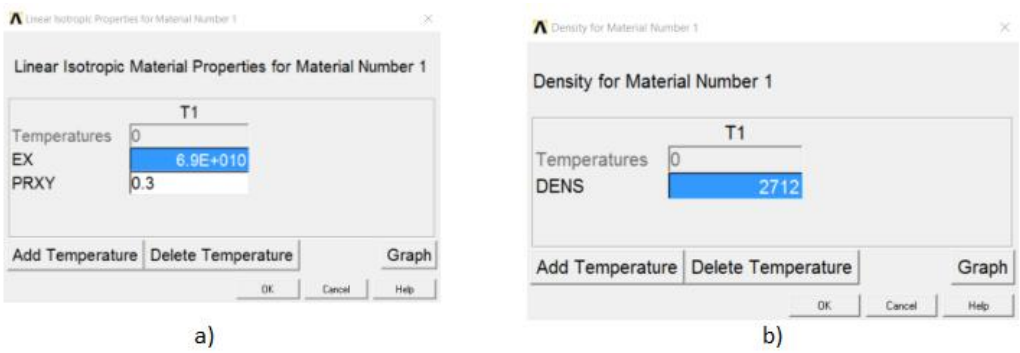

Figure 3.5: Shaft model material properties in $ANSYS$: a) Young's Modulus and Poisson's ratio; b) Density.

The shaft's cross-section is described by its radius $R(m)$ and disk quarter division N, as shown in Figure 3.6 a). The shaft model was computed using 2 keypoints connected by a line with length $L(m)$ (total shaft length). The respective mesh is applied dividing the line into N_e elements in the axial direction. Since the shaft is considered simply supported, fixed-fixed boundary conditions were implemented

in all directions (X, Y and Z axis) at keypoints 1 and 2, while fixed-fixed boundary conditions were applied on the remaining nodes of the shaft only in the axial direction (axis Y).

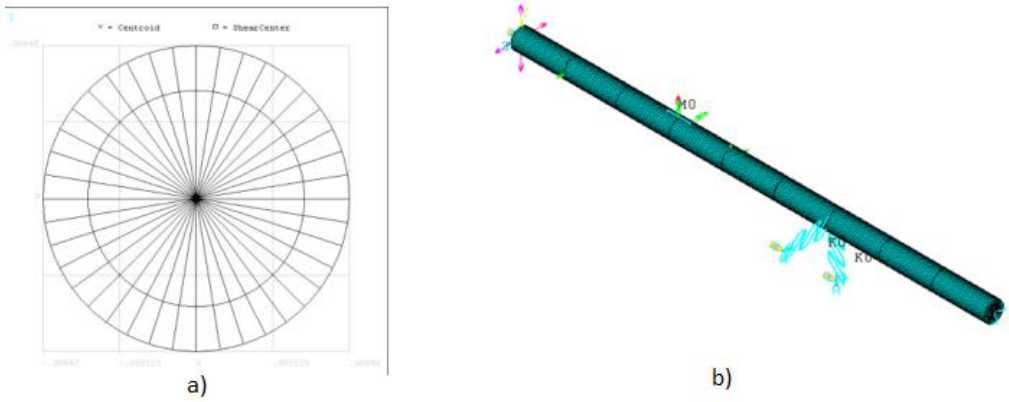

Figure 3.6: Rotor model used in $ANSYS$: a) Circular cross-section; b) Mono-rotor model, with disk of mass $M0$ and spring of elastic constant $K0$.

The rigid disk is represented by the MASS21 finite element [28] located at $l_1 = L/3(m)$, which has up to six dofs. As shown in Figure 3.7 a), the inputs required to model this element include the disk's mass $M_D(kg)$ and rotary inertia $I_{xx} = I_{zz}(kg.m^2)$ and $I_{yy}(kg.m^2)$.

In order to simulate an undamped asymmetric rotor, one implements two spring-damper elements, denominated COMBIN14 [28], located at $l_2 = 2L/3(m)$. Also, fixed-fixed boundary conditions on all directions (X, Y and Z axis) where applied on the 2 external keypoints of the spring-damper elements. Figure 3.7 b) demonstrates the inputs that characterize this component, which involve the stiffness and damping coefficients on X and Z directions, $K_{xx}(N/m)$, $K_{zz}(N/m)$ and $K_{xz} = K_{zx} = C_{xx} = C_{zz} = C_{xz} = C_{zx} = 0$.

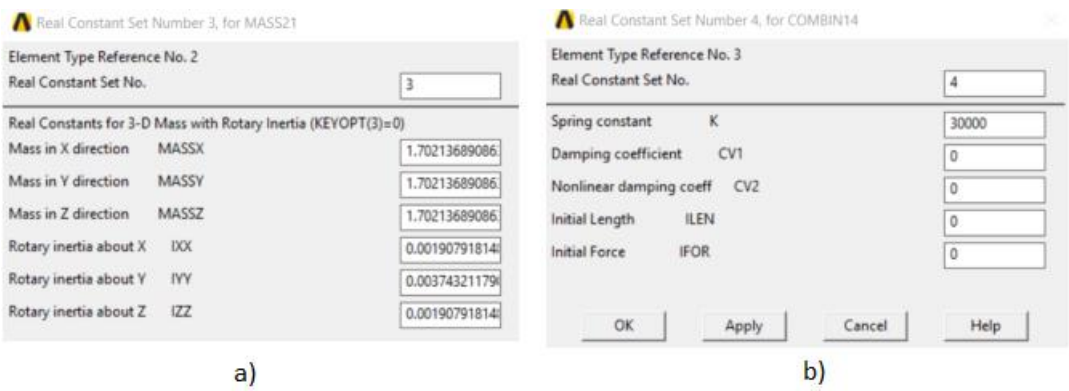

Figure 3.7: Properties window: a) Disk model; b) Bearing model.

To simulate an excitation through a mass unbalance (harmonic analysis), two vector forces were computed at the disk position in the X and Z directions. An important command used to specify whether the excitation frequency is synchronous or asynchronous with the rotational velocity of a structure in a harmonic analysis, is the SYNCHRO command.

Finally, to prepare the Campbell diagrams, the CAMPBELL command is used in the input file. The PLCAMP command plots Campbell diagram data and the PRCAMP command prints the Campbell dia-

gram data. For a modal analysis with multiple load steps corresponding to different angular velocities ω, the Campbell diagram shows the evolution of the natural frequencies [35].

3.3 Experimental Methodology

In this section, one presents the equipment used during the experimental tests and their main characteristics along with some precautions to consider during the installation. Then, one introduces the procedures and models utilized for each experimental test.

3.3.1 List of Equipment

The equipment used to perform the modal tests is listed in Table 3.1. These tests were carried out in the Vibration Lab of DEM/IST.

Table 3.1: Equipment used during the modal tests.

Equipment	Model
Impact Hammer	Brüel & Kjaer Type 8202
Force Transducer	PCB 280C01
Piezoelectric Accelerometer	Brüel & Kjaer Type 4508
Signal Analyser	Brüel & Kjaer Type 3560 D
Stroboscope with Portable Lamp	Brüel & Kjaer Type 4913
Pulse Software	Brüel & Kjaer Pulse Labshop Version 6.1.5

Impact Hammer

The excitation equipment used during this work was the impact hammer of Brüel & Kjaer Type 8202 equipped with a force transducer positioned between the hammer's head and the rubber tip (Figure 3.8), since both tests where carried out for low frequency ranges. This technique is very advantageous for this type of work since it requires few hardware and provides shorter measurement time, making it more accessible to readjust the experimental models and repeat the modal test as many times as necessary in order to obtain better results.

Figure 3.8: Image of the used impact hammer of Brüel & Kjaer Type 8202.

It is possible to assemble an additional mass on the back side of the hammer's head in order to apply more energy on impact, but considering that the modal tests where conducted on small structures the

attachment wasn't necessary. Table 3.2 shows some specifications of the impact hammer without the additional mass.

Table 3.2: Specifications of the hammer [36].

Type of tip	Force range (N)	Pulse Duration (ms)	Frequency range (Hz)	Hammer's mass (g)
Rubber	100-700	2.7	0-500	280
Plastic	300-1000	0.57	0-2000	280
Steel	500-5000	0.2	0-7000	280

Force Transducer

In order to measure the force response, one used the PCB 280C01 force transducer (Figure 3.9). This equipment is positioned between the impact hammer's head and the tip. Since this equipment is composed by moving parts, the transducer is screwed to the hammer's head. Thus it is important to ensure that the transducer is perfectly aligned with the hammer during the moment of impact in order to have a good force response measurement.

Figure 3.9: Image of the used force transducer PCB 280C01.

The main characteristics of the force transducer are displayed in Table 3.3, according to [37].

Table 3.3: Main characteristics of the force transducer PCB 280C01 [37].

Sensitivity (mV/kN)	Frequency range (kHz)	Mass (g)
112.41	0.03-36	22.7

Piezoelectric Accelerometer

To measure the structure's response, one utilized a piezoelectric accelerometer of Brüel & Kjaer Type 4508 attached to a mounting clip UA 1407, Figure 3.10. The accelerometer was attached to the structure with bee wax.

The signal's exit is transmitted using a coaxial cable 10-32 UNF and connects to the signal analyser using a BNC connector. It is important to mention that the accelerometer used is uni-axial, meaning that the acceleration measurements are all in a single direction. Thus it is critical to consider the accelerometer position in the setup procedure. Table 3.4 shows the main characteristics of this equipment, according to [38].

Figure 3.10: Piezoelectric accelerometer of Brüel & Kjaer 4508 and clip UA 1407.

Table 3.4: Main characteristics of the piezoelectric accelerometer.

Sensitivity (mV/ms^{-2})	**Frequency range (Hz)**	**Mass (g)**
10$\pm$0.05	0.3-8000	4.8

Signal Analyser

The dynamic signal analyser used during this work was the Brüel & Kjaer Type 3560 D, which is composed by 65 input channels and 7 modules. One of these modules is reserved for the DC Power Supply Unit Type 2826 and another used for a Controller Module. Thus, channel 1 from module 7 and channel 1 from module 1 were reserved for the accelerometer and for the force transducer respectively, Figure 3.11 [39].

Figure 3.11: Signal Analyser from Brüel & Kjaer Type 3560 D.

Stroboscope

An auxiliary equipment used in this work was the Brüel & Kjaer Type 4913, Figure 3.12. The Stroboscopic motion analyser/tachometer uses the phenomenon called persistence of vision to provide the illusion of ”freeze” or slow vibrational and rotational motion of the rotor, which normally would be too fast for the human eye to perceive [40]. When the machine is illuminated by the flashing light and the flash frequency rate is adjusted to the rotor’s spin frequency, an illusion of stationary or slowly moving machinery is obtained. This process allows to assess qualitatively how the system is behaving. In this particular case, the procedure helps to visualise if the rotor is operating near the first critical speed (Backward Whirl motion) or the second critical speed (Forward Whirl motion).

Figure 3.12: Stroboscope from Brüel & Kjaer Type 4913.

Pulse Software

The analyser platform used for data analysis, recording and data management was the Brüel & Kjaer Pulse Labshop version 6.1.5. Figure 3.13 shows the main page of the template, it is composed by four important windows that need to be easily accessible [17].

- Configuration - contains details of the inputs and outputs and specifies what instruments are connected.
- Measurement - used to setup signal grouping and specify which analysers are to be used.
- Function - used to setup the outputs of the analyser.
- Display - shows which measurements are currently displayed.

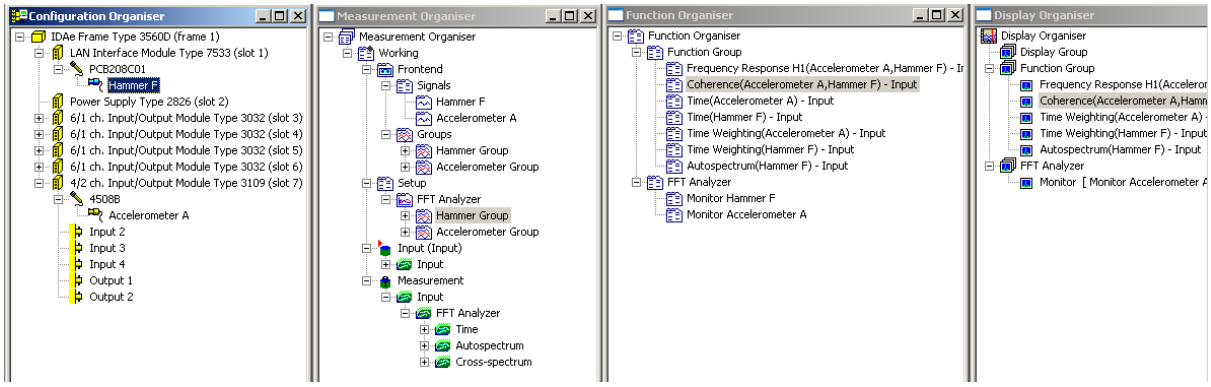

Figure 3.13: Pulse Labshop template.

To configure the transient window, the user right clicks the Hammer Group in the Measurement window and chooses ”properties”, Figure 3.14 b). In this window it is possible to change the shift time and length of the signal, where the shift time describes the duration until the window starts and the length sets how long the window will be.

For the exponential window, the user opens the ”properties” of the Accelerometer Group, Figure 3.14 a). This window allows the user to modify the shift time and the time constant τ of the signal, where τ describes the rate at which the exponential curve decays.

Finally, to configure the FFT, the user opens the ”properties” of the FFT Analyser in the Measurement window, Figure 3.15. In this window it is possible to choose the frequency span and the number of lines

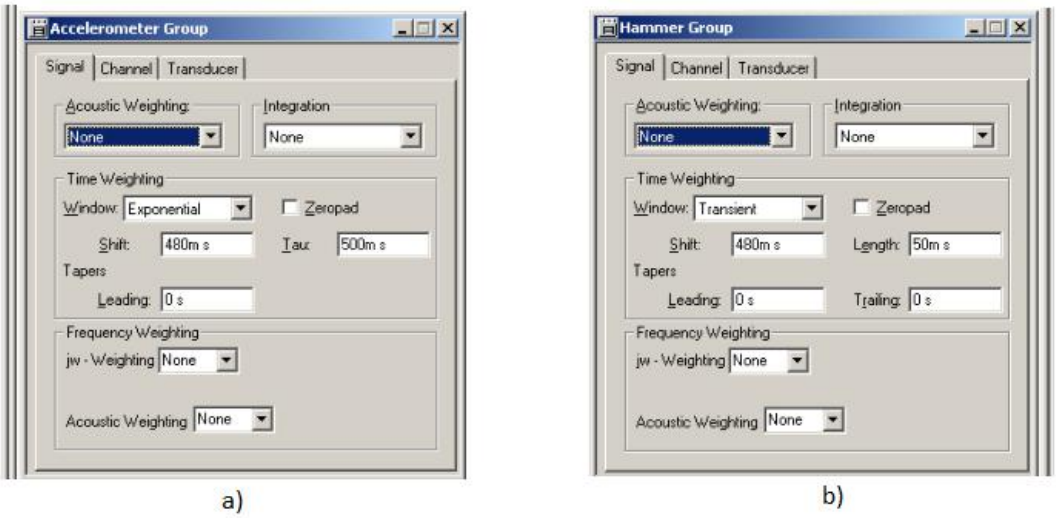

Figure 3.14: Window configuration: a) Exponential window; b) Transient window.

which the frequency axis is divided.

For more information on how to configure the template, the FFT Analyser and the transient/exponential windows, one can review the Pulse Labshop user guide [17].

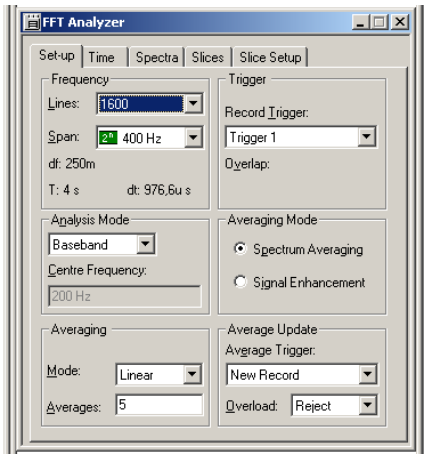

Figure 3.15: FFT window configuration.

3.3.2 Experimental Models

In this section, one presents the experimental models used in this work and the installation procedures to consider for each test.

Suspended Beam

This test is accomplished by analysing a rectangular cross-section beam, and compare its results with a predetermined numerical solution, obtained with the model developed in section 3.2.2. The beam's response was calculated under free body conditions, therefore the body was suspended on a portal crane using two nylon strings, as shown in Figure 3.16.

Figure 3.16: Beam suspended on a portal crane.

As already mentioned, the equipment of choice to excite the structure was the impact hammer equipped with a rubber tip, since one is dealing with a small structure and low frequency ranges. The additional mass on the hammer wasn't necessary for this test. The accelerometer was attached to the beam using bee wax and it was positioned at 2/3 of the beam's length in order to avoid nodes at least in the first and second mode shapes. Considering that the accelerometer used is uni-axial, the impact of the hammer was performed in the same position of the accelerometer but on opposite sides of the beam to make sure that no resonances were excited due to transverse modes, Figure 3.17.

Figure 3.17: Point of impact with the hammer.

A common source of error in modal testing is the oscillation of the wires that connect the accelerometer to the signal analyser, so it is important to make sure they are firm and their motion is well constrained.

Description of the Test Rig of the Machinery Fault Simulator (MFS)

The rotor system used to conduct the modal experiment for this thesis was the SpectraQuest's Machinery Fault Simulator (MFS) [41], illustrated in Figure 3.18.

The simulator is composed by a shaft supported by two rolling element bearings and it is connect to the motor through a coupling. The disk is located at 1/3 of the shaft's length in order to simulate the theoretical model introduced by Lalanne and Ferraris [3]. The unbalance mass can be introduced in the outer radius of the disk in order to excite the rotor for the critical speeds. The device is also equipped with a motor controller with a ON/OFF switch, which allows the user to manipulate the machine's spin frequency. The MFS comes with various optional kits that allow the operator to study different rotating machinery faults, being the critical study kit the one used during this work in order to gain practical knowledge in identifying resonance conditions.

Figure 3.18: SpectraQuest's Machinery Fault Simulator (MFS) used for resonance test [41].

Before explaining the procedure used to perform the modal tests in the MFS, it is important to emphasize the initial challenge that one had regarding the setup of the simulator. The preparation phase (which lasted nearly two months) was already complicated to begin with, since the equipment used to perform the tests hadn't been used for several years and it wasn't ready to carry out the pretended tasks. First, one had to prepare an inventory list of the equipment presented in the lab to ensure that all of the rotor system components were accessible and operational, being the critical study kit (set composed be an aluminium shaft, a steel disk, a coupling and two rolling element bearings) the most relevant for this particular work. Then, one had to go through the learning process on how to operate the simulator and how to assemble and disassemble the different components of each kit by resorting to the instruction manual provided by the manufacturer. After acquiring the necessary knowledge to operate the simulator, one started with the disassembling of the kit (shaft, disk, coupling and bearings) initially installed in the MFS (Figure 3.19), but since the machine hadn't been routinely maintained, it was necessary to lubricate the connections between the components in order to unscrew them.

Figure 3.19: SpectraQuest's Machinery Fault Simulator (MFS), initial rotor setup [41].

Subsequently, one proceeded with the installation of the critical study kit (displayed in Figure 3.18), an important aspect to consider is that the screws used to secure the components need to symmetrically tightened, for that reason one used a torque wrench calibrated with a tightening torque of 130 Ncm. Also, the necessary measurements of the rotor components were taken (disk radius and thickness, shaft radius and length, etc.).

Only after completing the preparations previously mentioned, one was capable of proceeding with the experimental tests presented below.

The experiment was divided in two stages in order to achieve the following objectives:

- Determine the rotor natural frequencies at rest;
- Obtain the rotor critical speeds.

The first stage was accomplished by performing the impact hammer test on the rotor system at rest. Once again, this method was chosen so that the user could readjust the rotor components, e.g. the disk position along the shaft, in order to perform more tests and acquire better results. The hammer was equipped with a rubber tip and no additional mass, since one was interested in a low frequency range. The test was carried out for three different locations, the shaft, the disk and the bearings. For each of these locations, measurements were made in X and Z directions by mounting the accelerometer in the horizontal and vertical directions respectively in order to determine the natural frequencies at rest in both directions, as illustrated in Figures 3.20 a)-f). Following the same approach used for the steel beam, measurements were done applying an impact on the opposite side of the accelerometer's position. In order to obtain good results with the MFS, one needs to be certain that all rotor components are well aligned, the fasteners are strongly tightened and the UNF cables are properly secured.

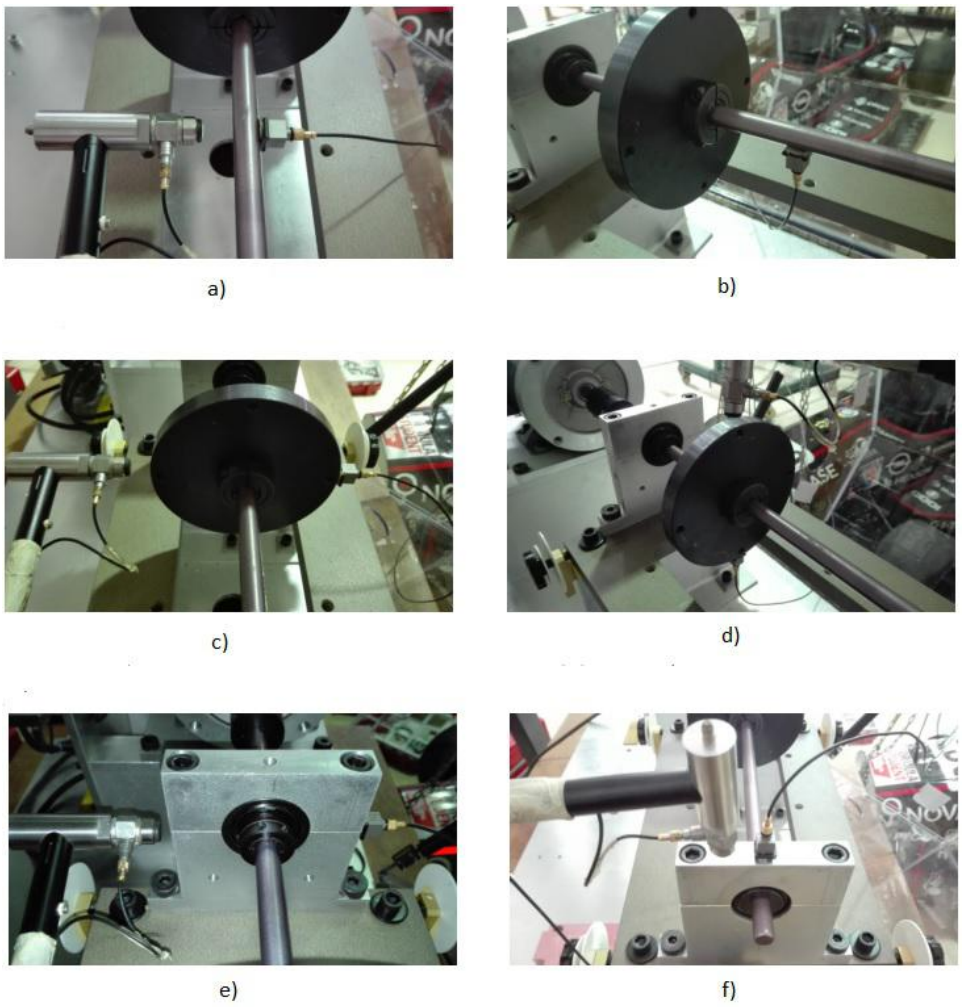

Figure 3.20: Accelerometer mounting positions: a) Shaft horizontally; b) Shaft vertically; c) Disk horizontally; d) Disk vertically; e) Bearing horizontally; f) Bearing vertically.

In the second stage, one computes the Autospectrum of the rotor machinery in operation to acquire the system critical speeds. Measurements were taken for four different rotation speeds (5 Hz, 10 Hz, 20 Hz and 30 Hz). Considering that the rotor must in motion throughout the procedure, the accelerometer was positioned in the bearings horizontally, as shown in Figure 3.21.

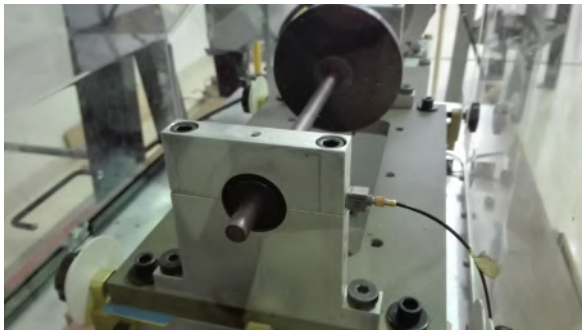

Figure 3.21: Rotor setup for second stage.

In order to visualise the physical phenomena of operating under critical conditions, a ”Start-Up” and ”Coast-Down” procedure was performed. The operator turns ON the MFS and increases the rotation speed slowly until the user hears a rumble and vibrations starts to increase. The speed is increased some more until the vibration reaches a peak in amplitude. The user keeps increasing the speed so that the vibration abates quickly, at that point the rotor just passed through the first and second critical speed, since both speeds are rather close as it will be shown in the next section. Finally, the operator reduces the speed passing through the critical speeds one more time until the MFS stops. Using the same security measures employed in the first stage, one must be certain that the MFS is in alignment, all fasteners are firmly tightened, the UNF cables are well secured and the protective cover is installed.

In addition, to witness the BW and FW motion, the Stroboscope was used. A yellow sticker was placed on the disk beforehand, in order to create a reference point, as shown in Figure 3.22.

Figure 3.22: Rotor disk with a yellow sticker.

By adjusting the flash rate frequency to the rotor’s first critical speed, one observes sticker’s rotation in the opposite direction of the disk’s rotation, indicating a BW condition. Readjusting the flash rate frequency to the rotor’s second critical speed the opposite case is observed, i.e., the sticker rotates in the same direction as the disk’s whirl, demonstrating a FW condition. For both the Stroboscope and ”Start-Up/Coast-Down” procedures a video recording was created.

Chapter 4

Results and Discussion

This chapter consists on the presentation and discussion of the analytical, numerical and experimental results obtained throughout this work. Reminding, the foremost objective of this thesis is related with the MFS equipment, for which after mounting the setup one would like to compare the natural frequencies and critical velocities obtained experimentally with the results from the analytical and numerical models, thus validating the numerical model (based on the FEM) used in this work. In order to do so, several steps were considered.

Section 4.1.1 starts with a convergence study between the finite element code conceived in $Matlab$, based on the finite elements presented in section 2.5, and the rotor's finite element model ($ANSYS$), mentioned in section 3.2.2, in order to verify the $Matlab$ script in terms of accuracy.

Afterwards, an analysis of the lateral dynamic behaviour of a symmetric and asymmetric rotor is implemented in section 4.2, i.e., the study of the natural frequencies, critical speeds, maximum displacement due to mass unbalance excitation forces and whirling motion of the rotor system. These studies are accomplished by comparing the output obtained with the numerical models against the results acquired with Rayleigh-Ritz model described in section 2.6.

After gaining insight on the rotor dynamic behaviour, a representation and discussion of the results acquired by the experimental models is made in section 4.3. These experimental results are then compared with the numerical data obtained.

Finally, in section 4.4, a case-study of a concrete aeronautical application is analysed, the bi-rotor of the propfan engine described in [42].

4.1 Mono-rotor from Lalanne and Ferraris

In this thesis, the three rotor models are based on the one introduced by Lalanne and Ferraris [3], illustrated in Figure 4.1. The rotor is composed by a shaft of length L, a rigid disk located at $Y = l_1$ and a discrete bearing located at $Y = l_2$. For the purpose of this thesis, one considers an undamped ($c_{xx} = c_{zz} = c_{xz} = c_{zx} = 0$) rotor. In the analytical and numerical models, both symmetric and asymmetric rotor are analysed. In the experimental model, one only considered the case of an

undamped and asymmetric ($k_{xx} \neq k_{zz} \neq 0$ and $k_{xz} = k_{zx} = 0$) rotor.

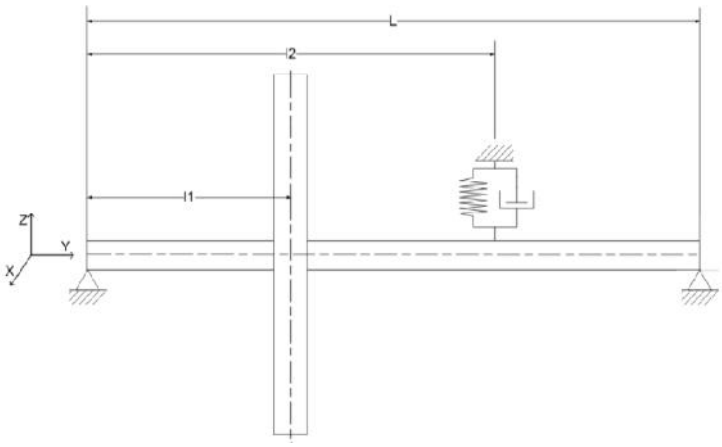

Figure 4.1: Model of the mono-rotor (source [4]).

The material properties, dimensions and relevant data of the rotor components illustrated in Figure 4.1 were adapted to the ones of the rotor experimental model used in the lab (MFS), whose characteristics are displayed in Table 4.1.

Table 4.1: Material properties and dimensions of the rotor components.

Disk Data	**Shaft Data**
Inner Radius: $R_1 = 0,0065m$	Length: $L = 0,34m$
Outer Radius: $R_2 = 0,066m$	Radius: $r = R_1 = 0,0065m$
Thickness: $h = 0.016m$	$S = 1,33 \times 10^{-4}m^2$
$M_D = 1,702kg$	$I = 1,402 \times 10^{-9}m^4$
$I_{Dx} = I_{Dz} = 0,001908kg.m^2$	$\rho_S = 2712kg/m^3$
$I_{Dy} = 0,00374kg.m^2$	$E_S = 69 \times 10^9 Pa$
$\rho_D = 7850kg/m^3$	
$E_D = 200 \times 10^9 Pa$	

4.1.1 Convergence Study

In this section, a convergence study is performed for the purpose of validating the developed FEM model in $Matlab$. In order to do so, a direct comparison between the results obtained from the finite element model developed in $Matlab$ with the model used in a commercial finite element program $ANSYS$ is performed.

The finite elements used in $Matlab$ code were described in section 2.5, while the $ANSYS$ finite elements were introduced in section 3.2.2. The $ANSYS$ element library provides a wide variety of of beam elements from which to choose, being the BEAM188 the one selected. Another possibility would be to use the BEAM4 element to compare against the $Matlab$ elements, since it is based on the Euler-Bernoulli theory, but it does not include the Coriolis forces and gyroscopic damping matrix and for that reason the BEAM188, with cubic interpolation, was used. The disk is considered as a rigid body, as such a structural mass element was chosen (MASS21), whose input values are the same as in Figure 3.7 a) (mass and rotary inertias about the element coordinate axis). Finally, the COMBIN14 element, a

2D longitudinal spring-damper element in the $X - Z$ plane, was used to represent the bearing.

The solving methods used for the modal analysis were introduced and described in section 2.5.6. An optimized numeric solver, the $polyeig$ function [29], was used in the $Matlab$ code in order to compute the eigenvalues and eigenvectors. In $ANSYS$, the corresponding solving method is employed using the QRDAMP command. Since one considers the disk and mass unbalanced to be positioned at $Y = l_1 = L/3$, and the bearing positioned at $Y = l_2 = 2L/3$, an equally spaced mesh is used with a first model using three equally sized elements along the shaft and the refined meshes using a number of elements multiples of the initial.

The convergence study is applied for the symmetric (with $k_{xx} = k_{zz} = 0$) rotor's frequency at rest, with $l_1 = L/3$, using as reference the first natural frequency obtained with a mesh composed by 60 finite elements for the $Matlab$ and $ANSYS$ finite element models. Table 4.2 indicates the first frequency value for both models using 60 elements.

Table 4.2: Frequency reference values for the $Matlab$ and $ANSYS$ models using 60 finite elements.

	Frequency Reference Value (Hz)
Matlab	$45,623698$
ANSYS	45.621131

Having established the reference values for the first natural frequency, one may now proceed with the convergence study with a graphical illustration, as shown in Figure 4.2.

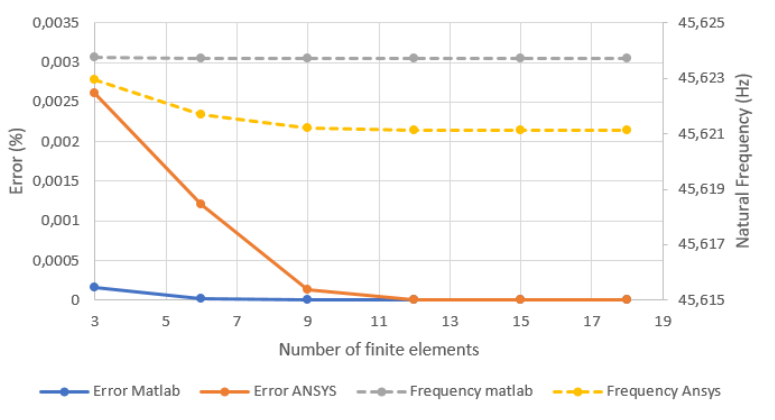

Figure 4.2: Evolution of the first natural frequency with mesh refinement at $\Omega = 0$.

Observing the graphic computed for different number of elements, having the computational costs into consideration, the solution converges using 15 elements for both $Matlab$ and $ANSYS$ models. Taking this into account, the boundary conditions are to be applied at nodes 1 and 16 of the shaft, the disk and mass unbalanced forces at node 6 and finally the bearing at node 12. An example of the rotor finite element model, using 15 elements (16 nodes), is illustrated in Figure 4.3.

Despite that both models converge rapidly, the $ANSYS$ finite element model does it monotonically faster. This occurs due to the fact that the $ANSYS$ BEAM188 Timoshenko element with cubic shape functions contains two added internal nodes and three point of integration along the element length, resulting in a quadratic variation of the element solution (rotations, displacements), while the $Matlab$

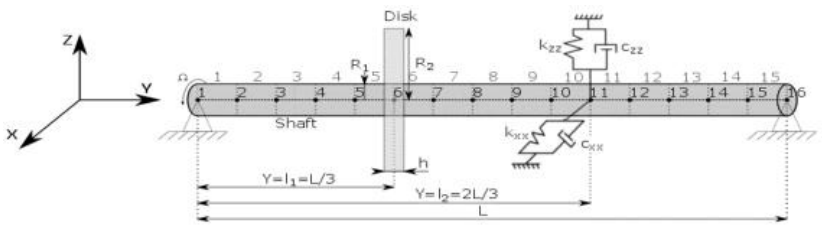

Figure 4.3: $Matlab$ finite element model of the mono-rotor using 15 elements (16 nodes) (source [43]).

Euler-Bernoulli beam element (with transverse shear correction) only uses two points of integration, leading to a linear variation of the element solution, which results in a ”stiffer” numerical behaviour, i.e. higher natural frequency values are obtained considering the same number of elements. Regardless, one may conclude that this convergence study leads to the validation of the finite element model developed in $Matlab$.

4.2 Numerical *versus* Analytical Model

After completing the convergence study, one proceeds to compare the results obtain with the FEM and the Rayleigh-Ritz method, considering the case of a symmetric and asymmetric rotor. Also, each case is carried out for two hypothesis, one where the disk is located in the middle of the shaft ($l_1 = L/2$) and a second where the disk is positioned at $l_1 = L/3$.

Initially, the Campbell diagrams obtained with the FEM and the Rayleigh-Ritz method are analysed. Then, a study of the system's response to an unbalanced excitation is performed for both methods, in order to support the results observed in the Campbell diagrams. These tests allow to examine the contrasts between both methodologies and helps to clarify the parameters influence on the results.

4.2.1 Symmetric Rotor

Campbell Diagram

Considering the undamped symmetric rotor (with null stiffness coefficients $k_{xx} = k_{xz} = k_{zx} = k_{zz} = 0$) of Figure 4.3, to determine the analytical solution one applied the methodology presented in section 3.1 to plot the Campbell diagram using equations 2.125 and 2.127. Having the rotors mass $[M]$, damping $[C]$ and stiffness $[K]$ matrices (from Equation 2.116), they are introduced in a polynomial eigenvalue solver (e.g. $polyeig$ in $Matlab$), which is used to obtain the roots $r_i = \pm j\omega_i$ of the characteristic equation 2.121 and the respective eigenfrequencies ω_i, for the interval $\Omega = [0, 9000][RPM]$.

For the FEM, one used the methodology described in section 2.5.6 to obtain the Campbell diagram, in $Matlab$, of the undamped symmetric rotor finite element model illustrated in Figure 4.3. After obtaining the rotors mass $[M]$, damping $[C]$ and stiffness $[K]$ matrices and using a polynomial eigenvalue solver (e.g. $polyeig$ in $Matlab$), one can obtain the roots $r_i = \pm j\omega_i$ for $\Omega = [0, 9000][RPM]$. For the $ANSYS$ model, one applies the methodology presented in section 3.2.2, the eigenfrequencies are determined

using the QRDAMP command in the input file, while the plot of the Campbell diagram is performed using the PLCAMP command and the PRCAMP command prints the Campbell diagram data.

Since the Campbell diagram curves obtained with the $Matlab$ model are practically identical to the curves acquired with the $ANSYS$ model, one decided to only illustrate a comparison between the Campbell diagrams of the $Matlab$ and Rayleigh-Ritz models. In order to view the Campbell curves obtained with the $ANSYS$ model as well as the mode shape that corresponds to the rotor's first natural frequency, one may consult Appendix B. Having clarified that, Figures 4.4 a) and b) illustrate the Campbell diagrams for the Rayleigh-Ritz method and the FEM considering the first hypothesis (disk positioned at $l_1 = L/2$) and the second hypothesis (disk positioned at $l_1 = L/3$).

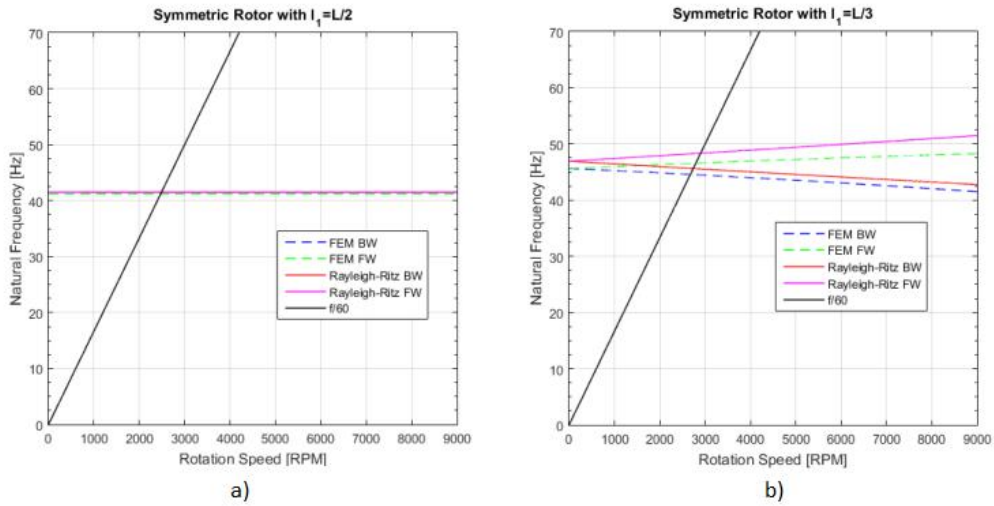

Figure 4.4: Campbell diagram of the symmetric rotor: a) Disk position $l_1 = L/2$; b) Disk position $l_1 = L/3$

Considering that one is dealing with a symmetric rotor, the natural frequencies at rest are the same for both Backward and Forward Whirl. In order to better compare these frequencies, Table 4.3 indicates the natural frequencies at rest and critical speeds (intersection points between the synchronous line and the frequency curves of the Rayleigh-Ritz and FEM model, in Figure 4.4) of the three models, considering both disk positions.

Table 4.3: Symmetric rotor first natural frequency at rest and critical speeds for both disk positions.

Method	**Frequency at Rest (Hz)**				**Critical Speeds (rpm)**			
	$l_1 = L/2$		$l_1 = L/3$		$l_1 = L/2$		$l_1 = L/3$	
	BW	**FW**	**BW**	**FW**	**BW**	**FW**	**BW**	**FW**
Rayleigh-Ritz	41,50	41,50	46,93	46,93	2490	2490	2738	2901
Matlab	41,15	41,15	45,62	45,62	2469	2469	2674	2795
ANSYS	41,39	41,39	45,71	45,71	2482	2482	2679	2801

Observing the results, one may conclude that for a disk position at $l_1 = L/2$, the frequency difference at rest and the critical speeds difference between the FEM and the Rayleigh-Ritz method are very low, which is to be expected.

However, for $l_1 = L/3$ the differences become more noticeable. This result has already been discussed in past literature, particularly in [3]. The frequencies at rest and critical speeds obtained using

the FEM are lower when comparing with the computed solution using the Rayleigh-Ritz method, which can be explained analysing the first mode shape. In the Rayleigh-Ritz method, the shape function $f(y) = \sin\left(\frac{\pi y}{L}\right)$ (Equation 2.98) is considered for the exact solution of a beam's first vibration mode. The shape function presents a maximum value of $f(y) = 1$ for $y = \frac{L}{2}$ and a minimum value of $f(y) = 0$ for $y = L$, implicating that the shape function does not take into account the effect of the concentrated mass (disk) located at $Y = l_1 = L/3$. This means that the analytical model presents a more restrictive behaviour when compared with the numerical model, i.e. more reliability only for a particular scenario ($l_1 = L/2$). Also, with the increase of the rotational speed the inertial forces start to have even more influence in stressing out the limitations of the shape function. Thus, one may anticipate better results from the FEM since the model's computed deformation has a better adjustment to the real deformation.

Mass Unbalanced

The next step introduces an additional study for a disk's location $l_1 = L/3$, with a mass unbalance $m_u = 0.1g$ positioned at a distance $d = R_e = 0,066m$ from the shaft's geometrical center and at an angular position $\alpha = 0^o$ with respect to the Z axis. The undamped symmetric rotor model with the added mass unbalanced is illustrated in Figure 4.5.

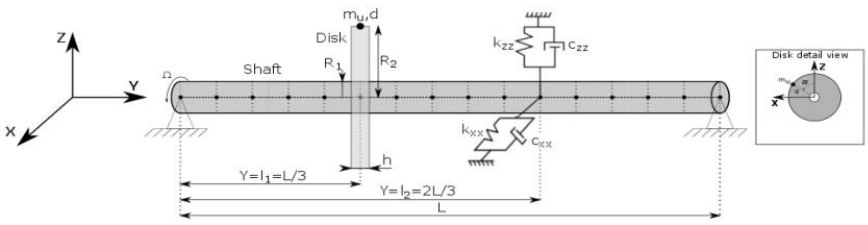

Figure 4.5: Undamped symmetric rotor with Mass Unbalanced at disk position $l_1 = L/3$ (source [43]).

For the analytical solution, one uses the methodology described in section 3.1, which states that a mass unbalanced applied in a rigid disk results in a synchronous harmonic force, as in Equation 2.95. The corresponding response amplitudes Q_1 and Q_2 at $l_1 = L/3$ can be obtained by solving the equations system 3.4, which corresponds to a steady-state analysis.

As for the FEM, one used the methodology presented in section 2.5.7. The same mass unbalanced is applied to node six of the undamped symmetric rotor FEM of Figure 2.5. The mass unbalanced placed on the disk results in a synchronous harmonic force, as in 2.95. Subsequently, the response amplitudes for displacements u, w (in the X and Z directions, respectively) are obtained for the finite element model using equation 2.92.

Knowing that the amplitude Q_i is dependent of the rotation speed Ω, one may plot the Response diagram as illustrated in Figures 4.6 a) and b).

Observing the rotor's response in Figure 4.6, one notices that the displacement evolution, with the rotation speed Ω, is equal in both directions (u and w), which is to be expected for a symmetric rotor. Also, the asymptote of the finite element response is located at a lower spin speed, since the critical speeds obtained with the Rayleigh-Ritz method are higher when compared with those acquired with the FEM.

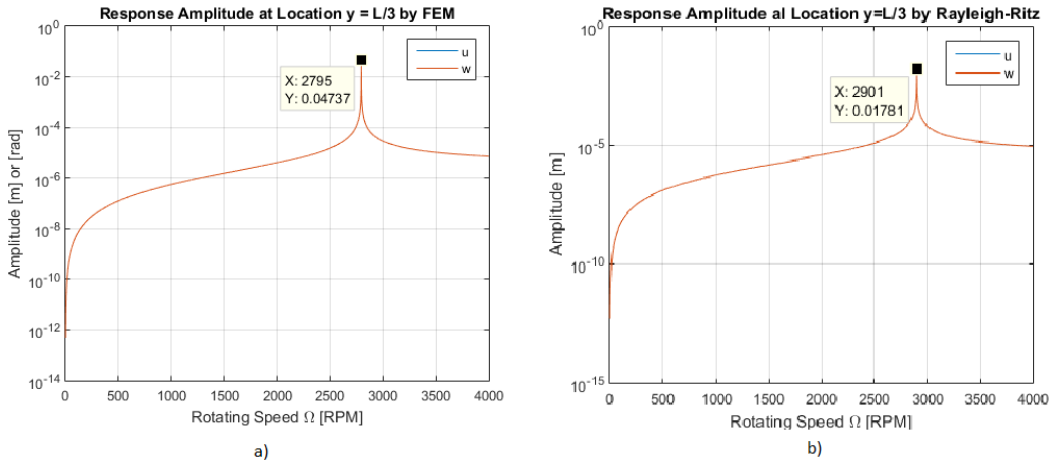

Figure 4.6: Response diagram symmetric rotor ($l_1 = L/3$): a) FEM; b) Rayleigh-Ritz.

The amplitude is null at zero rotating speed, since the mass excitation force has a speed-square characteristic. In the sub-critical range the harmonic motion grows from zero to its maximum at the system's critical speed. Throughout the sub-critical range, the deflection is manly dominated by the system's stiffness and as the spin speed increases so does the influence of the inertial forces (specially the centrifugal force), which is responsible for the accentuated response growth.

During the growing stage, the harmonic response remains in phase with the excitation for both transverse directions (observe Equation 2.93 and Figure 2.11), which means that the vector $\bar{OC}$ rotates synchronously with the rotation speed in the XZ plane, staying aligned with vector $\bar{OD}$. Thus, one may confirm that the amplitude grows asymptotically and reaches a peak located at the Forward Whirl critical speed, verifying that mass unbalanced forces only excite the Forward Whirl modes in the case of a symmetric rotor.

Having established the symmetric rotor study, one proceeds with the analysis of the asymmetric rotor.

4.2.2 Asymmetric Rotor

Campbell Diagram

In this section, similar to what was done in section 4.2.1, one is interested in plotting the Campbell diagram. In order to do so, one determines the analytical solution applying the methodology presented in section 3.1 to the same model (Figure 4.3), except that now is added a bearing positioned at $l_2 = 2L/3$ with a stiffness coefficient of $k_{xx} = 2,3 \times 10^4 N/m$ in the X direction and $k_{zz} = 1,27 \times 10^5 N/m$ in the Z direction. After obtaining the rotors mass $[M]$, damping $[C]$ and stiffness $[K]$ matrices (from Equation 2.116), these are introduced in a polynomial eigenvalue solver (e.g. $polyeig$ in $Matlab$), which is used to obtain the roots $r_i = \pm j\omega_i$ of the characteristic equation 2.121 and the respective eigenfrequencies ω_i (Equations 2.125 and 2.127), for the interval $\Omega = [0, 9000][RPM]$.

As for the FEM, the methodology presented in section 2.5.6 was used to obtain the Campbell diagram of the undamped asymmetric rotor finite element model illustrated in Figure 4.3. Just like the

symmetric rotor, having obtained the rotors mass $[M]$, damping $[C]$ and stiffness $[K]$ matrices and using a polynomial eigenvalue solver (e.g. $polyeig$ in $Matlab$), one can obtain the roots $r_i = \pm j\omega_i$ for $\Omega = [0, 9000][RPM]$. In $ANSYS$ environment, the methodology described in section 3.2.2 is applied to the rotor model, the QRDAMP command is used to determine the eigenfrequencies, the PLCAMP plots the Campbell diagram and the PRCAMP command prints the Campbell diagram data.

Due to the same reasons already explained for the symmetric rotor in section 4.2.1, the Campbell curves obtained with the $ANSYS$ model and the first natural frequency mode shape are shown in Appendix B. The Campbell diagram for the first Backward and Forward modes considering the first hypothesis ($l_1 = L/2$) is illustrated in Figure 4.7 a) and for the the second hypothesis ($l_1 = L/3$) the Campbell Diagram is displayed in Figure 4.7 b).

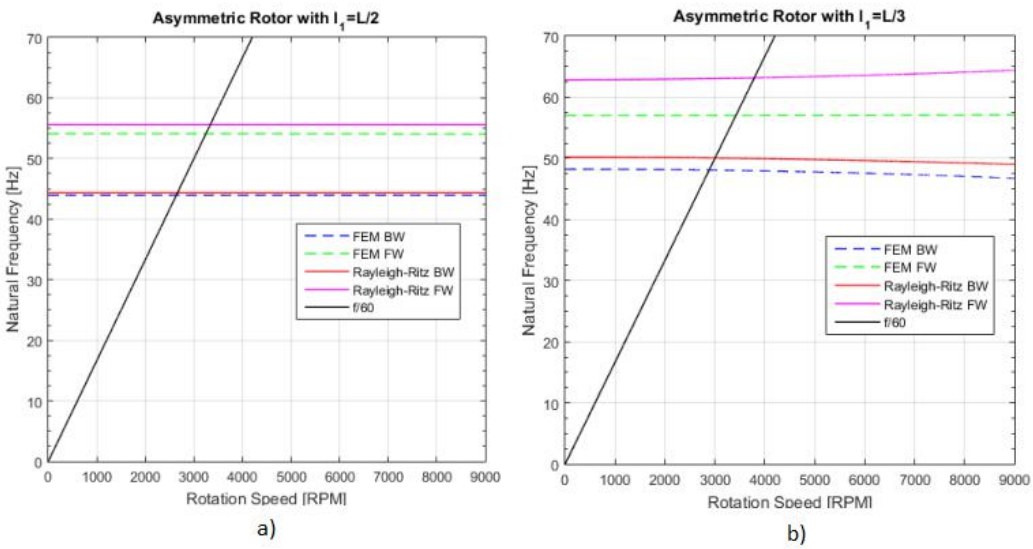

Figure 4.7: Campbell Diagram of the asymmetric rotor: a) Disk position $l_1 = L/2$; b) Disk position $l_1 = L/3$.

Comparing the asymmetric rotor Campbell diagrams from Figure 4.7 a) and b) with the diagrams obtained for the symmetric rotor (Figures 4.4 a) and b)), significant changes take place. In the case of a asymmetric rotor, the Campbell Diagram displays two different natural frequencies at rotation speed $\Omega = 0rpm$, which demonstrates an alteration in the dynamic behaviour of the rotor system. Due to the fact that the spring adds stiffness to the system, the natural frequencies are now sensible to different stiffness characteristics in the X and Z directions, causing the FW and BW curves to drift apart contrary to the symmetric rotor. Given that $k_{zz} > k_{xx}$, one notices that the frequency values in the X direction have a lower increase when compared with the increment of the natural frequencies in the Z direction for all three models.

Table 4.4 presents the natural frequencies and the critical speeds of the three models for both disk positions.

Regarding the critical speeds, the effect of adding bearing stiffness is similar to what occurred in the natural frequencies, the critical speeds are higher when compared with the ones obtained with the symmetric rotor in Table 4.3. Once again, the frequencies difference and critical speeds difference

Table 4.4: Asymmetric rotor first and second natural frequency and critical speeds for both disk positions.

Method	Frequency at Rest (Hz)				Critical Speeds (rpm)			
	$l_1 = L/2$		$l_1 = L/3$		$l_1 = L/2$		$l_1 = L/3$	
	BW	**FW**	**BW**	**FW**	**BW**	**FW**	**BW**	**FW**
Rayleigh-Ritz	44,38	55,59	50,19	62,87	2663	3335	3003	3790
Matlab	43,93	54,11	48,22	57,03	2636	3246	2884	3423
ANSYS	44,26	54,92	48,32	57,17	2655	3294	2890	3431

between the numerical models and the Rayleigh-Ritz model (calculated for $l_1 = L/2$) are very small, although these differences are much higher for a disk positioned at $l_1 = L/3$, due to the same reasons already explained for the symmetric rotor.

Mass Unbalanced

Similar to what was done for the symmetric rotor in section 4.2.1, a mass unbalanced $m_u = 0.1g$ positioned at a distance $d = R_e = 0,066m$ from the shaft's geometrical center and at an angular position $\alpha = 0^o$ with respect to the Z axis, is added to node six of the undamped asymmetric rotor finite element model of Figure 4.5.

To acquire an analytical solution, one used the methodology presented in section 3.1 in order to determine the response amplitudes Q_1 and Q_2 at $l_1 = L/3$ by solving equations system 3.4.

For the FEM, the methodology described in section 2.5.7 is applied to determine the response displacements u and w (in the X and Z directions, respectively) of the undamped asymmetric rotor finite element model (Figure 4.5).

The Response diagrams of the asymmetric rotor for the FEM and Rayleigh-Ritz method are shown in Figures 4.8 a) and b).

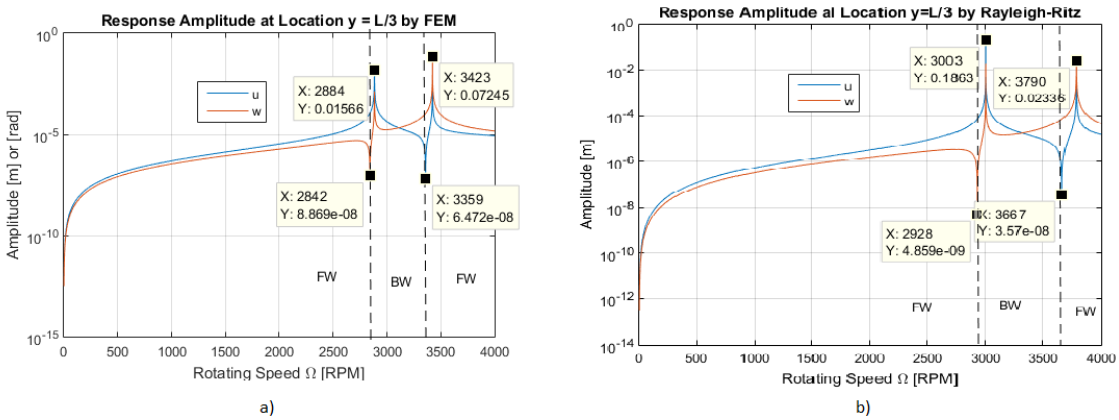

Figure 4.8: Response diagram asymmetric rotor ($l_1 = L/3$): a) FEM; b) Rayleigh-Ritz.

Observing the previous graphics, it clearly illustrates two maximum amplitudes located at the same system's critical speeds for each respective model, as shown in Table 4.4. This shows that the mass unbalanced forces may excite both BW and FW frequencies in the case of asymmetric rotors. During the sub-critical range one observes that the response amplitude u (in X direction) presents a higher value than w (in the Z direction). This can be justified by the fact that the bearing stiffness in the Z direction is

higher than the one added in the X direction, $k_{zz} > k_{xx}$.

As the spin speed Ω reaches the first critical speed ($2842RPM$), the response amplitude w rapidly decreases, which signal a mode change from a FW to a BW mode. Likewise, as the spin speed reaches the second critical speed ($3423RPM$) the response amplitude u decreases, but for this case the mode changes from BW to FW.

Additionally, the displacement u is maximum in the first critical speed (indicating an horizontal critical speed, i.e. in the X direction) due to the added stiffness, as already explained. On the other hand, w is higher in the second critical speed (indicating a vertical critical speed, i.e. in the Z direction) which is explained by the fact that the mass/inertia effect surpasses the added stiffness effect.

Comparing the FEM values with the results acquired with the Rayleigh-Ritz method, although the analytical solution displays a correct behaviour in terms of whirling motion, the values of critical speeds and response amplitudes u and w are substantially different, due to the effects regarding the shape function, explained in section 4.2.1.

4.3 Numerical *versus* Experimental Model

In this section, one compares the numerical results with the data obtained from the experimental models. Section 4.3.1 shows a comparison between the steel beam finite element model, described in section 3.2.2, and experimental model presented in section 3.3.2. Section 4.3.2 presents the experimental results acquired with the rotor experimental model (MFS) presented in section 3.3.2. The experimental data is then compared with the results obtained with the FEM discussed in section 4.2.2, in order to validate the numerical methodology.

An important aspect to consider is that the numerical models need to be frequently adjusted to the experimental models. Considering that these are related to simple structures, one chose to readjust their global properties (i.e. the Young's Modulus and density) as well as the bearing stiffness coefficients k_{xx} and k_{zz} (for the rotor model) so that the numerical models could represent more accurately the behaviour observed experimentally.

4.3.1 Beam Experimental Results and Comparison

In this section, one compares the beam's results extracted by the numerical model with the data obtained with the experimental test. To determine the numerical solution, one used the methodology presented in section 3.2.2 applied to the beam finite element model illustrated in Figure 4.9, with the following properties: Young's modulus $E = 185GPa$; Poisson's coefficient $\nu = 0.3$; mass density $\rho = 7820kg/m^3$; length $L = 800mm$; height $h = 21mm$ and width $w = 5.5mm$.

The numerical results (see section 3.2.2), are obtained using the following parameters to define the geometry of the beam: 2 keypoints; 1 line and the respective mesh defined by 50 finite elements per line.

For the experimental test, one applied the methodology described in section 3.3.2 to the steel beam,

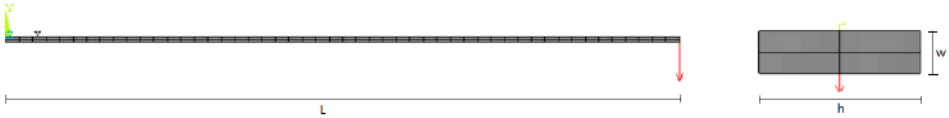

Figure 4.9: Steel beam finite element model parameters identification.

illustrated in Figure 4.10, with the same mechanical properties as the ones used by the numerical model. The specimen was suspended on a portal crane using two nylon strings, to simulate free body conditions. The uni-axial accelerometer was attached at 2/3 of the beam's length and an impact hammer equipped with a rubber tip was used to excite the structure.

Figure 4.10: Steel beam experimental setup.

In order to analyse the experimental results, the FFT in Pulse software was configured to use 1600 lines until 400 Hz, providing a response duration of 4s and an interval of 0,25 Hz between readings, Figure 3.15. The hammer was configured to use a transient window in order to capture the impact signal for a duration of 50 ms (Figure 3.14 b)). For the accelerometer, one used an exponential window with a time constant of 500 ms (Figure 3.14 a)). The force signal was supervised in order to verify its stability through the frequency range and the estimator H_1 was used to obtain the FRF. Figure 4.11 presents the FRFs computed from the steel beam experimental and numerical models.

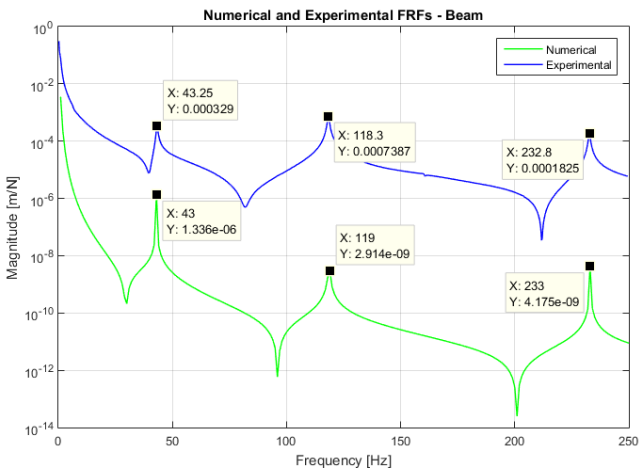

Figure 4.11: Frequency response function of the steel beam.

Analysing the graphic, it is easy to identify the models first, second and third natural frequencies. Although the study of antiresonance is considered out of scope of this thesis, one notices that the

frequencies that corresponds to the antiresonance peaks are different in both curves. This may be explained by the fact that hammer's impact position was different from the location of the unitary force used in the harmonic analysis. Also, the difference in amplitude may be explained by the different forces applied (in FEM, $F = 1$).

Table 4.5 represents the first three natural frequencies determined from the numerical model, created in *ANSYS*, and the experimental model.

Table 4.5: First three mode shapes and natural frequencies of the steel beam numerical and experimental model.

Mode Shapes	ANSYS	Experimental
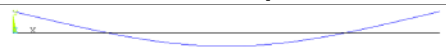	$f_1^n = 42,96Hz$	$f_1^e = 43,25Hz$
	$f_2^n = 118,58Hz$	$f_2^e = 118,30Hz$
	$f_3^n = 232.96Hz$	$f_2^e = 232,82Hz$

Observing the results from Table 4.5, one may confirm that the numerical model is well adjusted to the experimental model in terms of the natural frequencies, completing the objectives established for this particular test. At this point, one has verified the proper functioning of the lab equipment in order to proceed to the model test in the MFS.

4.3.2 MFS Experimental Results and Comparison

In this section, one compares the results obtained in section 4.2.2, with the experimental data collected using the methodology (first and second stage) presented in section 3.3.2 for the MFS system. The properties of the experimental model are also displayed in Table 4.1.

First Stage - MFS Rotor at Rest

The results obtained with the rotor finite element model (discussed in section 4.2.2) provided a good estimation of the its natural frequencies (Table 4.4), which is crucial to better interpret the experimental FRFs acquired for the experimental rotor at rest.

The experimental test performed in this stage follows the methodology described in section 3.3.2 applied to the experimental rotor system at rest, shown in Figure 4.12. Measurements of the rotor's response were performed for the six pre-established accelerometer positions (Figures 3.20 a)-f)): D_X; D_Z; S_X; S_Z; B_X and B_Z. The hammer was equipped with a rubber tip and the impact was performed on the opposite side of the accelerometer's position.

For this stage, the FFT (in Pulse) was configured to use 1600 lines until 100 Hz, with a response duration of $T = 16s$ and an interval of 0,0625 Hz between readings. The impact hammer was configured using a transient window in order to capture the impact signal for a duration of 50 ms. For the accelerometer, one applied an exponential window with a time constant of 500 ms and the estimator H_1 was used to obtain the FRF. Figure 4.13 illustrates the rotor's frequency response (in terms of mechani-

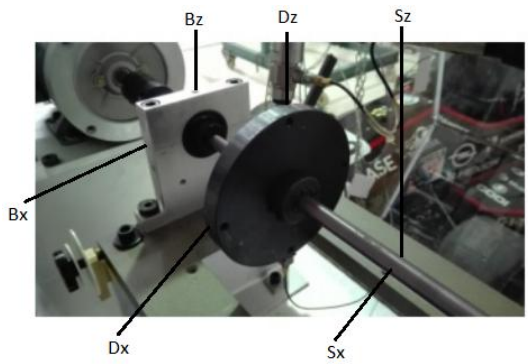

Figure 4.12: Rotor experimental model (first stage) and accelerometer position identification.

cal receptance) for the six pre-established accelerometer measurement positions: D_X, D_Z, S_X, S_Z, B_X and B_Z.

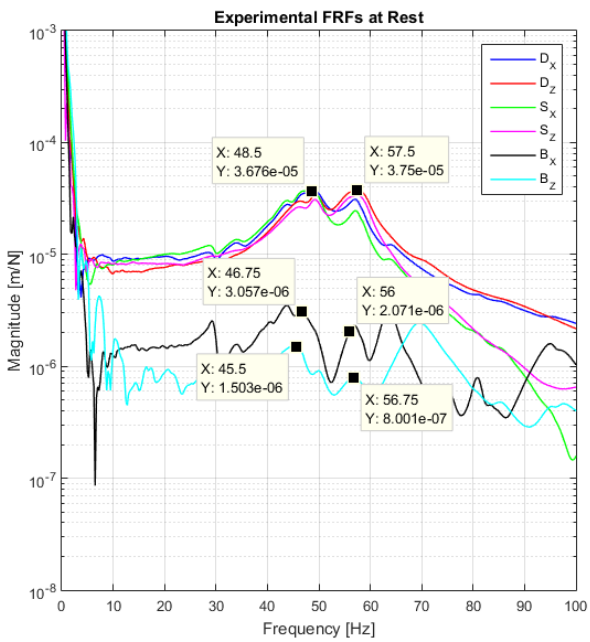

Figure 4.13: Frequency response functions of the disk, shaft and bearings on the horizontal and vertical directions, using the impact hammer.

Observing Figure 4.13, one highlighted some of the peaks that represent the expected first and second natural frequency of the rotor. It is important to mention that not all peaks considered are marked in the graphic since it would overload it with information. To view the FRF curves separately along with all their points of interest, one may consult Appendix C. Table 4.6 shows the frequencies of interest that correspond to the first and second natural frequencies of each curve and the calculated average for each frequency.

In order to compare the natural frequencies obtained with the numerical method (see Table 4.4) and the experimental method, the frequencies difference between the experimental and numerical models is shown in Table 4.7.

Examining the results from Table 4.6, one notices that in most cases the natural frequencies of the

Table 4.6: Experimental first and second natural frequencies (Hz) and respective averages.

Frequency at Rest	Accelerometer Position						Average
	D_X	D_Z	S_X	S_Z	B_X	B_Z	
ω_1	49	49,25	47,5	49,25	46,75	45,25	47,80
ω_2	57	57,5	57,25	57,5	57	56,75	57,19

Table 4.7: Difference between the first and second natural frequency of the numerical and experimental models.

Method	Freq. Difference (Hz)	
	ω_1	ω_2
Experimental vs Matlab	0,42	0,16
Experimental vs ANSYS	0,52	0,02

experimental model are higher than the numerical models frequencies. An important aspect to consider is that the numerical model doesn't represent the complete experimental model, since the external components of the MFS (such as the support plate, the protective cover and the electrical motor) were not computed in the numerical model, which could be influencing the discrepancy between the numerical and experimental results. This is specially true in the case of the bearing's FRF curve, considering that this component connects the shaft to the other parts of the MFS. In this particular curve, other peaks besides the ones that correspond to the first and second natural frequency are quite noticeable.

Regardless, observing the results from Table 4.7 one may conclude that the natural frequencies acquired by the experimental model are very similar to the ones obtained with both numerical models, contributing to the validation of the numerical models. Having completed the natural frequency study, one proceeds with the analysis of the critical speeds.

Second Stage - MFS Rotor in operation

Once again, the results acquired with the rotor finite element model (section 4.2.2) offered a good estimation of the rotor behaviour in terms of critical speeds, allowing a more effective analysis of the experimental Autospectrum.

For this stage, one used the methodology described in section 3.3.2 to the experimental rotor in operation. Measurements were taken considering four operational spin speeds (5 Hz, 10 Hz, 20 Hz and 30 Hz). During the whole procedure the accelerometer was positioned horizontally on the bearing (B_X), as illustrated in Figure 4.14.

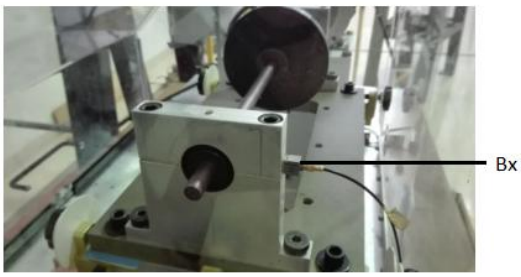

Figure 4.14: Rotor experimental model (second stage) and accelerometer position identification.

The signal analyser (in Pulse) was configured to obtain the Autospectrum function. For the FFT, one defined a frequency range of 100 Hz, with 1600 lines resulting in a interval of 0,0625 Hz between readings and a response duration of $T = 16s$. The record trigger was switched to "Free Run", since there is no impact hammer being used and the excitation force derived from the rotor's own rotational motion (Figure 3.15). For the accelerometer, a more appropriate window was used for this type of test, i.e., "Hanning" window and the estimator H_1 was applied to compute the functions. Figure 4.15 represents the Autospectrum function (in terms of mechanical receptance) considering four shaft spin speeds: 5 Hz, 10 Hz, 20 Hz and 30 Hz.

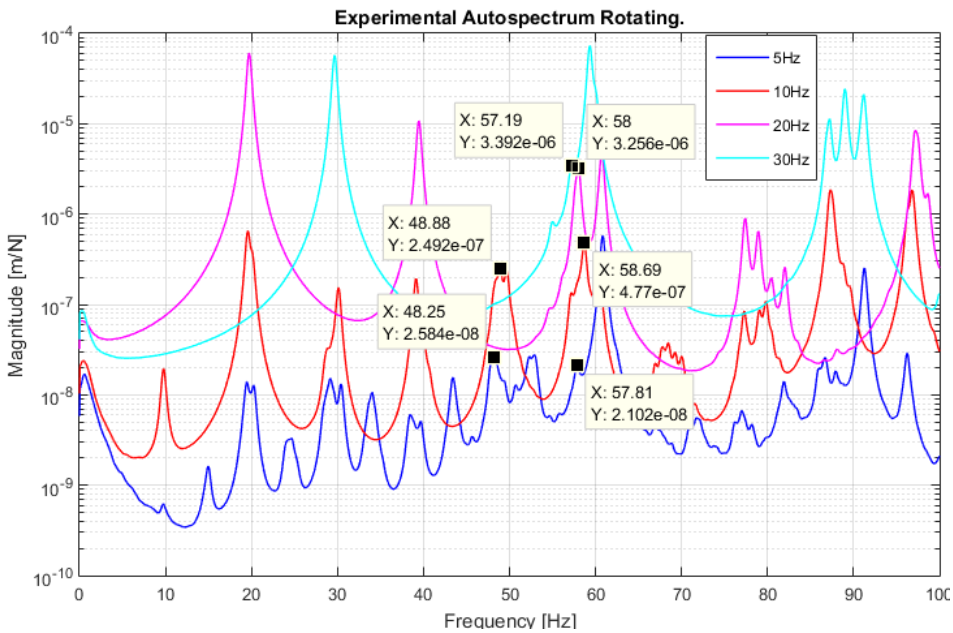

Figure 4.15: Experimental Autospectrum of the MFS, considering a rotation speed of 5 Hz (300 RPM), 10 Hz (600 RPM), 20 Hz (1200 RPM) and 30 Hz (1800 RPM).

Examining the graphic, one notices that each curve indicates a clear maximum at the rotor's rotating frequency and their respective multiples. For example, the Autospectrum that corresponds to a spin speed of 20 Hz presents a peak exactly at that frequency and (with a lower intensity) at higher multiples (40 Hz, 60 Hz,...), but these are not the frequencies of interest. As a result, one decided to mark the peaks that represent the expected first and second critical speeds values, as shown in Figure 4.15. For a closer inspection, one may consult Appendix D, which displays the Autospectrum curves separately. Table 4.8 displays the first and second critical speed ($\Omega(Hz) = \frac{\Omega(rpm)}{60}$) along with the computed average for each speed.

Table 4.8: Experimental first and second critical speeds.

Critical Speeds (Hz)	**Shaft Spin Speed (Hz)**				**Average (Hz)**
	5	**10**	**20**	**30**	
Ω_1	48,25	48,88	-	-	48,57
Ω_2	57,81	58,69	58,06	57,19	57,98

To compare the critical speeds determined with the numerical method (see Table 4.4) and the experimental method, the critical speeds difference between the numerical and experimental models is shown

in Table 4.9.

Table 4.9: Difference between the first and second critical speed of the numerical and experimental models.

Method	C. S. Difference (Hz)	
	Ω_1	Ω_2
Experimental vs Matlab	0,50	0,51
Experimental vs ANSYS	0,52	0,72

Observing the results from Table 4.8, one notices that the first critical speed was not detected by the autospectrum curves that correspond to a shaft spin speed of 20 Hz and 30 Hz, implying that BW peaks are usually not observed in practice. This occurs due to the high damping effect of these curves. For this reason, one decided not to show autospectrum curves for high rotational speeds, since for Ω values greater than 30 Hz no other peaks were observed other than the operating frequency and its multiples.

Nevertheless, good accuracy is obtained, at least for the first two critical speeds, without considering "foundation" effects. Analysing the results displayed in Table 4.9, one concludes that the critical speeds obtained with the experimental model are very close to the ones acquired with both numerical models. Thus, the combination of the results achieved in the first and the second stage offer the validation of the numerical methodology (FEM), completing the main objective of this thesis.

Additionally, the study performed with the stroboscope, described in the end of section 3.3.2, allowed to confirm the mode changes from FW to BW motion and vice-versa. Adjusting the stroboscope flash rate frequency to the rotor's first critical speed ($\simeq 48,07Hz$ or $2884RPM$), one observed a sticker rotation in the opposite direction of the disk's rotation, displaying BW conditions as expected by inspection of the Campbell diagram (Figure 4.7 b)) and the Response diagram (Figure 4.8 a)). The opposite case is observed when the flash rate frequency is adjusted to the rotor's second critical speed ($\simeq 57,05Hz$ or $3423RPM$), showing a sticker rotation in the same direction as the disk's whirl, which proves that the rotor just changed from BW to FW motion.

After acquiring the validation of the numerical method, one is ready to implement the FEM to the Propfan Engine, as shown in the next section.

4.4 Case Study-Propfan Engine

In this section, the numerical methodology previously presented is now applied to the Propfan jet engine of the DUPRIN (DUcted PRopfan INvestigation) European research programme [44], illustrated in Figure 4.16 a). The primary objective of this programme was to develop a highly efficient and low consumption jet engine, through the use of an High Bypass Ratio, in order to fulfil the need of a more sustainable aircraft in the aerospace industry. The engine includes a four stage turbine capable of developing a maximum power of 160 kW and rotations speeds up to 16000 rpm.

To build the finite element model in $ANSYS$ environment, one had to consider some simplifications of the designed propfan, such as the simplification of the reduction gearboxes to a rigid element. By applying this adjustment, one is able to obtain a shaft maximum rotational speed of 16000 rpm. Con-

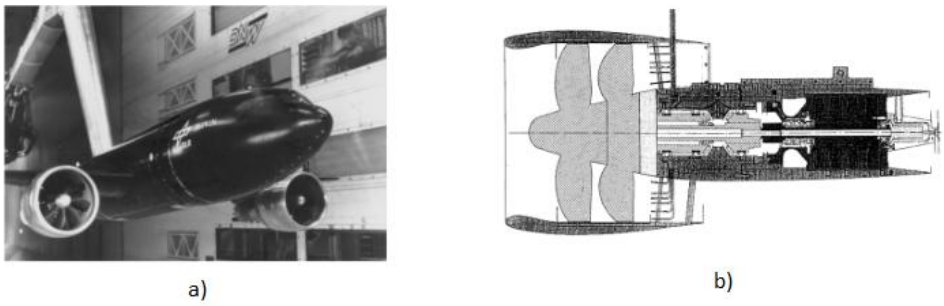

Figure 4.16: The DUPRIN Propfan: a) Prototype b) Jet engine cross-section (source [42]).

sidering that there is only torsional coupling between the shafts and the turbine, it is possible to study the dynamic behaviour of the shaft and blades separately from the turbine. Having said that, only the dashed parts (light grey) of the engine represented in Figure 4.16 b) were modelled, which include the fan blades, inner and outer shafts and the bearings.

4.4.1 The Model

The considered structure was initially modelled by Ferraris in [42] and it was submitted to a modal and unbalanced response analyses. Since neither the specific dimensions nor the materials properties were found in literature, one resorted to the work developed by Pedro Paulo [45] and Rafael Carvalho [4], whose adaptation of the available schematics and dimensions provided an approximate model in order to reproduce the results acquired by Ferraris. The final result is the schematic shown in Figure 4.17.

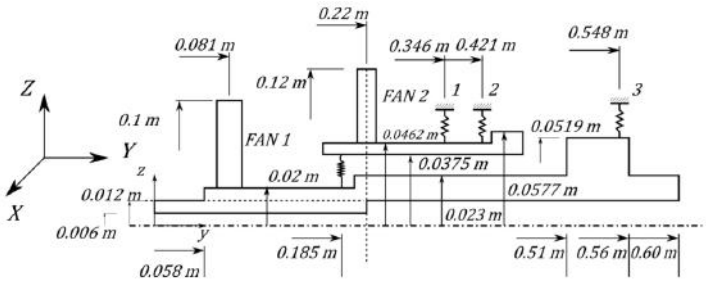

Figure 4.17: Revolution section of the propfan model (source [45]).

The propfan model consists of two fans attached to two shafts rotating with the same spin speed ($\Omega_1 = \Omega_2$) but in opposite directions. The shafts are supported by three bearings with stiffness values only in the X and Z directions and are connected by an intershaft bearing (represented by a rigid bearing that couples the transverse displacements of both shafts). Additionally, one used a quality factor $Q = 50$ to characterize the material damping. Its value is the same as estimated in [42], whose authors believed it as the best one to describe the engine's dynamic behaviour.

Considering that the material properties of the propfan components and bearing stiffness values were not found, one had to adjust their values so that the model created in this work could reproduce the results acquired by Lalanne [42] more accurately. Thus, the titanium disk and the steel shaft properties

as well as the bearings stiffness values are presented in Table 4.10.

Table 4.10: Material and Bearing properties for the propfan model.

Material Properties		**Bearing Stiffness (N/m)**
Stainless Steel	**Titanium**	
$\rho = 7800kg/m^3$ (Density)	$\rho = 4693kg/m^3$ (Density)	$k_{xx_1} = k_{xx_2} = 1,2 \times 10^8$
$E = 210GPa$ (Young Modulus)	$E = 140GPa$ (Young Modulus)	$k_{xx_3} = 10^9$
$\nu = 0,3$ (Poisson Ratio)	$\nu = 0,32$ (Poisson Ratio)	$k_{zz_{1,2,3}} = 1,5 \times k_{xx_{1,2,3}}$

To compute the dynamic properties of the propfan engine, a finite element model was built in $ANSYS$ environment, illustrated in Figure 4.18. The shafts were modelled as beam elements (BEAM188). The inner shaft was divided in 25 elements and the outer one was divided in 15 elements, as it was used by Ferraris [42]. The disks were modelled as rigid bodies of punctual mass (MASS21) and the bearings are considered as spring elements (COMBIN14). Also, to include the quality factor Q one used the function MP/DMPR.

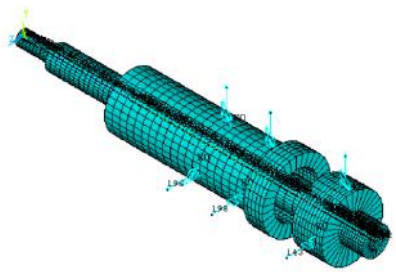

Figure 4.18: The Finite Element Model of the Propfan.

Having established the finite element model, a modal analysis was performed in order to obtain the Campbell Diagram and extract the engine critical speeds. Lastly, a mass unbalance response analysis was applied to plot the response diagram. The results acquired from both analysis were then compared with the ones displayed by Ferraris in [42].

4.4.2 Propfan Results and Discussion

In order to study the rotor dynamic response, one started by performing a free vibration analysis. The Campbell diagrams obtained with the considered model and the compared reference are displayed in Figures 4.19 a) and b), with a rotating speed range from 0 rpm till the turbine's maximum spin speed 16000 rpm.

Observing the previous graphics, one notices that the FW and BW curves are separated, due to different bearing stiffness values in the X and Z directions. Also, their frequencies are more or less constant throughout the rotation speed range, which is a consequence of the counter-rotating configuration, i.e., this type of movement tends to balance the gyroscopic effect produced by the inner and outer shafts, cancelling one another. Table 4.11 displays the obtained critical speeds and compares them with the ones acquired by Ferraris.

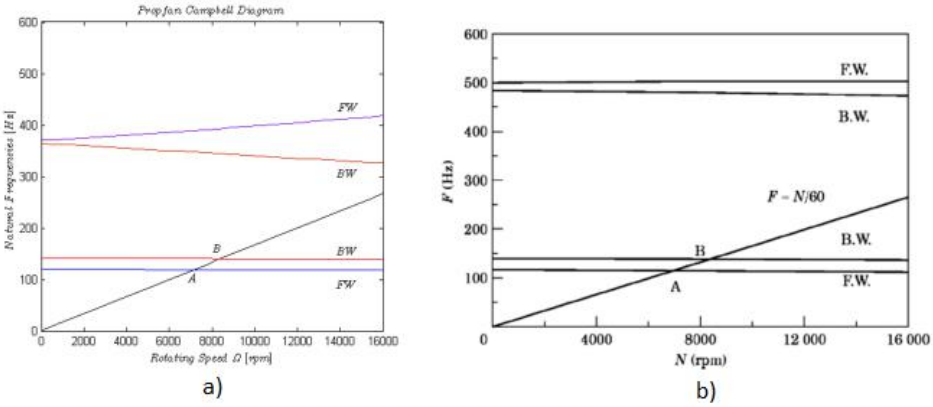

Figure 4.19: Propfan Campbell diagram: a) Used model b) Lalanne and Ferraris model (source [42]).

Table 4.11: Propfan's critical speed comparison.

Critical Speeds (rpm)	FW	BW
Used model	7145	8420
Ferraris, et al. [42]	7019	8357
Deviation (%)	1,79	0,76

After completing the modal analysis, a study of the system's response due to a mass unbalanced excitation was performed. In order to do so, punctual masses of $m_u \cdot d_u = 10g \cdot mm$ at 0° are placed on the first disk. From this analysis, the response diagram was plotted and compared it with the one acquired by Ferraris in Figures 4.20 a) and b).

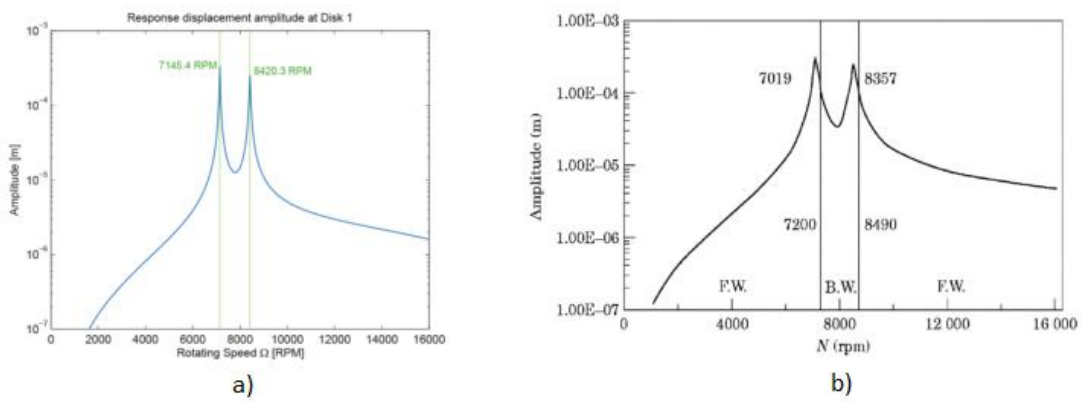

Figure 4.20: Propfan response diagram: a) Used model b) Lalanne and Ferraris model (source [42]).

As expected, the maximum displacements occur at the critical speeds for both models. Since one is dealing with asymmetric bearings, both critical speeds are excited (BW and FW). Examining the critical speed values for both models, one notices a small discrepancy between them (lower than 2%). This difference is related to the fact that the two models weren't computed with the same exact conditions, which suggest a possible reason for the disparity of the higher frequency modes visible in the Campbell Diagram (Figure 4.19 b)). The response of the second disk is similar, as such it was not presented.

Regardless, considering the data limitations and simplifications of the designed model, the results are satisfying. Therefore, the main objective established for this section was accomplished.

Chapter 5

Conclusion

Encouraged by the need for more convenient and efficient means to analyse the dynamic behaviour of rotation machinery, this thesis main objective has been to validate a numerical method (FEM) to study the response of a rotor system. To achieve this, one compared the natural frequencies and critical velocities obtained by the MFS equipment, available at Mechanics Vibration Laboratory at IST, with the results from the numerical models, thus validating the numerical methodology used in this work.

5.1 Rotordynamics Analysis

In section 4.1.1, a convergence study was performed in order to validate the finite element model created in $Matlab$. The study consisted in a comparison against the model conceived in $ANSYS$, which demonstrated a good coherence between both models as shown in Figure 4.2.

To support the convergence study, a comparison between the finite element model and the Rayleigh-Ritz method was carried out for both symmetric and asymmetric system. The natural frequencies and critical speeds were displayed in Tables 4.3 and 4.4. The results obtained with the FEM, for a disk located in the middle of the shaft, revealed an excellent agreement with the values presented by the Rayleigh-Ritz method; although if the disk is moved away from the middle of the shaft the FEM diverged considerably from the values found in literature. This divergence reinforces the fact that even if the shape function respects the system's boundary conditions, it may not correctly describe the behaviour of the rotation machinery, especially for cases where the concentrated mass (disk) is dislocated from the shaft center. Additionally, the system's response to a mass unbalanced excitation was presented for both symmetric and asymmetric rotor. The amplitude diagram for the symmetric rotor, clearly shows a single peak despite the fact that the excitation frequency line intercepts the Campbell diagram in two different speeds, confirming that symmetric rotors submitted to synchronous excitations only excite the FW modes. As for the asymmetric rotor, the amplitude diagram presents two distinct peaks, proving that asymmetric rotors subjected to synchronous excitations excite both FW and BW modes.

Section 4.3 presented the comparison between the numerical and the experimental results of the steel beam and the mono rotor, providing the dynamic response of both structures. Satisfying results

were easily obtained for the steel beam analysis, since the first three frequency differences between the numerical and experimental models were very narrow as shown in Table 4.5, approving the well functioning of the lab equipment and providing valuable experience in modal testing. The FRFs obtained for the MFS (first stage) revealed distinctive peaks at approximately 47,8 and 57,19 Hz, which correspond to the rotor's first and second natural frequency respectively. These values proved to be quite similar with the data acquired from both numerical models as shown in Table 4.7. As for the second stage, one also found a coherence between the critical speeds obtained with the numerical model and the values observed in the autospectrum curves (Figure 4.15). Despite the fact that for high shaft spin speeds the dampening effect becomes too high to observe the intended results, for lower rotating speeds the critical speed values are visible and similar with the ones acquired using the FEM (Table 4.9).

It is important to mention that one can only by analysing the different tests performed during this thesis simultaneously, one can achieve the completion of this thesis objective, the validation of the numerical methodology (FEM) applied to rotor systems.

5.2 The Propfan Case Study

In the case study presented in section 4.4, the proposed numerical method is applied to a Propfan counter rotating bi-rotor engine. A coherence was achieved between the results obtained with the model and the example found in literature for the first two natural frequencies, mode shapes and critical speeds.

On the other hand, the limitations of the finite element model are very clear. The last two modes show noticeable differences on the natural frequencies and their development, since the frequencies acquired with the developed model have lower values and are highly affected by the gyroscopic effects. Considering that the two model are not identical, these dissimilarities are expectable. Regardless, an agreement between the critical speeds was obtained.

5.3 Further Developments

As for future projects development, one may suggest the expansion of the numerical model (in a finite element program) to include the remaining components of the MFS, e.g. the support plate. This new model would be even more accurate in the dynamic analysis of the rotor system in view of the changes introduced to the structure.

It is also important to mention that the rotordynamic model presented didn't contain non-linearities such as internal damping and non linear damping. Thus, one may also suggest the adjustment of the new numerical model with the experimental model resorting to techniques such as model updating.

Regarding the experiment itself, this work didn't include experimental analysis of the rotor orbits, since one didn't have access to the required lab equipment. The inclusion of this test would be a great addition to the validation of the numerical methodology, considering that one would be able to not only determine the natural frequencies and critical speeds of the rotor, but also the maximum displacements, orbit path and phase changes under different spin speeds.

References

[1] G. Genta. *Dynamics of Rotating Systems*. New York : Springer, 1998.

[2] J. Vance, F. Zeidan, and B. Murphy. *Machinery Vibrations and Rotordynamics*. John Wiley and Sons, Inc., Hoboken, New Jersey, 2010.

[3] M. Lalanne and G. Ferraris. *Rotordynamics Prediction in Engineering*. Chhichest: Wiley and Sons, 2nd edition, 1998.

[4] R. Carvalho. A frequency-domain methodology for rotordynamics: Analysis and force identification. Master's thesis, Instituto Superior Técnico, Lisboa, Portugal, 2012.

[5] M. Matos. Balancing and force identification in rotordynamics. Master's thesis, Instituto Superior Técnico, Lisboa, Portugal, 2013.

[6] F. C. Nelson. Rotor dynamics without equations. *International Journal of COMADEM*, vol. 10(3): pp. 2–10, 2007.

[7] H. H. Jeffcott. The lateral vibration of loaded shafts in the neighbourhood of a whirling speed - the effect of want of balance. *Philos. Mag*, 1919.

[8] W. Campbell. *Protection of steam turbine disk wheels from axial vibration*. Schenectady, N.Y: General electric company, 1924.

[9] R. Ruhl and J. Booker. A finite element model for distributed parameter turborotor systems. *Journal of Engineering for Industry*, 1972.

[10] H. Nelson and J. McVaugh. The dynamics of rotor-bearing systems using finite elements. *Journal of Engineering for Industry*, 1976.

[11] H. Nelson. A finite rotating shaft element using timoshenko beam theory. *Journal of Mechanical Design*, 1980.

[12] G. Genta. Consistent matrices in rotor dynamics. *Meccanica*, 1985.

[13] J. Rao. *History of Rotating Machinery Dynamics*. Springer Netherlands, 2011.

[14] C. W. de Silva. *Vibration and Shock Handbook (Mechanical Engineering)*. CRC Press, 2005.

[15] Maia, Silva, He, Lieven, Lin, Skingle, To, and Urgueira. *Theoretical and experimental modal analysis*. Research Studies Press, 1998.

[16] B. Schwarz and M. Richardson. Experimental modal analysis. *Vibrant Technology, Inc.*, 1999.

[17] M. Skeen and G. Lucas. *Bruel & Kjaer Labshop Primer*. University of New South Wales, Schoold of Mechanical and Manufacturing Engineering, 2009.

[18] S. Timoshenko and J. Goodier. *Theory of elasticity*. McGraw-Hill, 1951.

[19] Y. C. Fung. *A First Course in Continuum Mechanics*. Prentice Hall, 3rd ed edition, 1994.

[20] H. Policarpo. Analytical, numerical and experimental study of the dynamical response of helicoidal springs and periodic bars. Master's thesis, Instituto Superior Técnico, Lisboa, Portugal, 2008.

[21] J. Reddy. *An Introduction to The Finite Element Method*. McGraw-Hill, 3rd ed edition, 2005.

[22] S. Rao. *The Finite Element Method in Engineering*. Elsevier/Butterworth Heinemann, 5th ed edition, 2011.

[23] R. D. Cook. *Concepts and Applications of Finite Element Analysis*. Wiley, 4th ed edition, 2001.

[24] N. Maia. *Introdução à dinâmica analítica*. IST Press, 2000.

[25] C. Birdsong. Basics of structural vibration, testing and analysis. *Sound and Vibration*, 2003.

[26] A. technologies. The fundamentals of modal testing: Application notes. 2000.

[27] E. Swanson, C. Powell, and S. Weissman. A practical review of rotating machinery critical speeds and modes. *Sound and Vibration*, 2005.

[28] ANSYS. Element reference manual v14.5, sas ip, 2013.

[29] MathWorks. Matlab documentation, 2013. URL `http://www.mathworks.com/help/matlab/index.html`.

[30] M. N. S. Ganeriwala. *Critical Speeds in Rotating Machinery*. PhD thesis, 2008.

[31] P. Lagos. Caracterização da resposta de vibração de um exaustor. Master's thesis, Instituto Superior Técnico, Lisboa, Portugal, 2016.

[32] P. Avitabile. Experimental modal analysis. *Sound and Vibration*, 2001.

[33] S. Saeed and A. Farhad. Effects of accelerometers mounting methods on quality of measured frf's. *Sound and Vibration*, 2014.

[34] O. Dossing. *Structural testing Part1 - Mechanical Mobility Measurments*. Denmark, 1988.

[35] H. Al-Khazali and M. Askari. Modal analysis design to exposure gyroscopic effect in rotating machinery using experimental and analytical/computational techniques. *International Journal of Engineering Science and Technology*, 2011.

[36] Product data impact hammer — type 8202; http://docslide.us/documents/hammerbk8202pdf.html.

[37] Product data force transducer — pcb 280c01; http://www.pcb.com/products/model/208c01.

[38] Accelerometer types 4507 and 4508; https://www.bksv.com/media/doc/bp1841.pdf.

[39] System data, types 3560-b and 3560-d; https://www.bksv.com/media/doc/bu0228.pdf.

[40] S. Gade and J. Michaelsen. News form the factory (technical review no.4). Technical report, Brüel & Kjaer, 1982.

[41] Machinery fault simulator; http://spectraquest.com/machinery-fault-simulator/details/mfs/.

[42] G. Ferraris, V. Maisonneuve, and M. Lalanne. Prediction of the dynamic behavior of non-symmetric coaxial co- or counter-rotating rotors. *Sound and Vibration*, 1996.

[43] J. Silva. Frequency domain force identification problem and the relation between force and displacement multi-degrees-of-freedom transmissibility. Master's thesis, Instituto Superior Técnico, Lisboa, Portugal, 2017.

[44] E. Hirschel, H. Prem, and G. Madelung. *Aeronautical Research in Germany: From Lilienthal until Today*. Springer-Verlag Berlin Heidelberg, 1 edition, 2004.

[45] P. Paulo. A time-domain methodology for rotor dynamics: Analysis and force identification. Master's thesis, Instituto Superior Técnico, Lisboa, Portugal, 2011.

Appendix A

Shaft Finite Element Matrices

Applying the Lagrange equation 2.49 in the shaft's kinetic 2.60 and strain 2.61 energy equation, results in:

$$\frac{d}{dt}\left(\frac{\partial T_S}{\partial \dot{\delta}}\right) - \frac{\partial T_S}{\partial \delta} = (M + M_S)\ddot{\delta} + C\dot{\delta} + (K_C + K_F)\delta \tag{A.1}$$

where M and M_S represent the mass matrices, K_C and K_F are the stiffness matrices, C stands for the damping matrix and δ is the nodal displacement vector for the shaft finite element. These matrices apply the Euler-Bernoulli beam theory with shear correction, and were used in the Matlab code.

A.1 Mass Matrices

$$M = \frac{\rho S L}{420}\begin{bmatrix} 156 & 0 & 0 & -22L & 54 & 0 & 0 & 13L \\ 0 & 156 & 22L & 0 & 0 & 54 & -13L & 0 \\ 0 & 22L & 4L^2 & 0 & 0 & 13L & -3L^2 & 0 \\ -22L & 0 & 0 & 4L^2 & -13L & 0 & 0 & -3L^2 \\ 54 & 0 & 0 & -13L & 156 & 0 & 0 & 22L \\ 0 & 54 & 13L & 0 & 0 & 156 & -22L & 0 \\ 0 & -13L & -3L^2 & 0 & 0 & -22L & 4L^2 & 0 \\ 13L & 0 & 0 & -3L^2 & 22L & 0 & 0 & 4L^2 \end{bmatrix} \tag{A.2}$$

$$M_S = \frac{\rho I}{30L}\begin{bmatrix} 36 & 0 & 0 & -3L & -36 & 0 & 0 & -3L \\ 0 & 36 & 3L & 0 & 0 & -36 & 3L & 0 \\ 0 & 3L & 4L^2 & 0 & 0 & -3L & -L^2 & 0 \\ -3L & 0 & 0 & 4L^2 & 3L & 0 & 0 & -L^2 \\ -36 & 0 & 0 & 3L & 36 & 0 & 0 & 3L \\ 0 & -36 & -3L & 0 & 0 & 36 & -3L & 0 \\ 0 & 3L & -L^2 & 0 & 0 & -3L & 4L^2 & 0 \\ -3L & 0 & 0 & -L^2 & 3L & 0 & 0 & 4L^2 \end{bmatrix} \tag{A.3}$$

A.2 Damping Matrices

$$C = \frac{\rho I \Omega}{15L}\begin{bmatrix} 0 & -36 & -3L & 0 & 0 & -36 & -3L & 0 \\ 36 & 0 & 0 & -3L & -36 & 0 & 0 & -3L \\ 3L & 0 & 0 & -4L^2 & -3L & 0 & 0 & L^2 \\ 0 & 3L & 4L^2 & 0 & 0 & -3L & -L^2 & 0 \\ 0 & 36 & 3L & 0 & 0 & -36 & 3L & 0 \\ -36 & 0 & 0 & 3L & 36 & 0 & 0 & 3L \\ 3L & 0 & 0 & L^2 & -3L & 0 & 0 & -4L^2 \\ 0 & 3L & -L^2 & 0 & 0 & -3L & 4L^2 & 0 \end{bmatrix} \tag{A.4}$$

A.3 Stiffness Matrices

$$K_C = \frac{EI}{(1+a)L^3}\begin{bmatrix} 12 & 0 & 0 & -6L & -12 & 0 & 0 & -6L \\ 0 & 12 & 6L & 0 & 0 & -12 & 6L & 0 \\ 0 & 6L & (4+a)L^2 & 0 & 0 & 6L & (2-a)L^2 & 0 \\ -6L & 0 & 0 & (4+a)L^2 & 6L & 0 & 0 & (2-a)L^2 \\ -12 & 0 & 0 & 6L & 12 & 0 & 0 & 6L \\ 0 & -12 & -6L & 0 & 0 & 12 & -6L & 0 \\ 0 & 6L & (2-a)L^2 & 0 & 0 & -6L & (4+a)L^2 & 0 \\ -6L & 0 & 0 & (2-a)L^2 & 6L & 0 & 0 & (4+a)L^2 \end{bmatrix} \tag{A.5}$$

$$K_F = \frac{F}{30L}\begin{bmatrix} 36 & 0 & 0 & -3L & -36 & 0 & 0 & -3L \\ 0 & 36 & 3L & 0 & 0 & -36 & 3L & 0 \\ 0 & 3L & 4L^2 & 0 & 0 & -3L & -L^2 & 0 \\ -3L & 0 & 0 & 4L^2 & 3L & 0 & 0 & -L^2 \\ -36 & 0 & 0 & 3L & 36 & 0 & 0 & 3L \\ 0 & -36 & -3L & 0 & 0 & 36 & -3L & 0 \\ 0 & 3L & -L^2 & 0 & 0 & -3L & 4L^2 & 0 \\ -3L & 0 & 0 & -L^2 & 3L & 0 & 0 & 4L^2 \end{bmatrix} \tag{A.6}$$

where a represents the shear effect influence, given by:

$$a = \frac{12EI}{GS_rL^2} \tag{A.7}$$

with the shear modulus of an isotropic material:

$$G = \frac{E}{2(1+\nu)} \tag{A.8}$$

where ν is the Poisson's ratio, E is the Young's modulus and S_r is shaft cross-section area.

Appendix B

ANSYS Campbell Diagrams

In this section, one shows the Campbell diagrams obtained for $ANSYS$ finite element model. The first two diagrams are related to the symmetric rotor (section 4.2.1) for two disk positions, as illustrated in Figure B.1 a) and b).

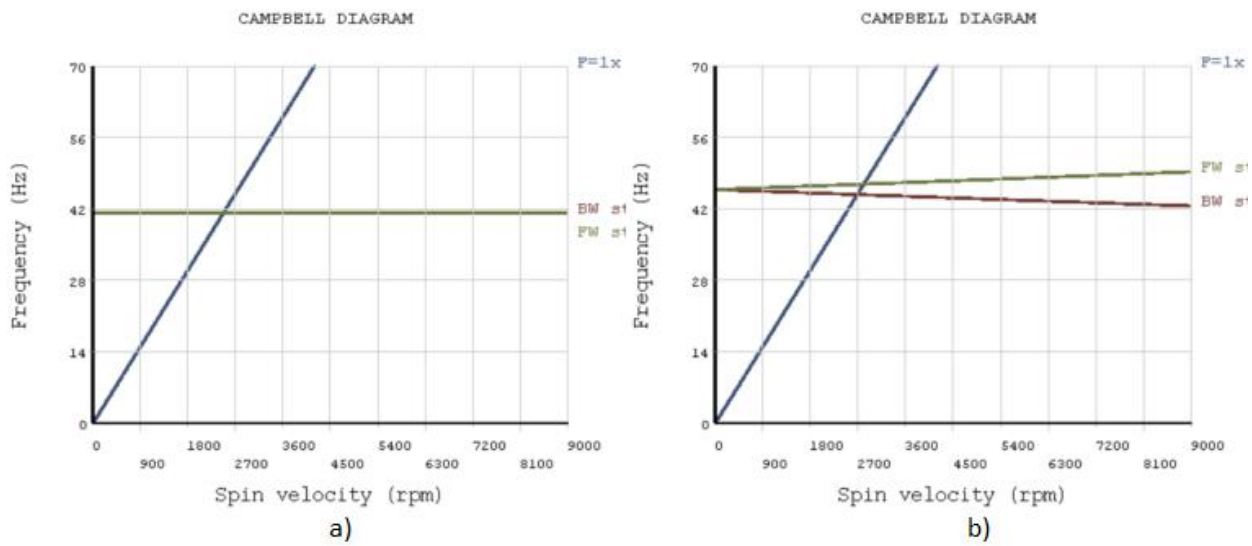

Figure B.1: Campbell diagram symmetric rotor: a) Disk location $l_1 = L/2$; b) Disk location $l_1 = L/3$.

From the $ANSYS$ solution and Figure B.1, one may extract the first natural frequency at rest as well as the critical speeds for a disk located at $l_1 = L/2$ and $l_1 = L/3$, as shown in Table B.1.

Table B.1: Symmetric rotor first natural frequency at rest and critical speeds for both disk positions - $ANSYS$.

Mode	**Frequency at Rest (Hz)**		**Critical Speeds (rpm)**	
	$l_1 = L/2$	$l_1 = l/3$	$l_1 = L/2$	$l_1 = L/3$
1 (BW)	41,39	45,71	2482	2679
2 (FW)	41,39	45,71	2482	2801

The mode shapes corresponding to the first natural frequency for both disk positions are displayed in Figure B.2 a) and b).

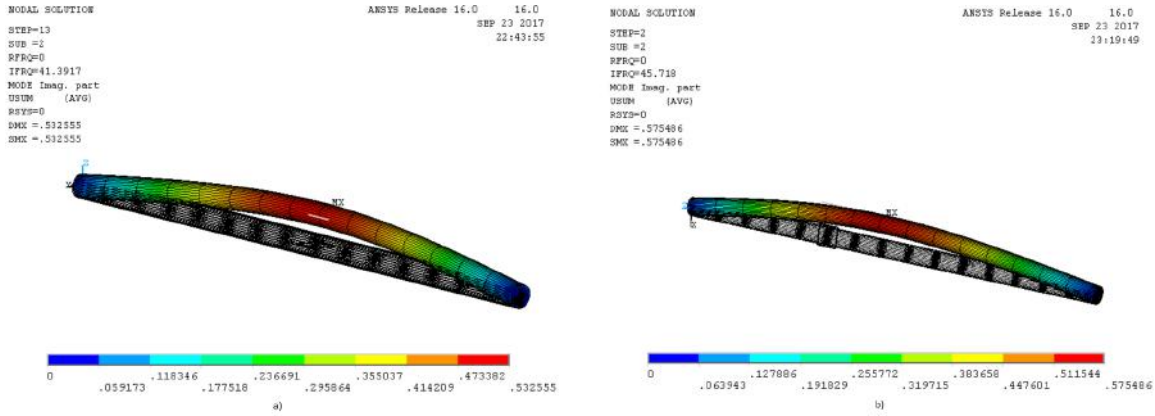

Figure B.2: Mode shapes corresponding to the first natural frequency: a) Disk location $l_1 = L/2$; b) Disk location $l_1 = L/3$.

The following Campbell diagrams are related to the asymmetric rotor (section 4.2.2) for two disk positions, as shown in Figure B a) and b).

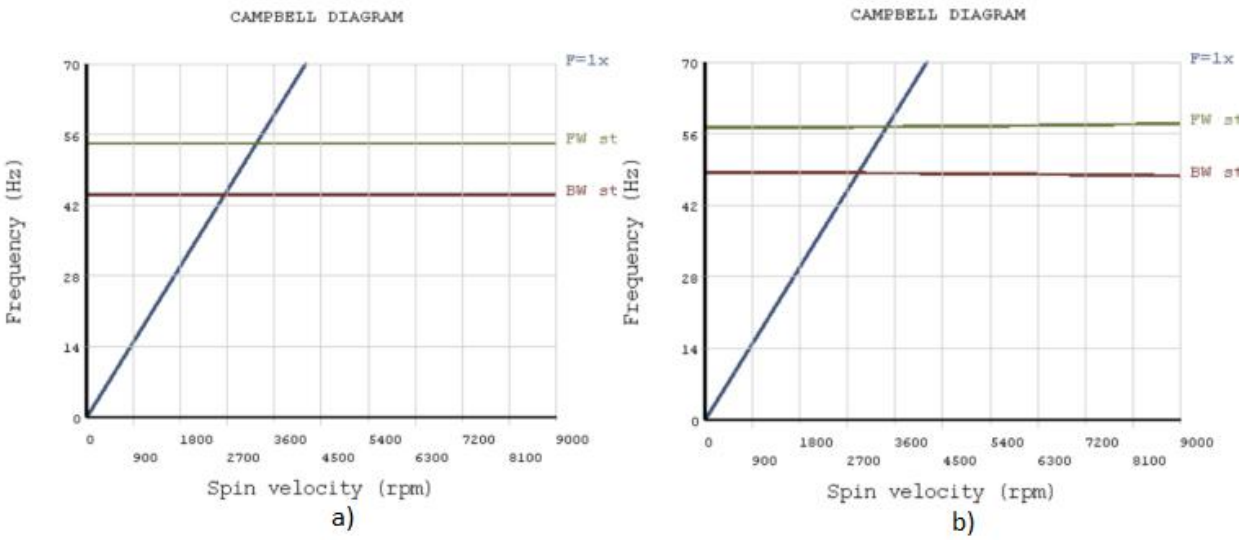

Figure B.3: Campbell diagram asymmetric rotor: a) Disk location $l_1 = L/2$; b) Disk location $l_1 = L/3$.

Just as the symmetric rotor, from Figure B.3 one may extract the first two natural frequencies at rest as well as the critical speeds for $l_1 = L/2$ and $l_1 = L/3$, as shown in Table B.2.

Table B.2: Asymmetric rotor first two natural frequency at rest and critical speeds for both disk positions - $ANSYS$.

Mode	**Frequency at Rest (Hz)**		**Critical Speeds (rpm)**	
	$l_1 = L/2$	$l_1 = l/3$	$l_1 = L/2$	$l_1 = L/3$
1 (BW)	44,26	48,32	2655	2890
2 (FW)	54,92	57,17	3294	3431

The mode shapes corresponding to the first two natural frequencies for both disk positions are displayed in Figure B.4 and B.5.

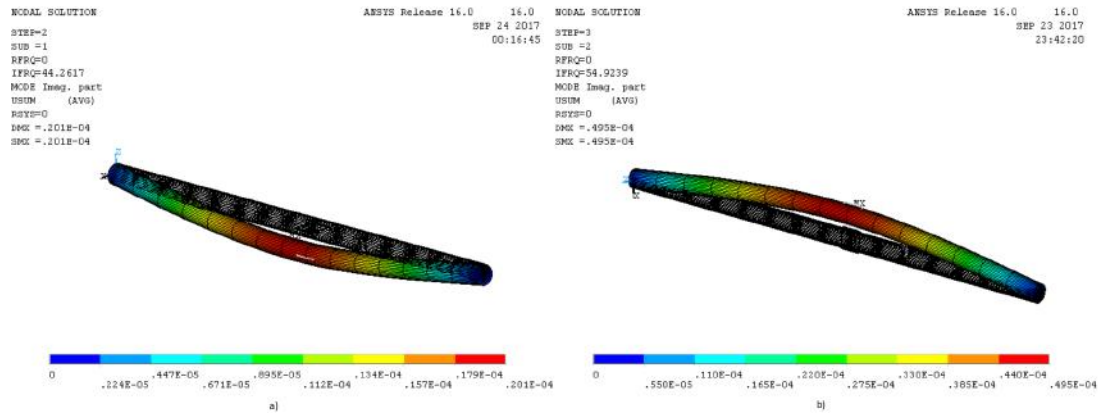

Figure B.4: Mode shapes corresponding to the first and second natural frequencies for $l_1 = L/2$: a) First natural frequency; b) Second natural frequency.

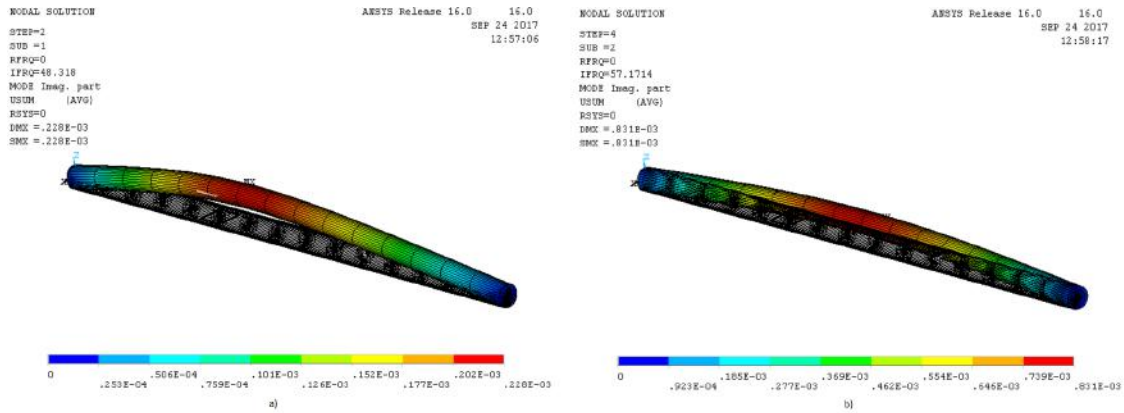

Figure B.5: Mode shapes corresponding to the first and second natural frequencies for $l_1 = L/3$: a) First natural frequency; b) Second natural frequency.

Appendix C

Frequency Response Functions of the Rotor at Rest

This section contains a separate display of the rotor's frequency response (in terms of mechanical receptance) for the six pre-established accelerometer measurement positions (D_X, D_Z, S_X, S_Z, B_X and B_Z), presented in section 4.3.2. In this case, one may observe the first and second natural frequency highlighted in each curve.

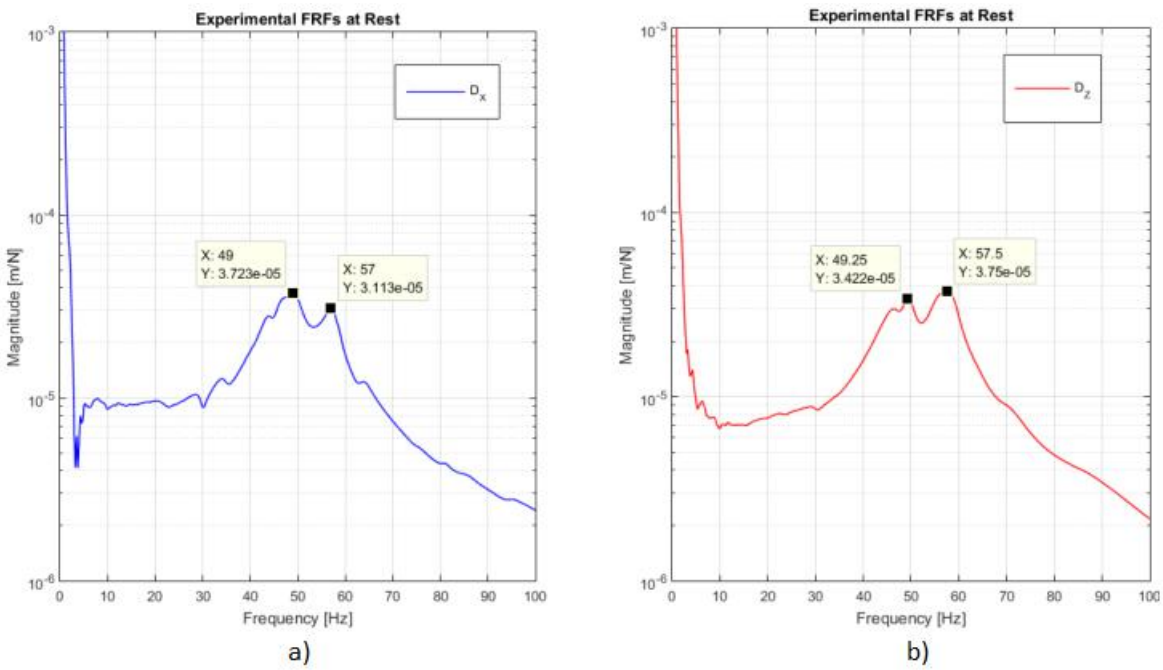

Figure C.1: FRF of the disk: a) Horizontal; b) Vertical.

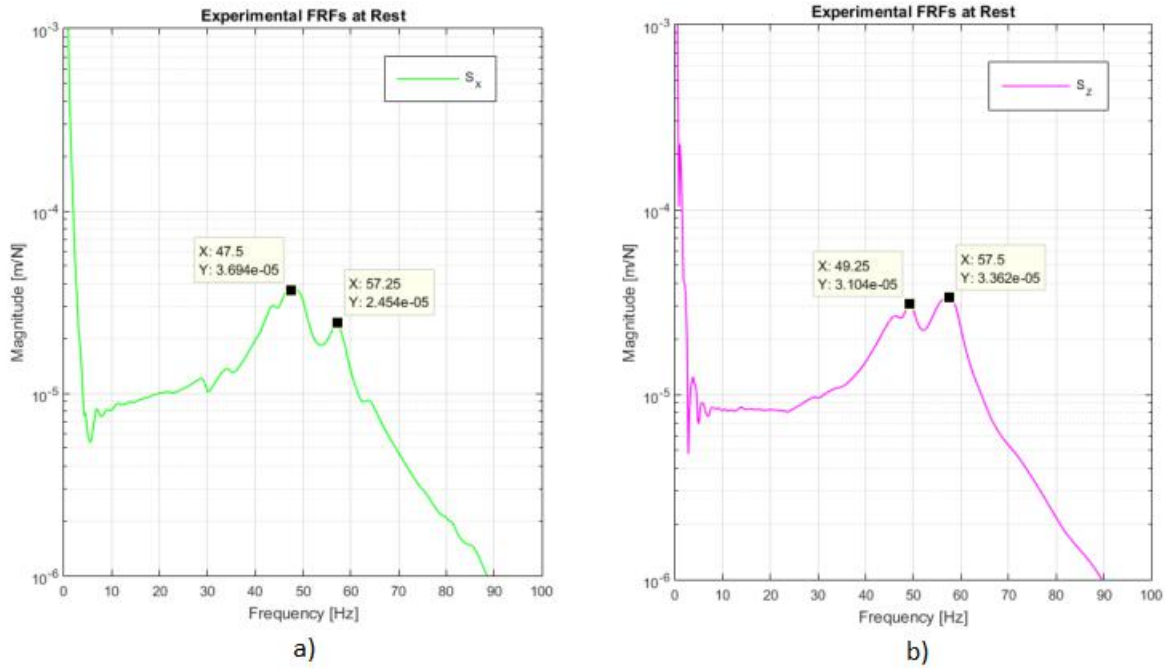

Figure C.2: FRF of the shaft: a) Horizontal; b) Vertical.

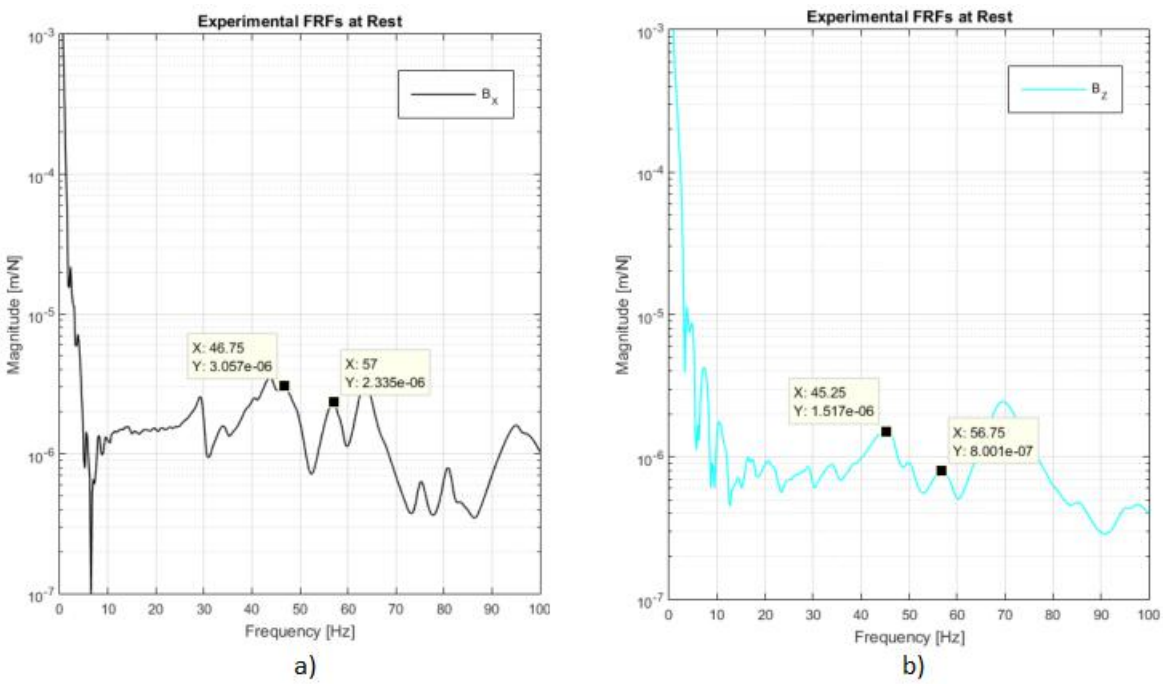

Figure C.3: FRF of the bearing: a) Horizontal; b) Vertical.

Appendix D

Experimental Autospectrum Functions

This section contains a separate display of the Autospectrum functions (in terms of mechanical receptance) for the four shaft spin speeds (5 Hz (300 RPM), 10 Hz (600 RPM), 20 Hz (1200 RPM) and 30 Hz (1800 RPM)), presented in section 4.3.2. In this case, one may have a closer look on the first and second critical speed (in Hz) highlighted in each curve.

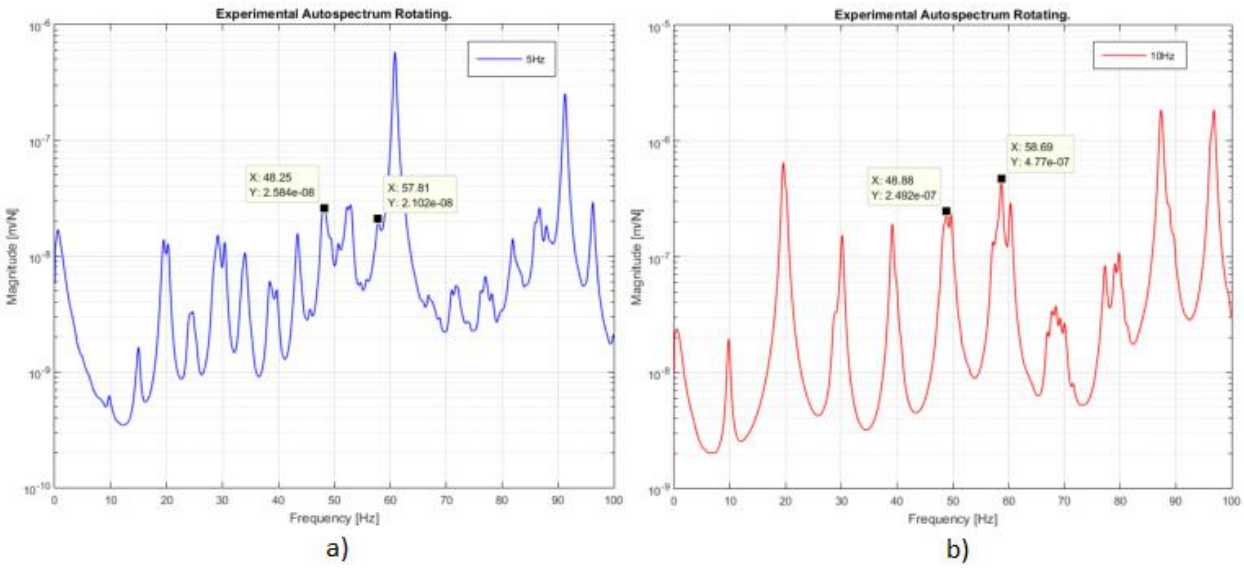

Figure D.1: Experimental Autospectrum for a rotation speed of: a) 5 Hz (300 RPM); b) 10 Hz (600 RPM).

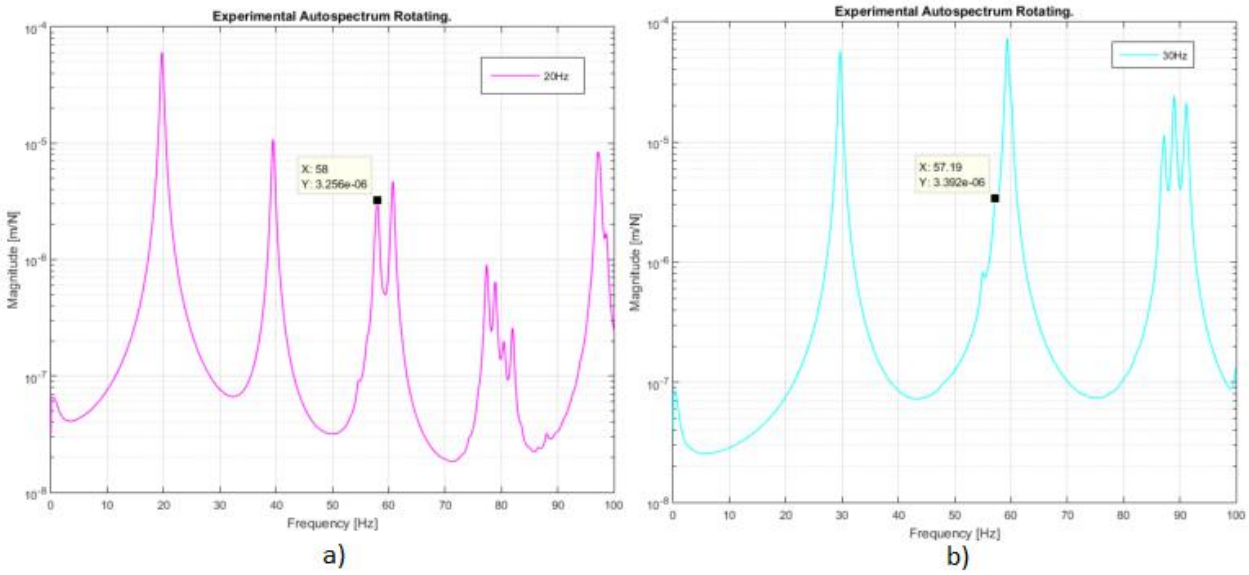

Figure D.2: Experimental Autospectrum for a rotation speed of: a) 20 Hz (1200 RPM); b) 30 Hz (1800 RPM).